

# **Evolution and Flare Activity of $\delta$ -spots in Cycle 23**

Thesis submitted in accordance with the requirements of  
the Kyoto University for the degree of Doctor in Philosophy

by

**Kan Takizawa**

June 2015



# Preface

It is known that  $\delta$ -spot group is the most flare-active one among all the sunspot types. However, it is still not clear what causes the strong flare activity. In this thesis, the author observationally studied the  $\delta$ -sunspots to find their flare productive conditions. To know the occurrence conditions of solar flare is not only beneficial for the advance of solar physics, but also for the human activity itself, because the major flare activity may damage the telecommunication network and the electricity supply network as the basis of our modern life. If we succeed to predict the occurrences of the major flare, possible social disasters will be avoided. After the launch of SOHO satellite in 1995, solar observation entered into a regular observation era from space. The SOHO mission succeeded to observe the solar surface through one solar cycle (Cycle 23) from space for the first time. The abundant and homogeneous data must contribute to increase the reliability of the statistical study. We mainly relied on the SOHO/MDI data, namely the magnetograms and the intensitygrams, in this study.

There are several challenges when considering the generation and development of  $\delta$ -spots. Among them, the author tried to clear the following questions in this study.

- i) How are  $\delta$ -spots born and how do they develop? (Formation of  $\delta$ -configuration)
- ii) What conditions make flare occurrence at  $\delta$ -spots? (Flare occurrence conditions)
- iii) How do  $\delta$ -spots keep themselves for a long time? (Long life of  $\delta$ -spots)
- iv) How do  $\delta$ -spots decay at last? (Decay of  $\delta$ -spots)

The thesis is organized as follows:

Chapter 1 is the general introduction to sunspots and the relationship between  $\delta$ -spots and solar flare activity.

In Chapter 2, we report the general properties for the  $\delta$ -spots appeared in Cycle 23 as the background of the detailed study.

In Chapter 3, we will focus on 31  $\delta$ -spots which can be studied from their birth phase. The results can be summarized as follows:

- i) Emerging  $\delta$  active regions (ARs) can be classified into three topological types as “quasi- $\beta$ ”, “writhed” and “top-to-top”. ii) Among them, “writhed” and “top-to-top” types tend to show high flare activity. iii) As the handedness of twist and writhe agree

---

with each other in most cases of “writhed” types (12 cases out of 13), we propose a magnetic model that multiple emerging flux regions in an  $\delta$  AR are not separated but united as a single structure below the solar surface. iv) Almost all the “writhed” type ARs have downward knotted structures in the mid portion of the magnetic flux tube, which are the essential elements of  $\delta$  ARs. v) The flare activity of  $\delta$  ARs highly correlate not only with the sunspot areas but also with the magnetic complexity, in a statistical sense. vi) We suggest that there is a possible scaling-law between Flare Index (FI) and the maximum umbral area.

In Chapter 4, we report on remarkable photospheric down flows near the neutral line in  $\delta$  active region NOAA 9957 as a case study of the  $\delta$ -spots decay. We interpreted this phenomenon as a magnetic flux submergence.

Chapter 5 gives our summary, and concluding discussions.

# Abstract

Emergence and magnetic evolution of solar active regions (ARs) of  $\beta\gamma\delta$ -type, which are known to be highly flare-active, were studied with the SOHO/MDI data in Cycle 23. The author and co-researcher selected 31 ARs, which can be observed from their birth phase, as unbiased samples of our study. From the analysis of magnetic topology (twist and writhe), we obtained the following results.

- i) From the point of view of topology, emerging  $\beta\gamma\delta$  ARs can be classified broadly into three categories: “quasi- $\beta$ ”, “writhed”, and “top-to-top”. The “top-to-top” type has the most complex topology and the “quasi- $\beta$ ” is the simplest type. The “writhed” group has medium complexity among the three types.
- ii) The ARs of more complex topology tend to exhibit higher flare activity.
- iii) The “writhed” types tend to have the same handedness of the twist and writhe.
- iv) We infer that downward-knotted structure in the mid portion of the flux tube are the essential elements of the active  $\beta\gamma\delta$  ARs.
- v) The flare activities of  $\beta\gamma\delta$  ARs highly correlate not only with the sunspot areas but also with the magnetic complexity.
- vi) We suggest the existence of a possible scaling-law between the flare index (FI) and the maximum umbral area ( $S_{Umax}$ ).

Furthermore, the author and co-researchers studied an inactive  $\beta\gamma\delta$  AR in its decaying phase as a representative example. In an inactive  $\beta\gamma\delta$  sunspot group NOAA 9957, we detected continuous prominent downflow motions of  $1500\text{-}1700\text{ m s}^{-1}$  for several hours on the magnetic neutral line (NL). In the downflow region, penumbral structures were observed to shrink and decay. We interpreted the phenomenon as one case of submergence of the magnetic flux and summarized as follows.

- i) In a rapidly decaying  $\beta\gamma\delta$ -type AR NOAA 9957, we have detected continuous and prominent downflows on magnetic neutral line.
- ii) The downflow motions occurred intermittently with an average lifetime of 12 hrs.
- iii) Near the downflow area, converging horizontal flow to the NL from both sides was found to continue almost 5 hrs. We suppose that the moat flow motions from two large

---

positive polarities promote or drive the phenomenon.

iv) Several submergences occurred along the NL which were accompanied by the flux cancellations and low flare activities.

# Contents

<b>Preface</b>	<b>i</b>
<b>Abstract</b>	<b>iii</b>
<b>Contents</b>	<b>vi</b>
<b>List of Figures</b>	<b>viii</b>
<b>List of Tables</b>	<b>ix</b>
<b>Acknowledgement</b>	<b>xi</b>
<b>1 Introduction</b>	<b>1</b>
1.1 Overview of Sunspots . . . . .	1
1.1.1 History of Sunspots Observation . . . . .	1
1.1.2 Sunspots . . . . .	2
1.1.3 Solar Cycle . . . . .	4
1.1.4 Magnetic Field . . . . .	5
1.1.5 General Morphological Models for EFRs . . . . .	8
1.2 $\delta$ -Spots . . . . .	9
1.2.1 Formation Paths of $\delta$ -Spots . . . . .	10
1.2.2 Flare Activity . . . . .	10
1.2.3 Observational Model of $\delta$ -Spot . . . . .	11
1.2.4 Magnetic Helicity . . . . .	12
<b>2 Preliminary Statistical Study of Sunspots in Cycle 23</b>	<b>15</b>
2.1 Data Set . . . . .	15
2.2 Overview of Flare Activity in Cycle 23 . . . . .	17
2.2.1 Relation between Maximum Area and Flare Index . . . . .	17
2.2.2 Relation between Lifetime and FI . . . . .	18
2.2.3 Histograms of Maximum Area, FI, and Lifetime . . . . .	18
2.2.4 Position of $\beta\gamma\delta$ -Spots among All Flaring ARs . . . . .	22
2.2.5 Relation between $\delta$ -Days and FI . . . . .	22

---

2.3	Purposes of This Thesis . . . . .	23
<b>3</b>	<b>Evolution and Flare activity of <math>\delta</math>-Sunspots in Cycle 23</b>	<b>25</b>
3.1	Introduction . . . . .	25
3.2	Data and Analysis . . . . .	26
3.2.1	Region Selection . . . . .	26
3.2.2	Imaging Data . . . . .	27
3.2.3	Image Analysis . . . . .	27
3.3	Results . . . . .	30
3.3.1	Case Studies . . . . .	31
3.3.2	Statistical Study . . . . .	44
3.4	Discussion . . . . .	52
3.5	Conclusions . . . . .	54
<b>4</b>	<b>Prominent Photospheric Downflows on Magnetic Neutral Line in a <math>\delta</math>-spot</b>	<b>57</b>
4.1	Introduction . . . . .	57
4.2	Data & Analysis . . . . .	59
4.3	Results . . . . .	62
4.3.1	Case Study of Most Prominent Redshift Patch . . . . .	62
4.3.2	Statistical Study of Redshift Patches . . . . .	64
4.4	Discussion and Conclusions . . . . .	66
<b>5</b>	<b>Conclusions and Discussion</b>	<b>71</b>
5.1	Conclusions . . . . .	71
5.2	Discussion . . . . .	72
5.2.1	Formation of $\delta$ -Configuration . . . . .	72
5.2.2	Flare Occurrence Conditions in $\delta$ -State . . . . .	72
5.2.3	Cause of Long Life for $\delta$ -Spots . . . . .	72
5.2.4	Decay of $\delta$ -Spots . . . . .	73
	<b>Bibliography</b>	<b>75</b>



# List of Figures

1.1	Sunspots sketch of Scheiner . . . . .	3
1.2	A Sample of Magnetogram . . . . .	5
1.3	Cartoon of Hale-Nicholson polarity law . . . . .	6
1.4	Mount Wilson magnetic classification . . . . .	8
1.5	Zwaan's $\Omega$ -loop model . . . . .	9
1.6	Schematic drawing of an emerging twisted flux rope . . . . .	12
1.7	Sample images of coronal sigmoid . . . . .	13
1.8	Magnetic Tongue patterns . . . . .	13
2.1	Relations between Maximum Area and Peak X-ray flux in Cycle 22 . . . .	16
2.2	Peak intensity of flares for different magnetic classes in Cycle 22 . . . .	16
2.3	Relations between Maximum Area and FI of three magnetic types . . . .	19
2.4	Relations between Maximum Area and Lifetime of three magnetic types . .	20
2.5	Histograms of Maximum Area, FI, and Lifetime in Cycle23 . . . . .	21
2.6	Venn diagram for flaring ARs in Cycle23 . . . . .	22
2.7	Relation between $\beta\gamma\delta$ -state days and FI of $\beta\gamma\delta$ -type ARs . . . . .	23
3.1	Co-aligned image between the magnetogram and the intensitygram . . . .	28
3.2	Sample of erosion operation to the vorticity field . . . . .	29
3.3	Illustrations of the emergence of tubes with left-handed writhe . . . . .	29
3.4	Sample images of magnetic tongues . . . . .	31
3.5	SOHO/MDI magnetograms and white-light images of NOAA 10720 . . . .	33
3.6	White light images, magnetograms, and vorticity fields of EFR2 . . . . .	34
3.7	Time variations of circulation and magnetic flux in sunspots p2 and n2 . .	35
3.8	Time evolution of sunspot areas in NOAA 10720 . . . . .	36
3.9	Coronal structure images of NOAA 10720 . . . . .	36
3.10	SOHO/MDI magnetograms and white-light images of NOAA 10826 . . . .	38
3.11	Time variations of circulation and magnetic flux in sunspots n1 and p2 . .	39
3.12	Time evolution of sunspot areas in NOAA 10826 . . . . .	40
3.13	A high-pass filtered TRACE 195 Å image of NOAA 10826 . . . . .	40
3.14	SOHO/MDI magnetograms and white-light images of NOAA 10050 . . . .	42

---

3.15	Time variations of circulation and magnetic flux in the main spots . . .	43
3.16	Time evolution of sunspot areas in NOAA 10050 . . . . .	44
3.17	$S_{\max}$ and FI <i>versus</i> the penumbral-umbral radius ratio in the $\delta$ -state . .	47
3.18	Flare index <i>versus</i> maximum umbral area in a logarithmic scale . . . . .	48
3.19	Histograms of $S_{U\max}$ and FI in the $\delta$ -state period . . . . .	49
3.20	Schematic models for $\beta\gamma\delta$ ARs . . . . .	51
3.21	FI and $S_{U\max}$ in the $\delta$ -state as a function of the $\delta$ -duration . . . . .	52
4.1	White light image and magnetogram of AR 9957 . . . . .	58
4.2	Raw and corrected images of MDI Dopplergram . . . . .	58
4.3	Areal evolution of AR9957 . . . . .	59
4.4	Temporal evolution of Doppler velocities in AR 9957 . . . . .	60
4.5	Temporal evolution of the most prominent downflow (RS6) . . . . .	61
4.6	Temporal evolution of horizontal flow . . . . .	62
4.7	Comparison between photospheric down flow and Evershed flow . . . . .	63
4.8	Vector magnetogram data obtained at <i>Huairou Solar Observatory Station</i>	64
4.9	Maximum LOS velocities of redshift patches near the NL in AR 9957 . .	65
4.10	Evolutions of redshift area, magnetic flux, and penumbral area for RS6 .	66
4.11	Schematic image of magnetic flux submergence . . . . .	67

# List of Tables

1.1	Soft X-ray flare classification . . . . .	11
2.1	Flaring Ratio of each magnetic class in Cycle 23 . . . . .	17
2.2	Comparison to lifetimes of flaring and no-flaring ARs . . . . .	18
3.1	Summary of parameters for 31ARs studied . . . . .	46



# Acknowledgement

I express my gratitude and appreciation to Dr. Kitai R., Prof. Ichimoto K., and Prof. Shibata K. for their kind advice and continuous encouragements to my works. Especially, I deeply thank Dr. Kitai for his persistently guidance even after his retirement.

I also appreciate to Prof. Emeritus Kurokawa H., who gave me the initial introduction to solar physics, and Dr. Zhang Y., who was a co-researcher in Kwasan and Hida observatories, for their useful discussion and kindly helps.

I am grateful to all the staffs of Kwasan and Hida observatories of Kyoto University, for their continuous helps. I am also grateful to all staffs and members of Department of Astronomy, Kyoto University, for their helps and useful discussion with them.

I have made extensive use of *SOHO* MDI Data Service, *TRACE* Data Center, and *GOES* Data Service. *SOHO* is a mission of international cooperation between the European Space Agency (ESA) and NASA. *TRACE* is a NASA Small Explorer (SMEX) mission to image the solar corona and transition region at high angular and temporal resolution. The Geostationary Operational Environmental Satellite system (GOES), operated by the United States National Environmental Satellite, Data, and Information Service (NESDIS), carries on weather monitoring researches and also supplies solar soft X-ray data.

I would like to thank my mother, Taeko, and my sister, Junko for their understandings and supports. Finally, I am thankful to my deceased father, Tatsuzo, who made me a first opportunity to study astronomy.

I can keep my studying for this thesis by support of the Grant-in-Aid for the Global COE Program “The Next Generation of Physics, Spun from Universality and Emergence” from the Ministry of Education, Culture, Sports, Science and Technology (MEXT) of Japan. I also received financial support from the Obtaining PhD support project by Foundation of Global Life Learning Center.



# Chapter 1

## Introduction

The descriptions of this chapter are mainly based on following books and papers: Sunspots (Bray and Loughhead, 1979), Astrophysics of the Sun (Zirin, 1988), Discovering the Secrets of the Sun (Kippenhahn, 1994), History of Modern Science and Mathematics volume II, Astronomy and Cosmology, edition 1.4 (Lehoux, 2001), Plasma Astrophysics (Tajima and Shibata, 2002), Sunspots: An overview (Solanki, 2003), The Sun: An introduction, 2nd edition (Stix, 2004), Journey from the center of the Sun (Zirker, 2001), Fundamentals of Solar Astronomy (Bhatnagar and Livingston, 2005), Encyclopedia of the Solar System, 2nd edition, chapter 2 (Aschwanden, 2006), The Physics of Solar Flares (Tandberg-Hanssen and Emslie, 2009), and Physics of the Sun: a first course (Mullan, 2009).

### 1.1 Overview of Sunspots

#### 1.1.1 History of Sunspots Observation

##### 1.1.1.1 Pre-Telescope Observation of Sunspots

In the western world, the earliest reference to naked eye sunspots observation appeared in the fourth century by Theophrastus of Athens (371-287BC), a pupil of Aristotle. Long time later, in 807AD, Einhard, the biographer of Charles the Great, wrote that a spot on the Sun was seen for eight days. At the time it was translated as an appearance of the planet Mercury in front of the Sun.

In the eastern world, the most systematic records of naked-eye observations of sunspots were kept by Chinese, Japanese and Korean astronomers. For example, one of the reports of China in the 354BC referred that a dark object was seen against the disk of the Sun ‘as big as hens egg’.

##### 1.1.1.2 The Dawn of Telescope Observation

The beginning of telescope observation of sunspots was the dawn of modern observational astronomy. There were three pioneers, Fablicius, Scheiner, and Galileo, as

the first observer of sunspots. On 9 March 1611, Johannes Fabricius (1587-1616) and his father, David Fabricius (1564-1617) saw small dark spot on the disk of the Sun through their telescope in East Friesland (in Germany). Johannes Fabricius published the report of the discovery in June 1611.

The day before the discovery of Fabricius, Christoph Scheiner (1575-1650) and his assistant, Johann Baptist Cysat (1588-1657), at Ingolstadt, saw spots on the disk of the Sun. However, Galileo Galilei (1564-1642), the most famous astronomer in Italy, claimed that he had seen spots on the Sun long before, namely in 1610. In any case, sunspots became the subject of research for modern science in the early seventeenth century.

For example, we show one of the remarkable sketches by Scheiner published in 1630 (Figure 1.1). Surprisingly, we can already see several significant features of sunspots in this sketch. We can see how spots move across the disk of the Sun. Their movement suggests that they rotate evenly around a sphere's axis. Most eye-catching feature of the sketch is that a sunspot has a dark central core which is surrounded by an area which is intermediate brightness between the core and the photosphere. Today the central dark part is called "umbra" and the surrounding area is called "penumbra".

## 1.1.2 Sunspots

### 1.1.2.1 Sizes

Sunspots are spanning in all sizes, from tiny "pores" less than 300 km to giants 100000 km in diameter. Pores are the smallest ones which have umbra only. Once a pore grows to a diameter of 10'' or more, penumbra appears, and the feature becomes a mature sunspot. Moderate to large spots usually have an umbra surrounded by a penumbra with many short fine fibrils. In the umbra, the magnetic field lines tend to be nearly vertical, while in the penumbra, they are almost horizontal. The largest spot area which was recorded on 7 April 1947 had an area of  $A \sim 6300$  millionths of the visible solar hemisphere (MSH), i.e., it occupied about 0.6% of the visible surface ( $\text{MSH} \sim 3.32 \text{ Mm}^2$ ). In general, the spots have areas of up to a few hundred MSH: 95% of spots have  $A \leq 500$  MSH (Bray and Loughhead, 1979; Table 6.1).

The diameter ratio of umbra to the total spot including penumbra is around 0.4 on average (Allen, 1973). However the ratio tends to increase according to increased sunspot area (Brandt *et al.*, 1990). We will discuss the variation of the penumbra-umbra radius ratio in more detail in Chapter 3.

### 1.1.2.2 Lifetimes

Individual sunspots last from a few hours to (in the case of the largest spots) several months. Typically, the lifetime is roughly proportional to the maximum area of the



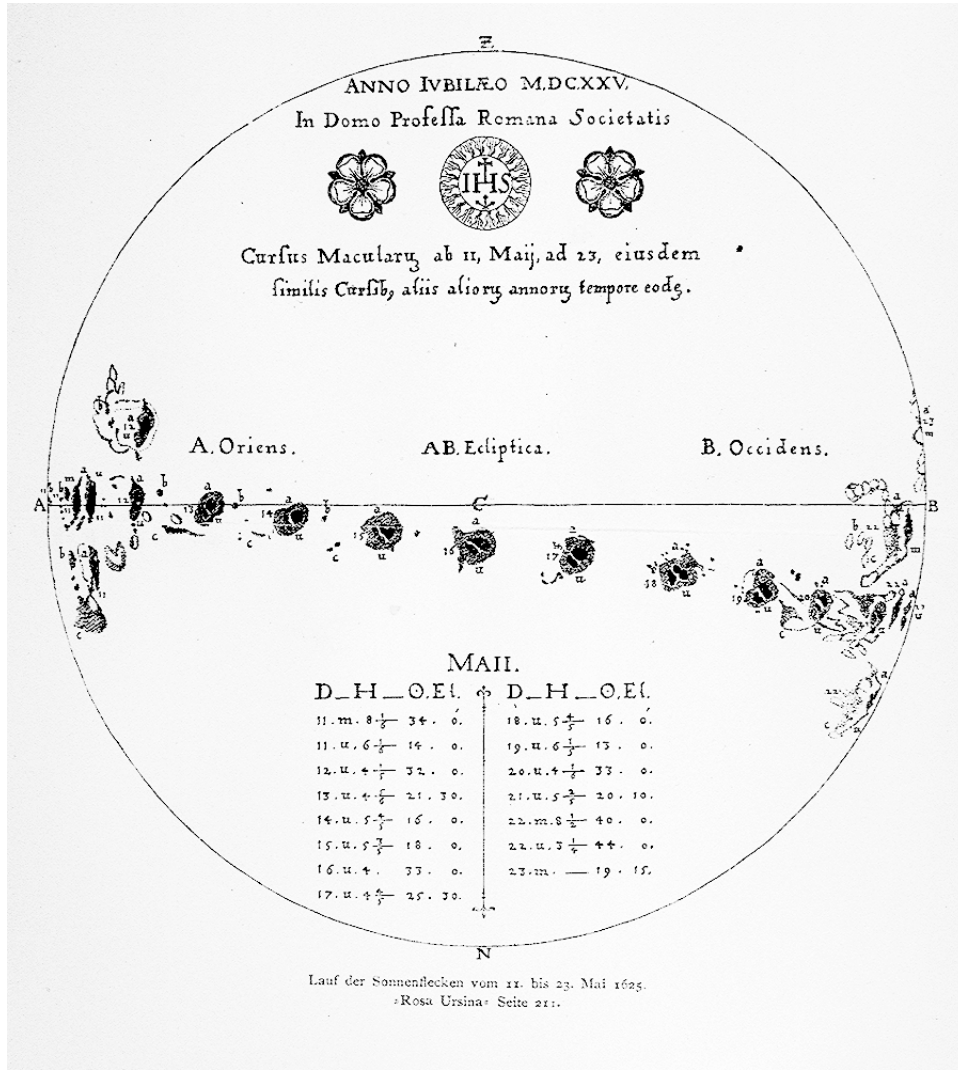


Figure 1.1: Sunspots sketch from 'Rosa Ursina' (1630) published by C. Scheiner.

spot ( $A$  MSH). The rule of the proportionality of the maximum area  $A$  of a sunspot group to its lifetime  $T$  (Gnevyshev, 1938; Waldmeier, 1955):

$$A = \bar{D}_{GW} T, \quad \bar{D}_{GW} \sim 10 \text{ MSH/day}. \quad (1.1)$$

Most spots decay by breaking up into smaller units, and these are then eroded over time by the convective turbulence around the periphery.

In the case of unipolar spot with penumbra, the diameter (including penumbra)  $\geq 2.5^\circ$ , Moreno-Insertis and Vázquez (1988) and Petrovay and van Driel-Gesztelyi (1997) found that decay rate proportional to the spot radius  $r$  is a good approximation:

$$\dot{A} \simeq -C_D r/r_0, \quad (1.2)$$

where  $r_0$  is the maximum radius, and  $C_D \approx 1.1 \times 10^9 \text{ m}^2\text{s}^{-1}$ . The rate indicates parabolic decay law for the sunspot area and it includes the fast initial decay phase.

The equation is also valid for the long-lived unipolar sunspots with penumbra.

### 1.1.2.3 Distribution

Mature spots begin life as pairs of opposite polarity pores, and that they grow by accumulation of other pores and even smaller neighboring magnetic elements. We call these spots ‘bipolar regions’. Today it is known that these pairs are connected by loops of magnetic field that arch through the solar corona. A pair spots across the disk of the sun as it rotates. A spot in the lead is called “leading spot” (preceding in the solar rotation), and the other in the rear called “following spot”. In most spot pairs, the line between the centers of the leading spot and the following spot is aligned almost east-west, although there is a slight tilt away from the exact east-west direction. The tendency of the tilt is clearly defined that the leading spot is situated at slightly lower latitudes (i.e., closer to the equator), while the following spot is situated at slightly higher latitudes. This definite tendency is called as “Joy’s law” (Hale, Nicholson and Joy, 1919; Brunner, 1930) named after Alfred H. Joy (1882-1973).

It is known that bipolar sunspots lack the symmetry (van Driel-Gesztelyi and Petrovay, 1990). The leading spots are more stable than following ones. The leading spots concentrate the dominant spots but the following spots tend to separate incoherent spot groups. The leading spots often keep longer life than the following spots.

It has been known that majority spots emerge between the equator area confined to the latitude  $\pm 35^\circ$  in general. At the latitudes greater than  $40^\circ$  sunspots are increasingly rare, small and short-lived.

### 1.1.2.4 Brightness and Temperature

The brightness of umbra is roughly 20-30% of the wavelength integrated flux of the quiet region (solar photosphere). The penumbra radiates 75-85% of the quiet region flux. The temperatures of umbra and penumbra are around 3900-4800K and 5400-5500K, respectively (Solanki, 2003).

Why sunspots have lower temperature than photosphere which is 6000K? As sunspots are made from bundles of magnetic flux tubes, the plasma ‘frozen’ in the tubes prevent thermal convection in the solar convection zone. This is why that sunspots are in lower temperature and darker than the photosphere.

### 1.1.3 Solar Cycle

One of the most important properties of the Sun is the periodicity of the sunspot activity, namely solar cycle. The solar cycle was discovered in 1843 by Samuel H. Schwabe (1789-1875), who after 17 years of observations noticed a periodic variation in the average number of sunspots. Solar cycles have an average duration of about 11

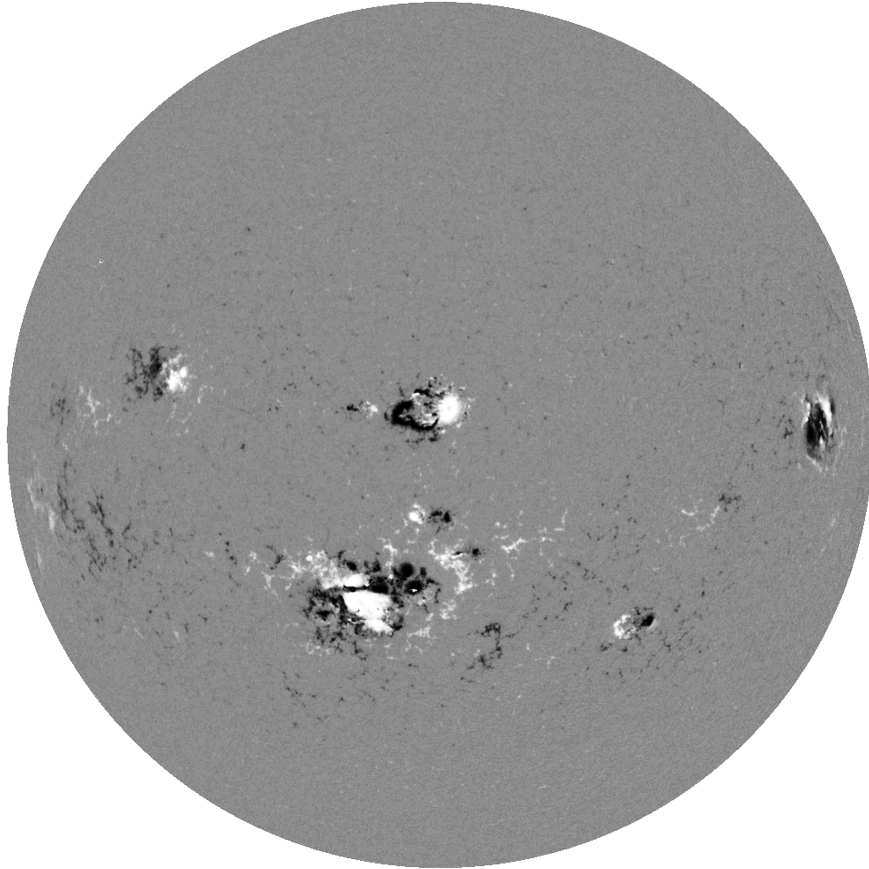


Figure 1.2: A Sample of Magnetogram image courtesy of SOHO/MDI. White (black) areas indicate positive (negative) polarity. There is no strong magnetic field in the gray area.

years. It is known that the cycle has the variations between eight and 14 years. At the beginning of a new cycle, a few spots emerge at latitudes around  $35\text{-}45^\circ$  in the both hemispheres. Over the course of the cycle, subsequent spots appear closer to the equator gradually, finishing at latitudes around  $7^\circ$ . By tradition, the cycle from 1755 to 1766 is the first solar cycle following the sunspot numbering scheme established by Rudolf Wolf (1816-1893).

#### 1.1.4 Magnetic Field

Development of magnetogram using the Zeeman splitting effect by George E. Hale (1868-1938) gave us significant information that the Sun has strong magnetic field (Hale, 1908). The example of the magnetogram obtained by SOHO/MDI is shown in Figure 1.2. In this figure, gray areas indicate that there is no magnetic field, while black and white areas indicate regions where there is a strong magnetic field. The magnetograms show “line-of-sight” magnetic fields. The white regions indicate positive magnetic polarity, while the dark regions indicate negative polarity. Mean magnetic

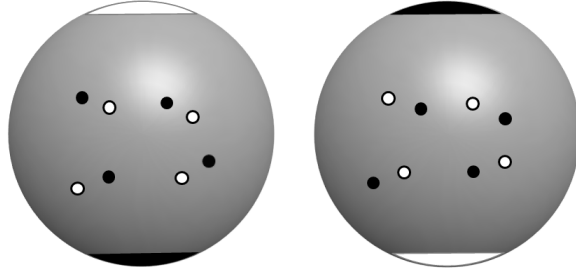


Figure 1.3: Cartoon of Hale-Nicholson polarity law. Both large spheres represent the solar photosphere. The small open and closed circles indicate positive and negative polarity, respectively. The magnetic polarity of leaders changes each solar cycle (see text).

field strength on the photosphere (quiet region) is around a few Gauss (G). The magnetic field strength of umbra reaches 2000-3000 G. In the case of the largest sunspot, the strength reaches 4000 G around the umbra. The magnetic field strength of penumbra gradually decreases with distance from the umbra, the strength fall to almost zero dramatically at the boundary with photosphere (quiet region).

When the sunspot diameter are within the range of 3500-60000 km with the average magnetic flux density of 1500 G, the total magnetic flux is estimated at  $1 \times 10^{19}$ - $4 \times 10^{22}$  Mx.

The appearance of sunspots is caused by solar magnetic activity. As a result of emergence of magnetic flux tube which is thought to be formed at the deep part of the convection zone, sunspot appears as the cross-section of the flux tube on the photosphere. Then the sunspots almost always have the pairs of opposite polarity.

Localized strong magnetic fields originated from the magnetic flux emergence are emerging flux regions (EFRs) (Zirin, 1972). Major energy release phenomena from the solar surface, namely solar flares, coronal mass ejections (CMEs), etc., are often observed near the periphery of sunspots. Then we call the periphery of sunspots 'active region' (AR).

#### 1.1.4.1 Hale-Nicholson Polarity Law

Sunspots often emerge in bipolar pairs, roughly along an east-west line, a leader that is further west than the followers as mentioned in section 1.1.2. All the leaders in the northern hemisphere have the same magnetic polarity during one solar cycle, all those in the southern hemisphere have the opposite polarity (we can see the clear order in Figure 1.2). These polarities reverse during the next cycle. The polarities at the poles also reverse every cycle. These patterns were first determined observationally

in the early 20 century by G.H. Hale and his colleagues. Then they are known as Hale-Nicholson Polarity Law (Hale and Nicholson, 1925).

In an odd number-cycle, all leaders (followers) in the northern (southern) hemisphere have positive (negative) polarity. In that cycle, the north (south) pole has positive (negative) polarity (see Figure 1.3). To return to the original magnetic condition, it takes twice the solar cycle. Then the solar magnetic cycles have the duration of around 22 years.

#### 1.1.4.2 Mt. Wilson Magnetic Classification

Sunspots come not only in all sizes but also in all shapes. Some groups of sunspots have a more complex magnetic structure than other sunspot groups and are more likely to produce solar flares. To estimate the flare productivity of a sunspot group, we can utilize Mount Wilson magnetic classification as the morphological indexes. Hale *et al.* (1919) made rules of a certain magnetic classification for every sunspot group at Mount Wilson observatory. Based on Künzel's study (1960),  $\delta$ -types were added later. Every sunspot group is classified into eight types as follows (see also Figure 1.4 adapted from US Air Force Weather Agency Manual 15-1<sup>1</sup>).

$\alpha$  : A unipolar sunspot group.

$\beta$  : A sunspot group that has a positive and a negative polarity (or bipolar) with a simple division between the polarities.

$\gamma$  : A complex region in which the positive and negative polarities are so irregularly distributed that they can't be classified as a bipolar sunspot group.

$\beta\gamma$  : A bipolar sunspot group but complex enough so that no line can be drawn between spots of opposite polarity.

$\delta$  : The umbrae of opposite polarity in a single penumbra.

$\beta\delta$  : A sunspot group with a general beta magnetic configuration but contains one (or more) delta sunspots.

$\beta\gamma\delta$  : A sunspot group with a beta-gamma magnetic configuration but contains one (or more) delta sunspots.

$\gamma\delta$  : A sunspot group with a gamma magnetic configuration but contains one (or more) delta sunspots.

It is known that  $\delta$ -type sunspots can be very active and produce the most intense solar flares. We will compare the flare activity of three representative types, namely  $\beta$ ,  $\beta\gamma$ , and  $\beta\gamma\delta$ , in Chapter 2.

<sup>1</sup><http://static.e-publishing.af.mil/production/1/afwa/publication/afwaman15-1/afwaman15-1.pdf>

UNIPOLAR GROUPS	ALPHA ( $\alpha$ )	
	ALPHA p ( $\alpha\rho$ )	
	ALPHA f ( $\alpha F$ )	
BIPOLAR GROUPS	BETA ( $\beta$ )	
	BETA p ( $\beta\rho$ )	
	BETA f ( $\beta F$ )	
	BETA - GAMMA ( $\beta\gamma$ )	
COMPLEX GROUPS	GAMMA ( $\gamma$ )	
	GAMMA - DELTA ( $\gamma\delta$ )	

Figure 1.4: Mount Wilson magnetic classification adapted from US Air Force Weather Agency Manual 15-1 (p. 37, figure 4.4). In this figure, ‘p’ and ‘f’ mean ‘preceding spot’ and ‘following spot’, respectively. The subclasses for ‘p’ and ‘f’ are not utilized in this study. Left side of this figure is West.

### 1.1.5 General Morphological Models for EFRs

The morphological model of EFR, which is obtained from motion of sunspots and magnetic features on the photospheric surface and temporal evolution of the structure in the chromosphere, is  $\Omega$ -loop emerging model (Zwaan, 1985; Figure 1.5).

We will take a general view of the evolution of EFR. The first manifestation of EFR is the appearance of a small and compact “plage” in the chromosphere (Fox, 1908; Waldmeier, 1937; Sheeley, 1969). Plage is the bright area in the chromosphere. Also around that time a tiny bipolar magnetic element is observed in magnetogram. The arch filament system (AFS) also becomes visible in the  $H\alpha$  line core. Roughly parallel dark fibrils connect opposite polarity in the AFS (Bruzek, 1967, 1969). The first AFS appears in  $H\alpha$  1-1.5 hour after the initial brightening (Glackin, 1975; Kawaguchi and Kitai, 1976). Ascending speed of the loop top of AFS reaches  $10\text{-}15 \text{ km s}^{-1}$ . In both legs, matter downflows occur with  $30\text{-}50 \text{ km s}^{-1}$ . The downflow motion is also detected

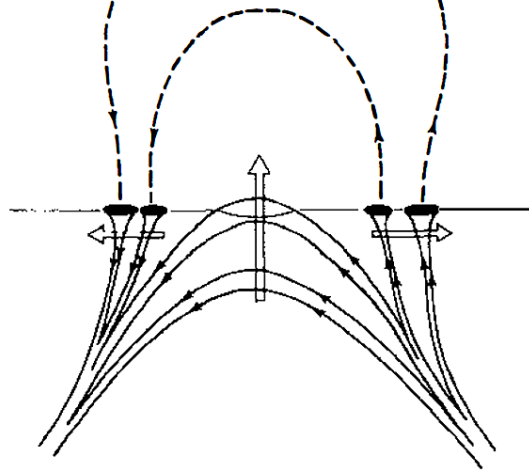


Figure 1.5:  $\Omega$ -loop emerging model (Zwaan, 1985). Broad arrows indicate local displacements of flux tubes.

in the photosphere with the speed of  $1\text{-}2 \text{ km s}^{-1}$  near pores (Kawaguchi and Kitai, 1976; Brants and Steenbeck, 1985). The opposite polarity of AFS move apart at a rate around  $1\text{-}2 \text{ km s}^{-1}$  (Harvey and Martin, 1973).

## 1.2 $\delta$ -Spots

Sunspots which have opposite polarity umbrae within common penumbra are called ‘ $\delta$ -spots’. (Künzel, 1960). The properties of the solar magnetic fields which showed strong and prolific flare activity are the development of magnetic shear and the increase of magnetic complexity. Magnetic gradient also increases in the magnetic fields generally. Well developed  $\delta$ -spots have all of these properties and are well known that they show higher flare activity than the other sunspot types (Tanaka, 1975; Zirin and Ligget, 1987; Sammis *et al.*, 2000).

Many  $\delta$ -spots disobey Hale-Nicholson law. Some  $\delta$ -spots show the magnetic distributions are in exact reverse of Hale-Nicholson law.  $\delta$ -spots tend to be compact compared with another sunspot types. As the umbrae with opposite polarity lie next to each other, the magnetic intensity near the magnetic neutral line is strong and the magnetic gradient is so large (Severny, 1960). In contrast, general bipolar magnetic fields have weak magnetic intensity around the neutral line and the magnetic gradient rarely develops. In addition, it is often observed that the magnetic fields of  $\delta$ -spot are strongly sheared along with the magnetic neutral line (Zirin and Ligget, 1987; Lites *et al.*, 1995). It is considered that the magnetic free energy is accumulated in the sheared (or twisted) magnetic force lines.

Moreover,  $\delta$ -spots have the property that the opposite polarity umbrae rotate each other as they grow (Tanaka, 1991; Leka *et al.*, 1996).

The correlations between magnetic shear and flare occurrence were pointed out that by several authors (Rust, Nakagawa and Neupert, 1975; Hagyard *et al.*, 1984; Gaizauskas, 1989). Kurokawa (1987) pointed out that the magnetic shears are developed by two ways: the collision between opposite polarities of different sunspots and the emergence of pre-twisted magnetic flux tube. Wang (1992) claimed adding to the above that the head on collision of opposite polarities promotes the growth of the magnetic shear.

### 1.2.1 Formation Paths of $\delta$ -Spots

Zirin and Liggett (1987) introduced the formation of  $\delta$ -spots which show the energetic flare activity as following three ways:

i) emergence of a single complex active region (AR) formed below the surface, *i.e.*, so-called “island  $\delta$ -spot”, ii) emergence of large satellite spots near a larger older spot, and iii) collision of spots of opposite polarity from different dipoles.

Tang (1983) concluded that the  $\delta$ -formation is attributed by the contribution of two different dipoles. The reasons are differences of expanding directions and speeds between two EFRs. However, if the magnetic flux tubes are strongly and intricately writhed, they are not evidence of the disconnection of the dipoles. We will discuss the possibility of connectivity of the two EFRs paying attention the handedness of the twist and writhe in Chapter 3.

### 1.2.2 Flare Activity

#### 1.2.2.1 Solar Flare

Solar flare is the most energetic phenomenon in our solar system. The energy of major flares reaches  $10^{22}$ - $10^{25}$  J.

The solar flare is a phenomenon that releases stored magnetic energy in AR in very short period. However the flares not always occur in every AR. It is known that the flare activity is more active in the ARs with more magnetic complex configuration. Although solar flares are brightening in the extreme ultra violet line and the X-ray, they are well observed in  $H\alpha$  from the ground observatories. By morphological flare observations in  $H\alpha$  line, the characteristics of many flares are known as “homologous” and “sympathetic”. That is to say, flares occur in the specific location repeatedly (Waldmeier, 1938). Almost all flares occur near the neutral line of AR with concentrated and complex magnetic field. It is also known that strong flare occurs when strong shear structure is seen around the neutral line. It is also pointed out that flares occur easily when new magnetic field emerges near the existing magnetic structure.



Table 1.1: Soft X-ray flare classification

class	Peak Flux Range (1-8 Å) Intensity $\phi$ ( $Wm^{-2}$ )
A	$\phi < 10^{-7}$
B	$10^{-7} \leq \phi < 10^{-6}$
C	$10^{-6} \leq \phi < 10^{-5}$
M	$10^{-5} \leq \phi < 10^{-4}$
X	$10^{-4} \leq \phi$

### 1.2.2.2 Classification of Flares

Although there are several methods to estimate the flare activity level, the classification based on the signal intensity of the soft X-ray is used broadly. Flares are classified A, B, C, M and X based on the integrated value of 1-8 Å of soft X-ray when the flare occurred. The regular observation of solar soft X-ray continues from 1990s by the successive *GOES* satellites. The classification of flares based on the soft X-ray intensity are shown in Table 1.1.

In this thesis, to estimate the total flare activity level of each AR, the value named “Flare Index” (FI) is adopted. The definition is as follows.

$$FI = 1.0 \times \sum_i m_C + 10.0 \times \sum_j m_M + 100.0 \times \sum_k m_X, \quad (1.3)$$

where  $m_C$ ,  $m_M$ , and  $m_X$  are the GOES soft X-ray peak intensity magnitudes (from 1.0 to 9.9) of flares of class C, M and X. The indices  $i$ ,  $j$ , and  $k$  are the number of flares of each classes per a period respectively (*cf.* Antalová, 1991).

### 1.2.3 Observational Model of $\delta$ -Spot

Several authors proposed the schematic model for individual cases of  $\delta$ -type spot evolution (e.g. Ishii *et al.*, 1998; Kurokawa *et al.*, 2002). For example, the schematic model proposed by Kurokawa *et al.* (2002) is shown in Figure 1.6. In these works, they suggest that the emergence of a twisted magnetic flux rope must be the source of strong shear development in an AR to produce a strong flare activity. As their studies are limited to the several individual cases, so their generality are not enough. Ikhsanov *et al.* (2003) proposed the morphologies of  $\delta$ -spot based on their empirical studies. They have classified magnetic topology of interaction between two major emerging flux tubes in three types, namely “vertical (top-by-top) collision”, “lateral (side-by-side) collision”, and “frontal (foot-by-foot) collision”. However their magnetic topology is confined above the solar surface and the validity of their model has not been verified well.

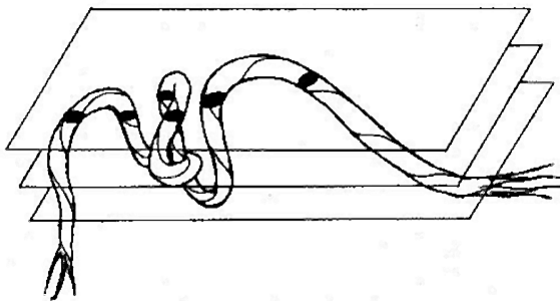


Figure 1.6: Schematic drawing of an emerging twisted flux rope adapted from Kurokawa *et al.* (2002) . The photospheric surfaces relative to the emerging flux rope are drawn at three successive times, T1, T2, and T3, and the locations of the sunspots or the cut ends of the flux rope at the photospheric surface at T1.

#### 1.2.4 Magnetic Helicity

The magnetic helicity is a physically useful quantity because it is well conserved in a closed volume (Berger and Field, 1984) . Magnetic helicity of a magnetic field  $\mathbf{B}$  within a volume  $V$  is defined by:

$$H = \int_V \mathbf{A} \cdot \mathbf{B} dV, \quad (1.4)$$

where the vector potential  $\mathbf{A}$  satisfies

$$\mathbf{B} = \nabla \times \mathbf{A}. \quad (1.5)$$

The magnetic helicity is a topological quantity for the twisting number or the linking number of the field line. Then, the next formula is established in the thin flux tube model:

$$H = (T_w + W_r)\phi^2, \quad (1.6)$$

where  $T_w$ ,  $W_r$ , and  $\phi$  are the twist, the writhe, and magnetic flux density along the flux tube, respectively. The twist is a measurement of winding number of the field lines about the magnetic axis of the rope, while the writhe is a quantity of the helical deformation of the magnetic flux axis itself (Török *et al.*, 2010).

##### 1.2.4.1 Helical Structures of Solar Surface

Helical structures in the solar atmosphere, representing twist and writhe, have been observed in various scales and at various heights. For example, Hale (1927) and Richardson (1941) were the first to mention the hydrogen vortices surrounding sunspots, so-called “sunspot whirls”, as helical structures. Coronal sigmoids (Rust and Kumar, 1996) had been also investigated in terms of their helicity patterns. The fantastic coronal sigmoid images obtained with *Hinode* X-ray telescope are shown in Figure 1.7.

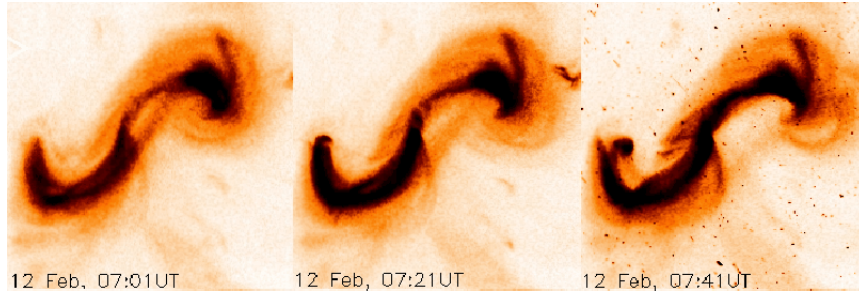


Figure 1.7: Sample images of coronal sigmoid with *Hinode* satellite adapted from Mackenzie and Canfield (2008).

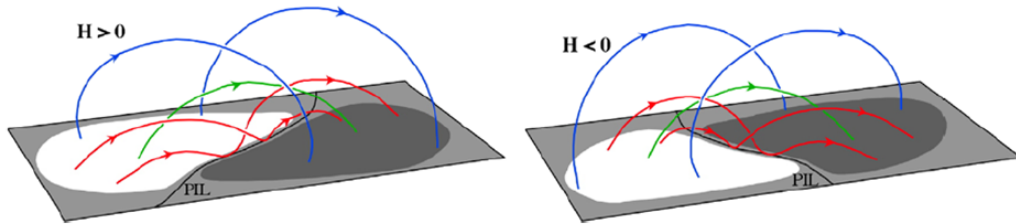


Figure 1.8: Magnetic Tongue patterns adapted from Luoni *et al.* (2013). Magnetic tongue patterns are direct signature of the emergence of a twisted flux tube. Elongation structure is due to the projection of the azimuthal magnetic field on the vertical direction.  $H$  and PIL mean Helicity sign and Polarity Inversion Line, respectively. Polarity inversion line means the same as neutral line.

#### 1.2.4.2 Magnetic Helicity Signs and Handedness

Recently, it has been developed that “magnetic tongue” is useful parameter to judge the magnetic helicity sign of the emerging field (López-Fuentes *et al.*, 2000; López-Fuentes *et al.*, 2003; Luoni *et al.*, 2011). Magnetic tongues are the elongated polarities distributed as if to follow the main polarities on the both sides of the magnetic neutral line. They can be interpreted as the sign of the azimuthal component in a twisted emerging flux tube. The distribution of the magnetic tongues to the neutral line can be used as proxy of the helicity sign of the emerging magnetic field. Magnetic tongue patterns are shown in Figure 1.8.

In the next chapter, the statistical study of flaring ARs in Cycle 23 will be introduced as preliminary investigation to advance this study.



## Chapter 2

# Preliminary Statistical Study of Sunspots in Cycle 23

In this chapter, the statistical property of various ARs which appeared in Cycle 23 will be shown as a back ground information of the study of  $\delta$ -spots. Particularly, we will show prominent property of  $\beta\gamma\delta$ -type ARs among all flare active ones by the statistical study. Based on this preliminary study, the main purpose of this thesis will be stated in a more detailed and concrete way.

Sammis *et al.* (2000) investigated the relationships among AR size, peak flare soft X-ray flux, and magnetic classification mainly using data of Cycle 22. Then they confirmed that  $\beta\gamma\delta$  spots produce many larger flares than other type spots of comparable size (Figure 2.1). There is a general trend for large ARs to produce large flares. However the dependence on magnetic class to produce large flares is more significant than that on the AR sizes (Figure 2.2). We investigate the flare activity of ARs in Cycle 23 referring Sammis's study in this chapter.

### 2.1 Data Set

To extract magnetic class of ARs in Cycle 23, we based on the following two data catalogues. One is USAF-MWL (known as USAF-SOON) ([ftp://ftp.ngdc.noaa.gov/STP/SOLAR\\_DATA/SUNSPOT\\_REGIONS/USAF\\_MWL](ftp://ftp.ngdc.noaa.gov/STP/SOLAR_DATA/SUNSPOT_REGIONS/USAF_MWL)) and the other is USAF/NOAA sunspot data (<http://solarscience.msfc.nasa.gov/greenwch.shtml>). The former is a merged one of the daily solar reports of six ground based observatories and the latter mainly consists of the data based on the space observations after the launch of SOHO spacecraft. When the type of an AR is assigned differently in the two catalogues, we choose the more complex one for the region as the representative of the day. In this way, we extract daily magnetic class of each AR. We treat the most complex type in the evolution of each AR as representative class hereafter.

We also use *GOES* 1-8 Å flux data to estimate the flare activity level of each ARs.

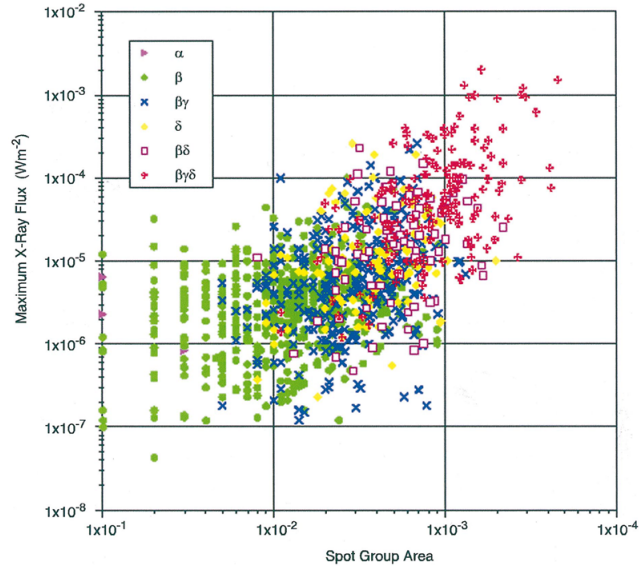


Figure 2.1: Relations between Maximum Area and Peak X-ray flux with each magnetic type adapted from Sammis *et al.* (2000).

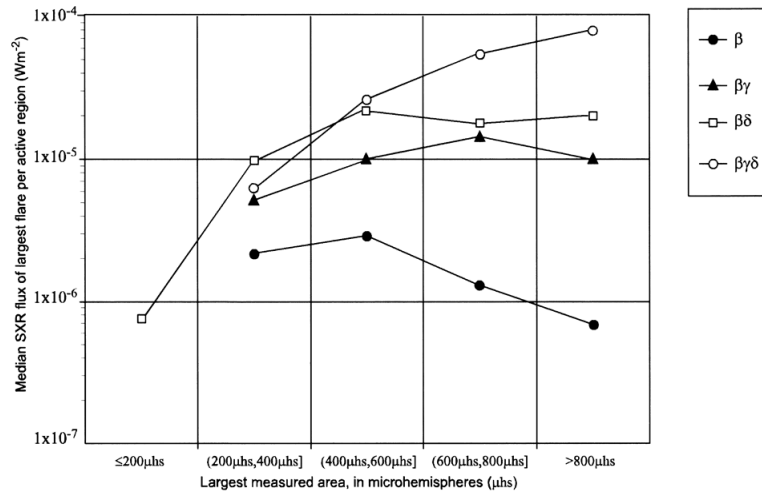


Figure 2.2: Median peak intensity of flares for different magnetic classes as a function of area adapted from Sammis *et al.* (2000).

## 2.2 Overview of Flare Activity in Cycle 23

The number of ARs with the exception of  $\alpha$ -type is 2868 in Cycle 23. Among them, 1188 ARs yield C1.0 flare or above (41.4%). The flaring ratios of each type based on Mt.Wilson classification are shown in Table 2.1. As shown in Table 2.1, 94% of ARs which reached  $\delta$ -types yield C1.0 flare or above. In the case of  $\beta\gamma\delta$ -type, the ratio is 98.5%. On the other hand, the flaring ratios of ARs which reached  $\beta\gamma$  and  $\beta$  are 69% and 22%, respectively. From these results, it is clear that the higher flare activity is shown in the more complex magnetic configuration. Although  $\delta$ -type is divided into several sub-types, to avoid complications we concentrate to analyze  $\beta\gamma\delta$ -type, which can be considered as the most developed and the highest flare active group, hereafter.

Table 2.1: Flaring Ratio of each magnetic class in Cycle 23

Magnetic type	Flaring ARs	Total ARs	Flaring Ratio (%)
$\beta\gamma\delta$	197	200	98.5
$\gamma\delta$	6	7	85.7
$\beta\delta$	40	45	88.9
$\delta$	107	121	88.4
( $\delta$ types total)	(350)	(373)	(93.8)
$\beta\gamma$	434	630	68.9
$\beta$	404	1860	21.7
$\gamma$	0	5	0.0
	1188	2868	41.4

### 2.2.1 Relation between Maximum Area and Flare Index

For flaring ARs, the relations between maximum area and FI of three types, namely  $\beta$ ,  $\beta\gamma$ , and  $\beta\gamma\delta$ , are shown in Figure 2.3. From these panels in Figure 2.3, more complex type has larger slope of the fitting curve. Two methods were used to get the index  $k$  of the power law function  $\propto x^k$ . The first one is the classical least square fitting (C-LS) to logarithmic values of abscissa and ordinate. Second one is the non-linear least square fitting (NL-LS) method based on Gauss-Newton algorithm (*cf.* Hansen *et al.*, 2012). The data scattering from the curve tend to be smaller in the more complex type. Especially in the graphs of  $\beta\gamma\delta$  and three types combined, it seems to have scaling law with the power index of 2 for the non-linear least-square regression. This value is consistent with the result of numerical simulation for twisted emerging flux tube by Magara (2014). We will discuss this topic in detail in Section 3.4 of Chapter 3.

### 2.2.2 Relation between Lifetime and FI

The Sun has the rotation period of around 28 days to the earth (or the observing satellite). Then the ARs moving across the solar disk can be observed 14 days at the most. As the regular space observation of solar invisible side is unrealized yet, we cannot know the real lifetime of ARs unfortunately. In spite of the restriction, we can compare the observed days of magnetic types from the data set. We use the observed days of AR based on the data set described in Section 2.1 as the proxy of the lifetimes of AR. To avoid complications, we call this values “lifetime” of AR hereafter. As shown in Figure 2.4, ARs with more complex magnetic type tend to have longer lifetime. When we compare the flaring ARs to the no-flaring ARs, the flaring ARs have about 20% longer lifetime than the no-flaring ARs in the all types (Table 2.2).

Table 2.2: Comparison to lifetimes of flaring and no-flaring ARs with three magnetic class (days). The upper column shows the average lifetimes and the standard deviations for the flaring ARs. The lower column shows the average lifetimes and the standard deviations for the no-flaring ARs. As only three ARs of  $\beta\gamma\delta$ -type ARs are no-flaring ones, the values are shown in parentheses.

	$\beta\gamma\delta$	$\beta\gamma$	$\beta$
Avg.	12.90	11.21	9.37
SD	1.79	2.57	3.21
Avg.	(9.67)	9.82	6.67
SD	(2.31)	2.96	3.66

### 2.2.3 Histograms of Maximum Area, FI, and Lifetime

We will show the histograms of Maximum Area, FI, and lifetime for  $\beta$ ,  $\beta\gamma$ , and  $\beta\gamma\delta$ -types ARs in Cycle 23 as a supplement to previous sections (Figure 2.5).

All the histograms are relative ones normalized by the total count for each category. The median values are shown for all the distribution.

We can confirm that more complex class has larger median value in every category.



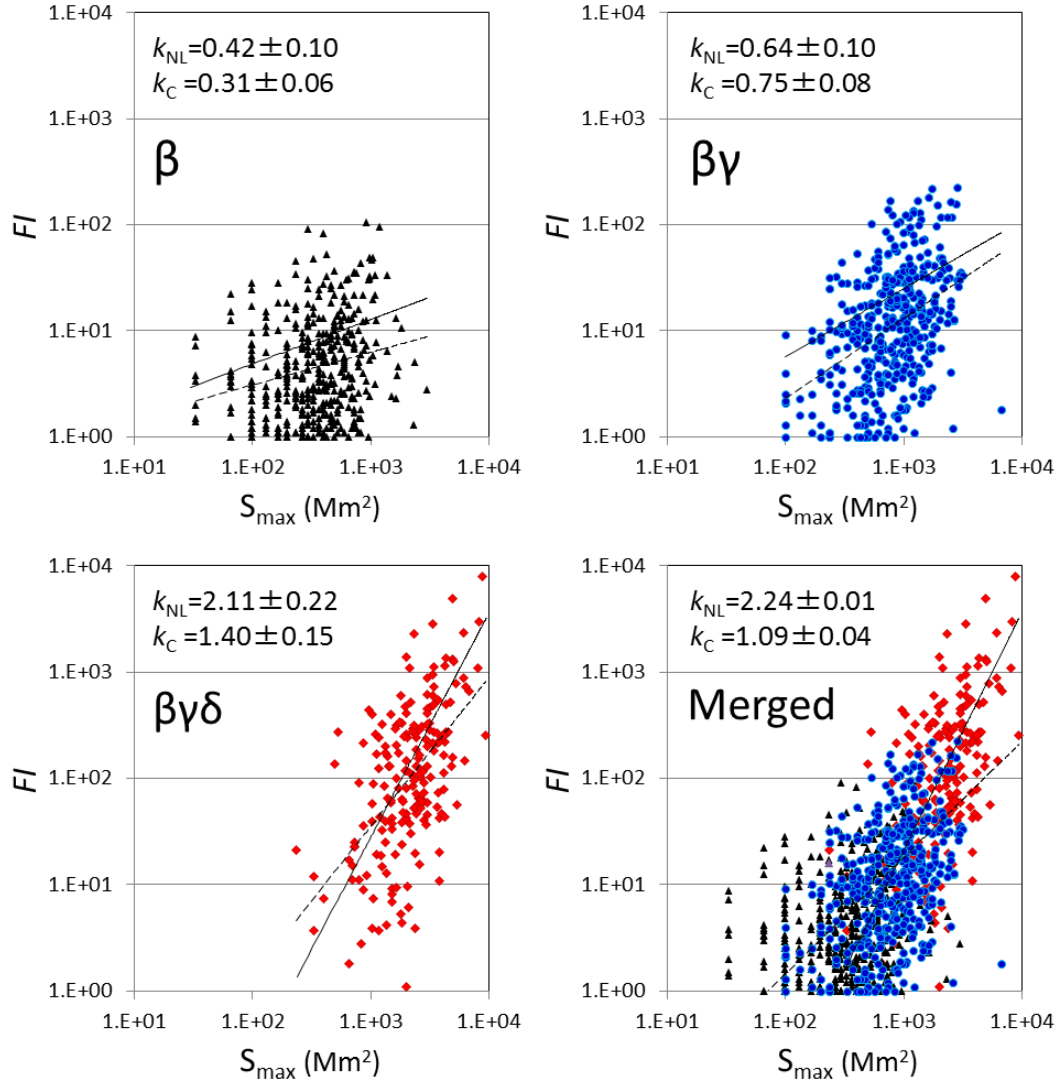


Figure 2.3: Relations between Maximum Area and Flare Index of three magnetic types. Black triangles, blue circles, red diamonds represent  $\beta$ -type,  $\beta\gamma$ -type, and  $\beta\gamma\delta$ -type ARs, respectively. The results of non-linear least-squares fitting (power-law index  $k_{NL}$ ) and classical least-squares fitting (power-law index  $k_C$ ) are shown by the solid and the dashed lines, respectively.

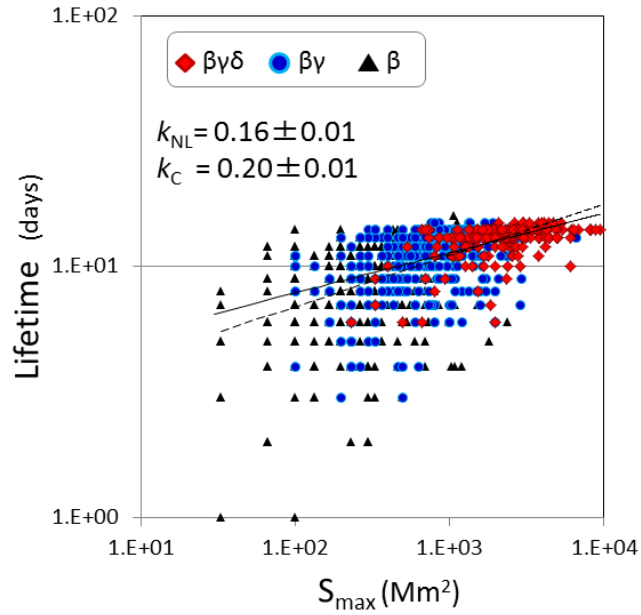
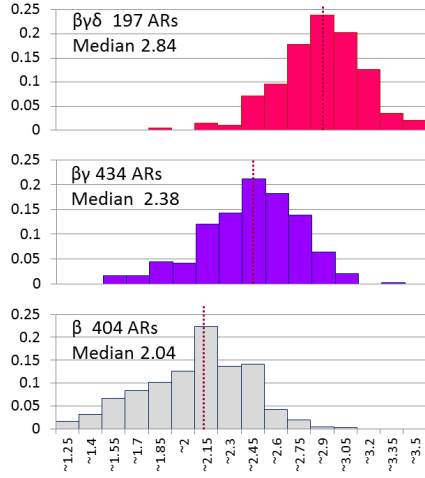
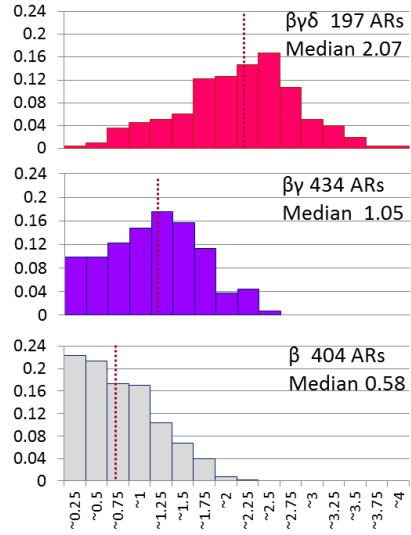


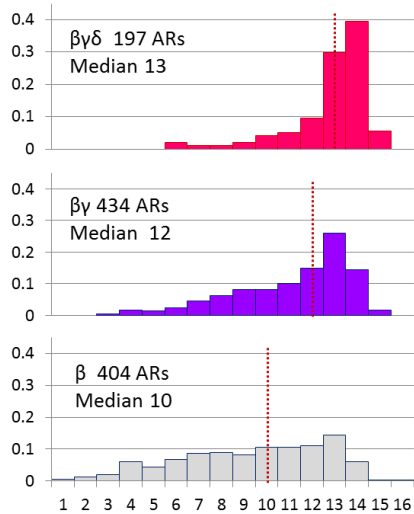
Figure 2.4: Relations between Maximum Area and Lifetime of three magnetic types. Upper limit of lifetime of ARs is around about 14 days on the visible solar disk. The symbols are the same as in Figure 2.3.



(a)  $\log_{10}(\text{Maximum Area})$



(b)  $\log_{10}(FI)$



(c) Lifetime

Figure 2.5: histograms of Maximum Area, FI, and Lifetime for  $\beta$ ,  $\beta\gamma$ , and  $\beta\gamma\delta$ -types ARs in Cycle23

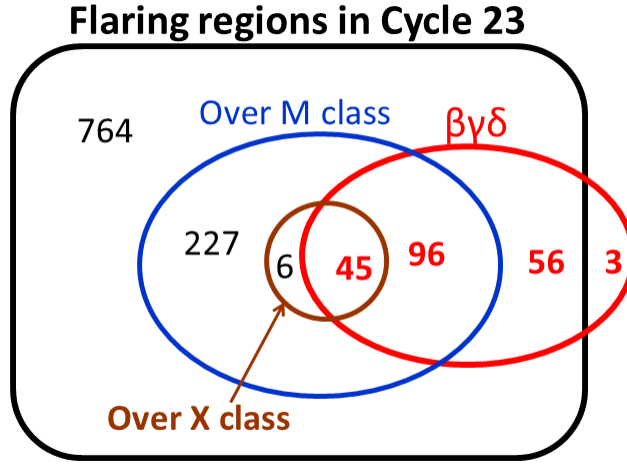


Figure 2.6: Count of flaring ARs in Cycle 23 classified by the soft X-ray level. The numbers mean the ARs contained in each separated regions.

#### 2.2.4 Position of $\beta\gamma\delta$ -Spots among All Flaring ARs

We classified all the ARs in Cycle 23 according to their levels of the flares. We will show the result in the Venn diagram format (Figure 2.6). The diagram is classified by soft X-ray flare level. The black circle includes the number of ARs which yield C1.0 flare or above. The blue circle includes the number of ARs which yield M1.0 flare or above. The brown circle includes the number of ARs which yield X1.0 flare or above. The red circle shows the numbers of  $\beta\gamma\delta$ -spots of each category described above.

Although there are three  $\beta\gamma\delta$ -spots without flare activity, we can also confirm the highest flare activity of  $\beta\gamma\delta$ -spots among all flaring ARs from this diagram. As the three inactive  $\beta\gamma\delta$ -spots reached the west limb of solar disk during their evolution, it is uncertain whether these ARs yield flare or not in their total evolutions. In any case, it is certain that there are inactive  $\beta\gamma\delta$ -spots. We will discuss this point of view in the next subsection concisely.

#### 2.2.5 Relation between $\delta$ -Days and FI

In this thesis, the author will pay attention on the duration of  $\delta$ -state for  $\delta$ -spots. The  $\delta$ -state in an AR was not always continuous. If  $\delta$ -state was appeared intermittently in an AR, we integrated all days which were reported as  $\delta$ -class. The value thus obtained is called “ $\delta$ -days” in this chapter. The ARs with the longer  $\delta$ -days tend to be the higher flare active in general as shown in Figure 2.7. However the trend has large dispersion in FI values for a given “ $\delta$ -day” values, the FI distributes from larger values to the smaller ones, which means that there are a variety of active region in  $\delta$ -spots in the view point of flare productivity. What is the difference between flare-active and flare-inactive  $\delta$ -

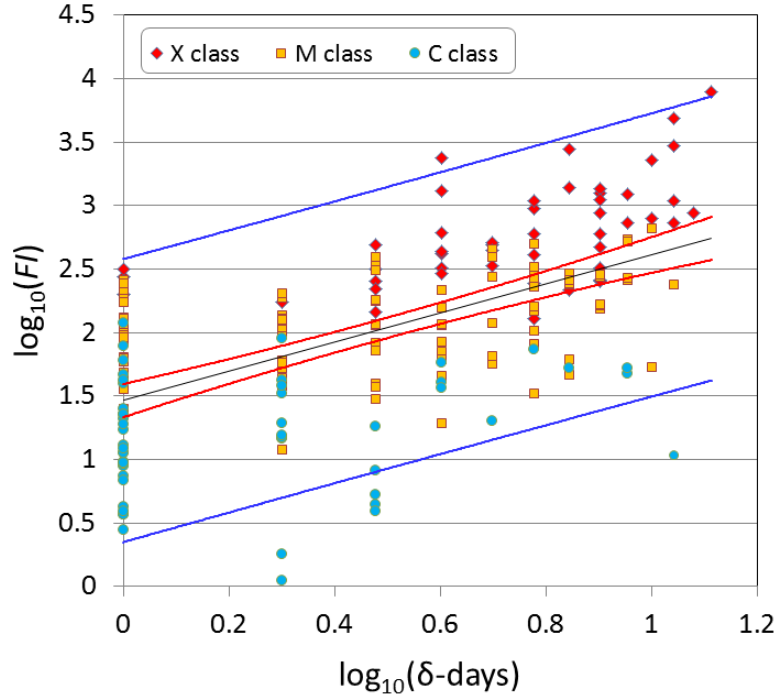


Figure 2.7: Relation between  $\beta\gamma\delta$ -state days and Flare Index of  $\beta\gamma\delta$ -type ARs. The red diamond, orange square, and blue circle mean the ARs that yielded X-class flare, M-class flare, and C-class flare as the maximum flare, respectively. The red lines and green lines indicate 95 % confidence lines and 95 % prediction lines, respectively.

spots? The question motivated the author to study the magnetic and morphological evolution of  $\delta$ -spots in details.

### 2.3 Purposes of This Thesis

Sometimes the largest solar flares affect the environment of the Earth. The telecommunication system and the electric power stations are damaged by them for example. That is why, it is important to investigate the energetic solar phenomena for us. We sometimes call such an investigation as “space weather report”. If we find the conditions of major flares, we can contribute the space weather forecast.

After the launch of SOHO satellite in 1995, the regular solar observation from space was achieved. The SOHO satellite supplied the various data, namely magnetograms, intensitygrams, dopplergrams, and so on, through the whole Cycle 23. Therefore we can perform precise study of ARs through the solar cycle, statistically.

As described previously, it is well known that  $\delta$ -spots are prolific and energetic on their flare activity. However, it is still not clear which conditions drive the high flare activity of  $\delta$ -spots. So the author tries to find such conditions in this thesis by a systematic study with continuous observation.

Among all the  $\delta$ -spots in Cycle 23, we selected those which can be studied from their births on the visible solar disk to make clear the magnetic connection between component spots. The result is described in detail in Chapter 3. The thesis also studies how  $\delta$ -spots decay in their last stage. The report of this point of view will be done in Chapter 4.

## Chapter 3

# Evolution and Flare activity of $\delta$ -Sunspots in Cycle 23

### 3.1 Introduction

A sunspot group with umbrae of opposite polarity within a single common penumbra is called the  $\delta$ -sunspot group (Künzel, 1960). It is well known that major flares almost always occur in  $\delta$ -sunspot groups (Tanaka, 1975; Zirin and Liggett, 1987; Sammis *et al.*, 2000). Hence, investigation of the formation and evolution of the  $\delta$ -configuration is the key in understanding the major flare activities.

Zirin and Liggett (1987) classified the formation of  $\delta$ -spots in three types as follows: i) Emergence of a single complex active region (AR) formed below the surface, *i.e.*, the so-called “island  $\delta$ -spot”, ii) emergence of large satellite spots near a larger and older sunspot, and iii) collision of sunspots of opposite polarity from different dipoles. Then Ikhsanov *et al.* (2004), from their morphological study of  $\delta$ -spots, classified the magnetic topology of collisional interaction between two major emerging flux tubes into three types, namely “vertical (top-by-top) collision”, “lateral (side-by-side) collision”, and “frontal (foot-by-foot) collision” (see also Ikhsanov and Marushin, 2003). Although these researches show a variety of ways of  $\delta$ -spot formation, they did not give us a detailed physical view of the formation of  $\delta$ -spots. This is because their classifications were phenomenological.

Succeeding researches (Kurokawa, 1987; Tanaka, 1991; Leka *et al.*, 1996, van Driel-Gesztelyi, 1997; Ishii *et al.*, 1998; Linton *et al.*, 1999; Fan *et al.*, 1999; López Fuentes *et al.*, 2000) have found several physical characteristics of active  $\delta$ -spots, in that they have strong magnetic shear structures in their magnetic neutral line area and that their opposite polarities rotate around each other. These characteristics were interpreted as due to the emergence of a kinked flux rope. Ishii *et al.* (1998) and Kurokawa *et al.* (2002) proposed a model of  $\delta$ -spot that the emergence of a twisted magnetic flux rope is the source of strong shear which produces strong flare activities. Poisson *et al.* (2013) suggested a model of  $\delta$ -spot as the emergence of a deformed single tube which have

downward convex structure at its middle part with kinking. Thus the twist and writhe of magnetic rope is now thought as a key factor for the development of  $\delta$ -spot and the associated flare activities which sometime show sigmoidal morphology (Rust and Kumar, 1996).

Although a number of case studies revealed the important characteristics of  $\delta$ -spot evolution, we have not yet had a conclusive observational and physical view of the  $\delta$ -spot formation. In this article, we tried to obtain more clues on this issue by surveying the  $\delta$ -spots in solar activity cycle 23 paying attention to magnetic helicity (twist and writhe). Among all the  $\delta$ -spots in Cycle 23, we selected those which can be studied from their birth on the visible solar disk in order to unambiguously study the magnetic connection between component sunspots in a group. Further we limited the samples to the  $\beta\gamma\delta$  regions, as they are thought to have the highest flare activities (Sammis *et al.*, 2000).

SOHO/MDI images were used to follow the evolution of the ARs.

Our study shows that the flare-active  $\delta$ -spots are mainly formed by the emergence of writhed and twisted magnetic tubes, which appear as a quadrupolar magnetic configuration on the photosphere. Even the appearance of a more complex  $\delta$ -configuration can be interpreted as a modification to this basic configuration. On the other hand, the flare activity is low when the magnetic tubes in the  $\delta$ -configuration show insignificant writhe or twist.

In Section 2, we describe the data used in our study and the analysis method. In Section 3, we present our detailed analysis on some representative cases and summarize our statistical analysis. Finally, we give discussion on our results and our conclusions in Sections 4 and 5, respectively.

## 3.2 Data and Analysis

### 3.2.1 Region Selection

To select  $\beta\gamma\delta$  ARs in Cycle 23, we based our study on the following two data catalogues: USAF-MWL (also known as USAF-SOON) <sup>1</sup> and USAF/NOAA sunspot data <sup>2</sup>. The former data base is compilation of daily solar reports of six ground-based observatories. The latter mainly consists of data based on space observations after the launch of the SOHO spacecraft. When the type of an AR is assigned differently in the two catalogues, we choose the more complex one of the region as the representative. In this way we selected 200  $\beta\gamma\delta$  regions which are classified so at least once during their lifetime. Four ARs classified as  $\beta\gamma\delta$  in the catalogues were excluded from our dataset as they showed no sign of  $\delta$ -type in our visual check with SOHO/MDI images. Finally we found and

---

<sup>1</sup>[ftp://ftp.ngdc.noaa.gov/STP/SOLAR\\_DATA/SUNSPOT\\_REGIONS/USAF\\_MWL](ftp://ftp.ngdc.noaa.gov/STP/SOLAR_DATA/SUNSPOT_REGIONS/USAF_MWL)

<sup>2</sup><http://solarscience.msfc.nasa.gov/greenwch.shtml>



selected 31 candidates which can be studied from their initial emergence on the visible solar disk with reference to the Solar-Monitor website <sup>3</sup>.

### 3.2.2 Imaging Data

To follow the evolutions of ARs, we used the longitudinal magnetograms and the continuum images taken with SOHO/MDI with a cadence of 96 min and a pixel size of  $2.0''$ . We utilized the *Geostationary Operational Environmental Satellite* (GOES) X-ray data to estimate the total flare activity of selected ARs. When we need to check the coronal structures, we used Full-disk Fe XII  $195\text{\AA}$  images of the *Extreme ultraviolet Imaging Telescope* (EIT; Delaboudinière *et al.*, 1995) on board SOHO taken with a cadence of 12 min and a pixel size of  $2.6''$  were used to check coronal structures. The *Transition Region and Coronal Explorer* (TRACE; Handy *et al.*, 1999) images in  $195\text{\AA}$ ,  $1600\text{\AA}$ , and  $5000\text{\AA}$  taken with approximately 1 min cadence and  $0.5''$  per pixel were also used if available.

### 3.2.3 Image Analysis

#### 3.2.3.1 Alignment of AR Images

A time-series of MDI images of a target AR was aligned by the method proposed by Chae (2001) and Chae *et al.* (2001). We converted original 2 arcsec resolution images into 1 arcsec ones, and then applied a non-linear mapping to remove the differential rotation effect. With these aligned images, we studied the evolution of the target AR, and measured the duration of the  $\delta$ -state by comparing the magnetograms with the continuum images. In this study, we set the brightness levels of 0.9 for penumbrae and 0.65 for umbrae relative to the intensity of the quiet region (see Figure 3.1).

#### 3.2.3.2 Circulation

When we closely looked at the evolution of an AR, some sunspots exhibited prominent rotation around their centers. We estimated the magnitude of rotation by measuring the spatially integrated vorticity around the rotating sunspot in the following manner. First, we re-aligned the sunspot location in each sequential magnetogram to the center of gravity of the magnetic field strength to remove the effect of proper motion of the sunspot. Second, we applied the local correlation tracking method (LCT; November and Simon, 1988) to these images to derive the horizontal velocity field ( $\mathbf{v}$ ) around the sunspot. Then, we calculate the area integral of the vorticity, namely circulation ( $C$ ), by

$$C = \int (\nabla \times \mathbf{v})_z dS, \quad (\nabla \times \mathbf{v})_z = \frac{\partial v_y}{\partial x} - \frac{\partial v_x}{\partial y}. \quad (3.1)$$

<sup>3</sup><http://www.solarmonitor.org/>

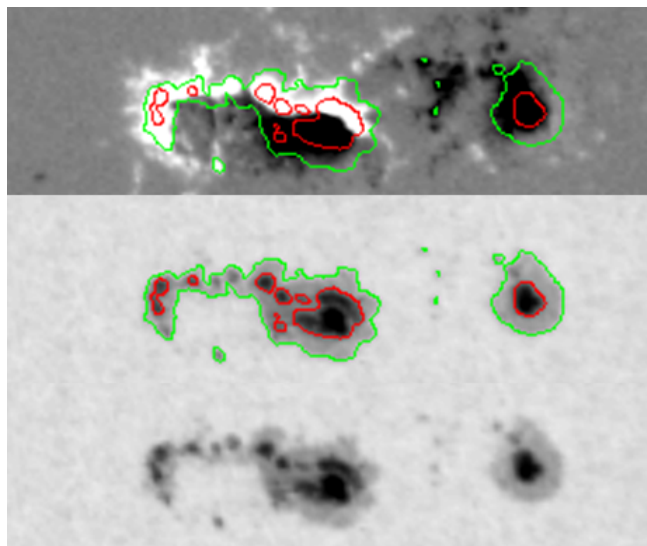


Figure 3.1: A magnetogram (top, gray scale) and a white light image (bottom) of NOAA 10314. Green and red contours show the intensity levels of 0.9 and 0.65 of the quiet region (QR) intensity and delineate QR-penumbra boundaries and penumbra-umbra boundaries, respectively (the middle panel). The AR has  $\delta$ -configuration in the central part.

We trimmed away the edge zone of three-pixel width from the vorticity field to remove fluctuating and erroneous values before the final estimation of the circulation. The procedure of trimming is done by first making a binary image from the original vorticity map, and then applying the erosion function ERODE in the IDL (Interactive Data Language) software to the binary image which results in the shrinkage of island areas in the binary image by three pixels, and finally masking the original vorticity map with the eroded binary image. An example of our method for the vorticity field at 17:35UT on 16 January 2005 is shown in Figure 3.2. From left to right, the velocity field overlaid on the magnetogram, the vorticity field, and trimmed-away map of the vorticity field are shown. Erroneous vorticity values originate at the border between the real velocity field and the quiet region where the velocity of magnetic features is zero. The erosion operation can eliminate the contaminations from the real rotational elements around the target sunspot effectively as shown in Figure 3.2.

According to the mathematical definition of circulation, positive (negative) circulation corresponds to counter-clockwise (clockwise) rotation. Note that the signs are opposite to those of the magnetic twist described in Section 3.2.3.4.

### 3.2.3.3 Tilt Angle of $\delta$ -Spots

The temporal variation of the tilt angle (*i.e.* the inclination angle of the line connecting the bipoles) tells us the orientation of the kink in an emerging magnetic tube. Figure 3.3 schematically shows the case of a tube with left-handed writhe; upward-kinked (left

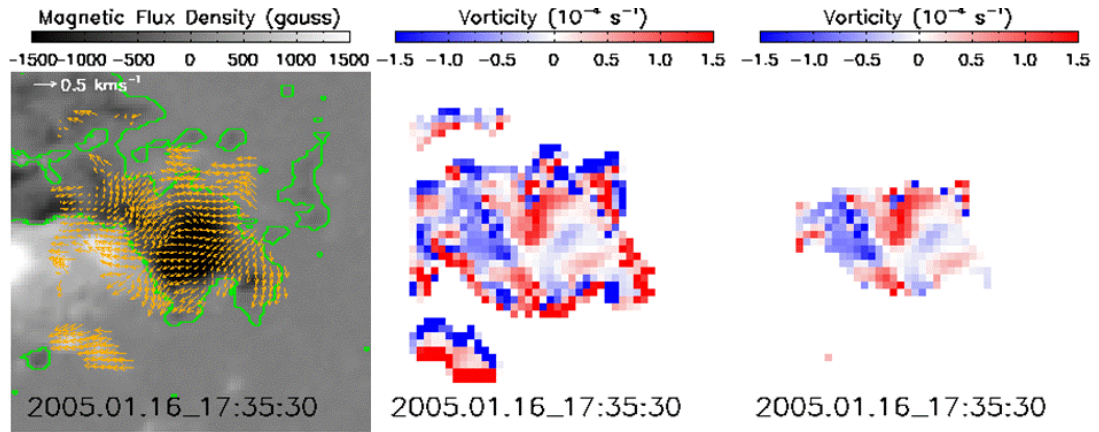


Figure 3.2: Erosion operation applied to the vorticity field at 17:35UT on 16 January 2005. From left to right are shown a magnetogram, a vorticity field, and the edge-trimmed map of the vorticity field, respectively. The velocity field (yellow arrows) and neutral lines (green contours) are overlaid on the magnetogram (gray scale).

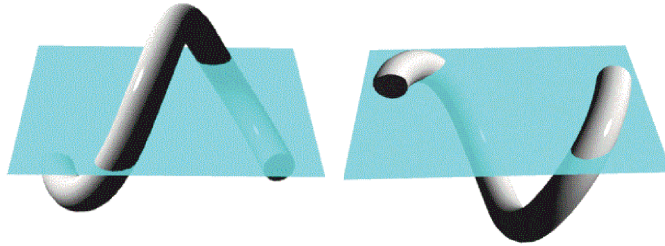


Figure 3.3: Illustrations of the emergence of tubes with left-handed writhe in the cases of upward-kinked and downward-kinked configurations. In both cases, the inclination angle of the line connecting the two footpoints rotates clockwise and their separation increases or decreases according to the orientation of the kink.

panel) and downward-kinked (right panel).

When they emerge through the photosphere, the tilt angle rotates in the clockwise (CW) direction in both cases. The distance between the footpoints increases for the upward-kinked case, while it decreases for the downward-kinked case. When the tubes with right-handed writhe emerge, the rotation is in the counter-clockwise (CCW) direction and the distance between the footpoints changes according to the kink direction as in the left-handed case. Thus we can infer the orientation of the kink in the emerging magnetic tubes from the temporal variations of the inclination angle and the distance between the two spots.

### 3.2.3.4 Sign of Magnetic Helicity

A “magnetic tongue” pattern is proposed as a useful parameter to give the sign of magnetic helicity of the emerging field (López Fuentes *et al.*, 2000; López Fuentes *et al.*, 2008; Luoni *et al.*, 2011). When a twisted tube emerges above the photosphere, the spatial distribution of photospheric magnetic field has an elongated shape like a tongue. The tongues of different polarities show anti-parallel orientations along the neutral line. Since the orientation of a tongue pattern depends on the sense of twist of the emerged tube, we can use this parameter as a proxy of the sign of helicity (twist) of the emerging magnetic tube as shown in Figure 3.4 (see also Figure 1 of Luoni *et al.*, 2011). The circulation of a sunspot is another measure of the sign of helicity of the magnetic flux tube, and consistency can be checked by comparing of these two signs.

To avoid confusion, we here reiterate the definitions for the handedness; the sign of the left (right)-handed twist or writhe is negative (positive).

### 3.2.3.5 Flare Index

Several authors have used the soft X-ray flare index (FI) as a proxy of the activity level of ARs, as given by (*e.g.* Antalová, 1996; Joshi and Joshi, 2004; Abramenko, 2005; Jing *et al.*, 2006)

$$\text{FI} = 1.0 \times \sum_i m_C + 10.0 \times \sum_j m_M + 100.0 \times \sum_k m_X, \quad (3.2)$$

where  $m_C$ ,  $m_M$ , and  $m_X$  are the GOES soft X-ray peak intensity magnitudes (from 1.0 to 9.9) of C, M and X-class flares. The indices  $i$ ,  $j$ , and  $k$  designate flares in each class per unit time period. For an AR, two kinds of periods were considered in this article; those in which the AR was visible on the disk and the AR was in the  $\delta$ -state. We do not consider small flares less than the C-class in this study because they tend to be frequently hidden by major flares or are indistinguishable from the background level.

## 3.3 Results

The  $\delta$ -spots studied in this article can be classified, from the point of view of the emergence morphology, the magnetic connection, the helicity of sunspots, and the flare activity, into the following groups: i) top-to-top collision, ii) writhed loop, iii) quasi- $\beta$ , and iv) the others. The majority of  $\delta$ -spots in our sample are classified into the first three groups. In the next subsection, we select and describe the features of a representative example of each group to show our classification scheme.

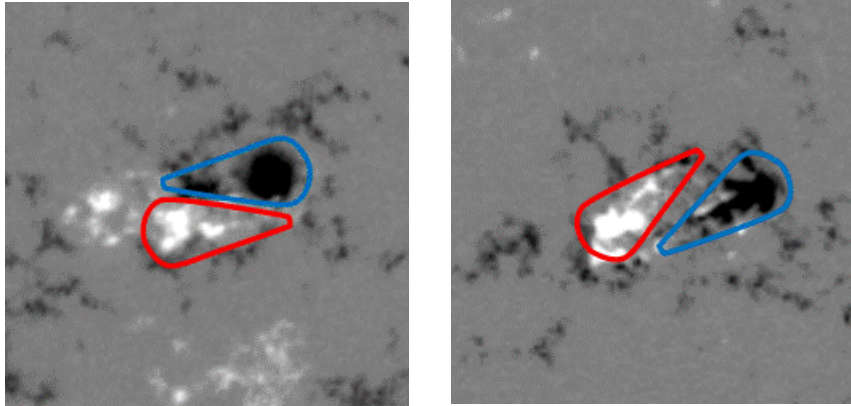


Figure 3.4: Sample images of magnetic tongues. When the head parts of the “Yin-Yang” structure forming the magnetic tongues show clockwise or counter-clockwise orientation, they indicate negative or positive magnetic helicity, respectively.

### 3.3.1 Case Studies

#### 3.3.1.1 Evolution of NOAA10720

NOAA10720 was the most flare-productive region in our samples. It had the longest  $\delta$ -duration (longer than 213 h), and showed rapid expansion since its emergence.

The magnetic and morphological evolution of the region was as follows. First, an emerging flux region (EFR1) emerged as a simple  $\beta$  magnetic configuration with almost east-west orientation obeying Hale’s law. Then it expanded rapidly in size and evolved to the  $\delta$ -configuration on 12 January 2005 as shown in Figure 3.5. Another new highly sheared EFR (EFR2), which disobeyed Hale’s law, appeared on the neutral line as if it tried to penetrate into the opposite polarity portion of EFR1 at around 16:00UT on 13 January 2005.

In Figure 3.5, we cannot see any signature of writhe in EFR1, as its tilt showed no systematic rotational movements. The magnetic tongues of EFR1 in the initial emerging phase indicated negative magnetic helicity as shown in the first row of Figure 3.5. This means that the tube emerged with a left-handed twist. Unfortunately, the tongue pattern could not clearly be seen after the vigorous and complex development of EFR1.

On the other hand, the tilt angle of EFR2 showed a slow CW rotation, suggesting the emergence of a loop with left-handed writhe. The twist of the magnetic tubes can be estimated by the circulation around the footpoints of the magnetic tubes, *i.e.* sunspots.

Now let us see the distribution of vorticity around sunspots of p2 and n2 shown in Figure 3.6. By specifying the integration area with a circle or an ellipse, which covers the target sunspot as compactly as possible, we estimated the circulation over the area covering each sunspot. The reliability of the circulation value was estimated by changing the size of the calculation area. The area was enlarged or reduced by 2 arcsec

for this purpose. Besides the procedures described in Section 3.2.3.2, we masked the opposite polarity areas before the integration to avoid contamination. The temporal evolution of the circulation of each sunspot is displayed in Figure 3.7. Both sunspots showed generally positive circulation although they showed negative values at times. When we closely looked at the vorticity map and the motions of small sunspots in the neighborhood of the n2 spot for a day on 16 January, we found that the rapid sliding motions of small sunspots relative to the static environment were recorded as false negative circulation. If we take this contamination into account, we can assume that the circulations around the p2 and n2 spots were mostly positive during the evolution, which means that the footpoints of the magnetic tube of EFR2 showed a CCW rotation during their evolution. Therefore, EFR2 can be considered as an emerging loop of a left-handed twist.

The timing of the flaring in the region is shown in Figure 3.8. After the emergence of EFR2 on 13 January, many flares have occurred, including three X-class flares. High activity triggered by the emergence of EFR2 reminds us of the top-to-top collision model proposed by Ikhsanov *et al.* (2004). The flare morphology gave us additional information on the magnetic helicity of EFR2. The SOHO/EIT 195 Å image in the left panel of Figure 3.9 shows an inverse-S shaped structure over EFR2 after the X1.2 flare that peaked at 0:43UT. The inverse-S sigmoid morphology indicates the left-handed twist of the magnetic tube. The TRACE 1600 Å image in the right panel of Figure 3.9 shows bright loops connecting the two polarities of EFR2. Guo *et al.* (2013) argued that negative helicity was accumulated in EFR2 by a model of non-linear force-free fields, suggesting the emergence of a tube with a left-handed twist.

Thus, we conclude that the significant flare activity of NOAA 10720 is due to the emergence and the intrusion of the twisted and writhed EFR2 into the magnetic neutral line of the pre-emerged EFR1. This region is a typical example of the top-to-top collision formation of an active  $\delta$ -type spot.

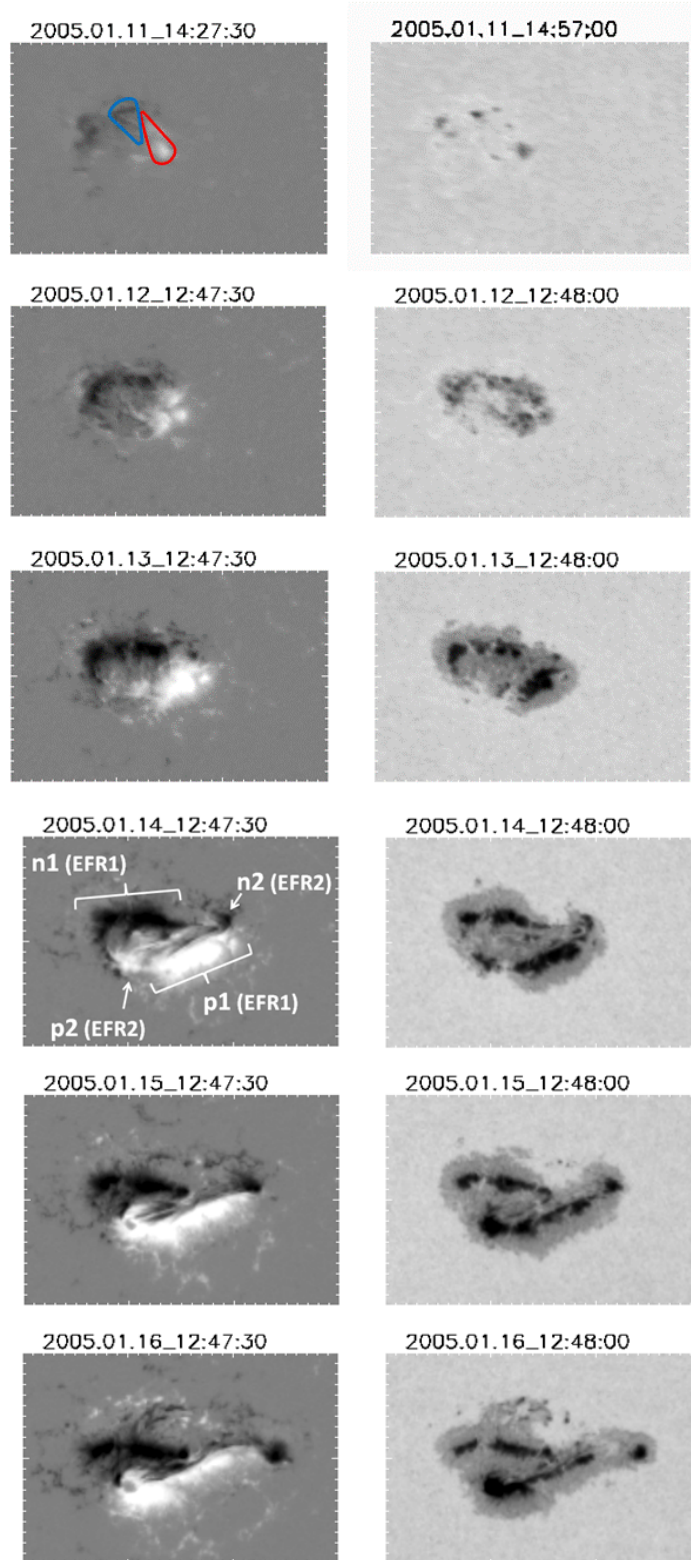


Figure 3.5: SOHO/MDI magnetograms (left) and white-light images (right) of NOAA 10720 corresponding to subsequent days of observations. Identified two EFRs are shown in the fourth row. The field of view (FOV) of each panel is  $300 \times 200$  arcsec.

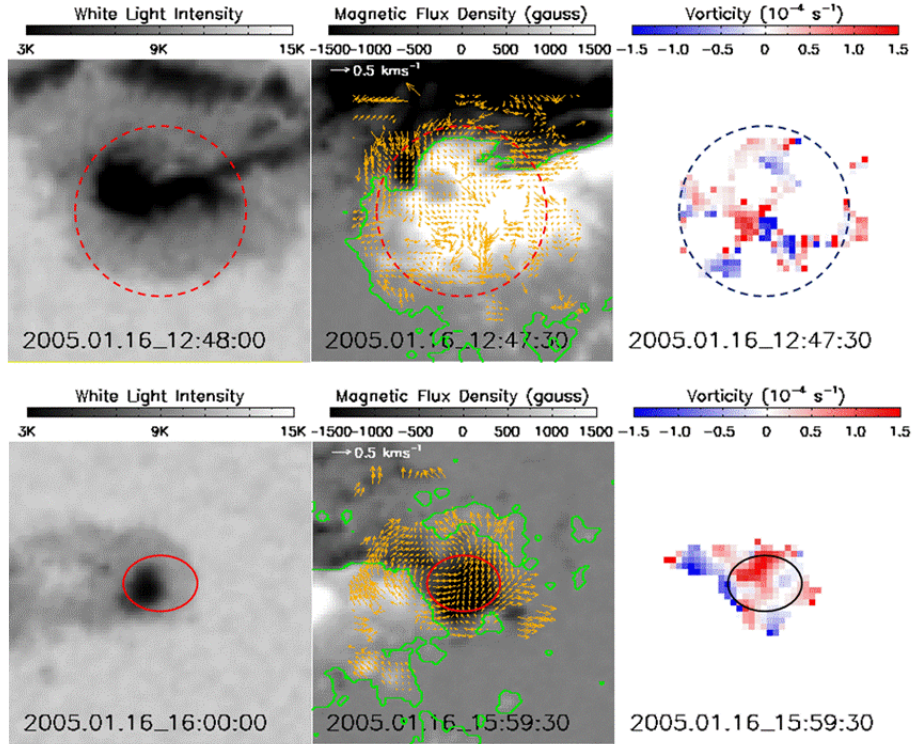


Figure 3.6: White light images (left), magnetograms (middle), and vorticity fields (right) of the positive (top row) and negative (bottom row) polarity areas of EFR2, respectively. The size of each FOV is  $100 \times 100$  arcsec, and its center is at the center of gravity of magnetic flux distribution. In the middle panels are overlaid the velocity fields (yellow arrows) and the neutral lines (green contours). The areas used to compute the circulation are shown by a circle of 28 arcsec radius in the top row and by an ellipse in the top row whose major and minor axes are 24 and 18 arcsec, respectively.



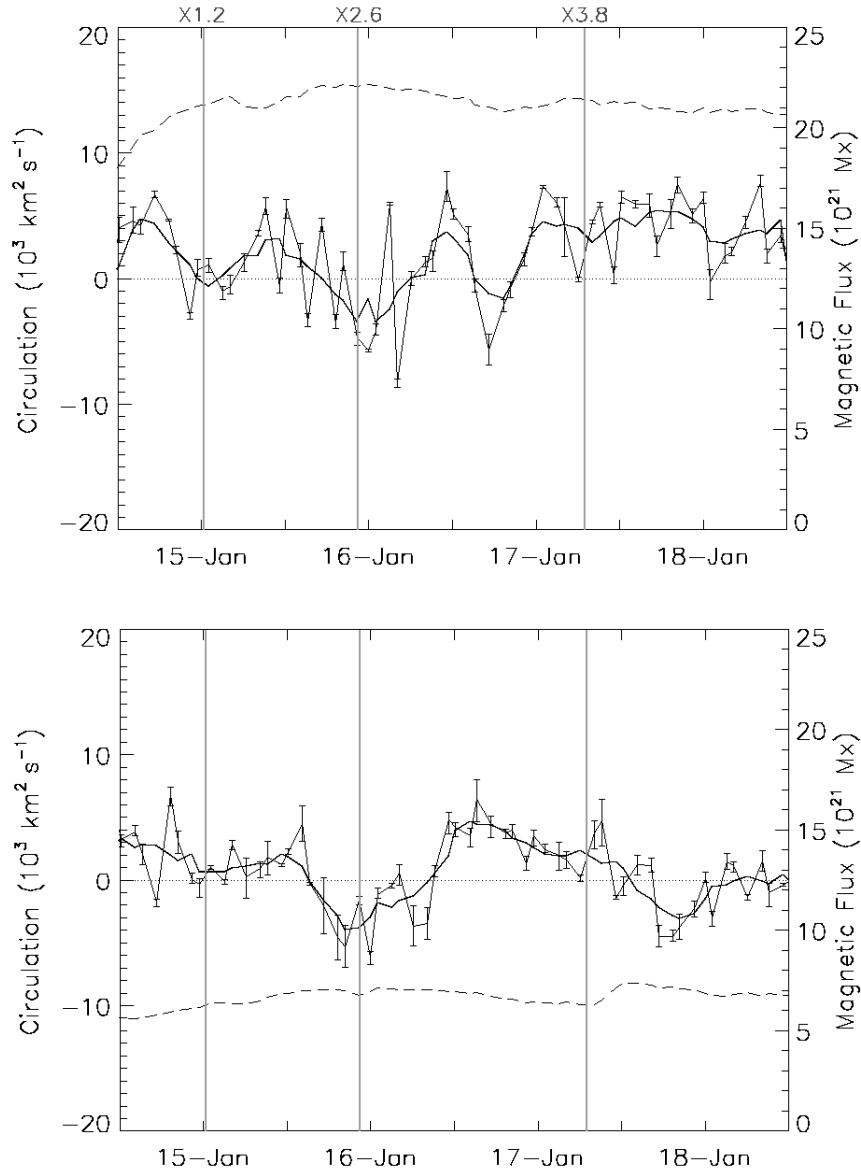


Figure 3.7: Time variations of circulation (thin solid lines) and magnetic flux (dashed lines) in sunspots p2 (top) and n2 (bottom) in NOAA 10720. The thick solid line shows the running average of circulation over five consecutive data points in each panel. The error bars indicate a possible range of the circulation values when the size of the analysis area is changes (see text). Vertical lines represent the times of the X-class flares. The magnetic flux values are evaluated for the full FOV of Figure 3.6.

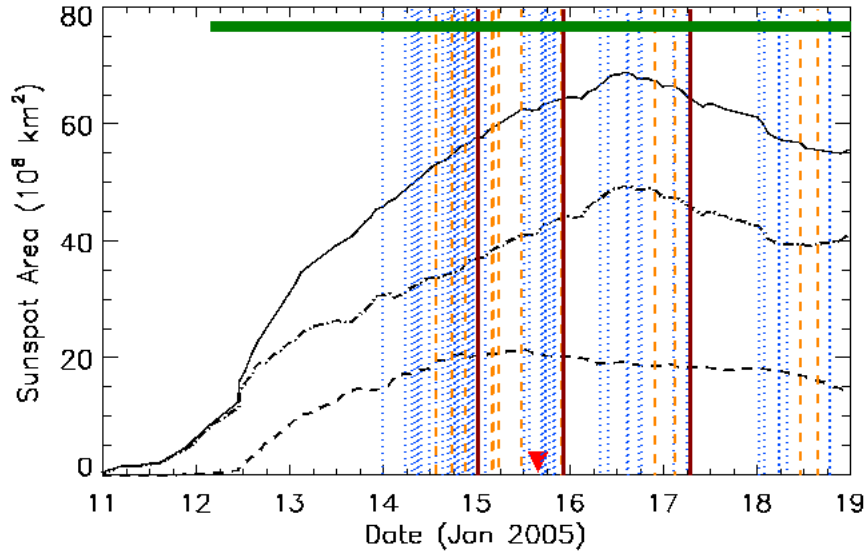


Figure 3.8: Time evolution of umbra (dashed), penumbra (dash-dotted), and total sunspot (solid) areas in NOAA 10720. Vertical lines indicate X-class (brown solid), M-class (orange dashed), and C-class (blue dotted) flares, respectively. The horizontal thick green line at the top represents the duration of the  $\delta$ -state. The triangle at the bottom indicates the central meridian passage of the region.

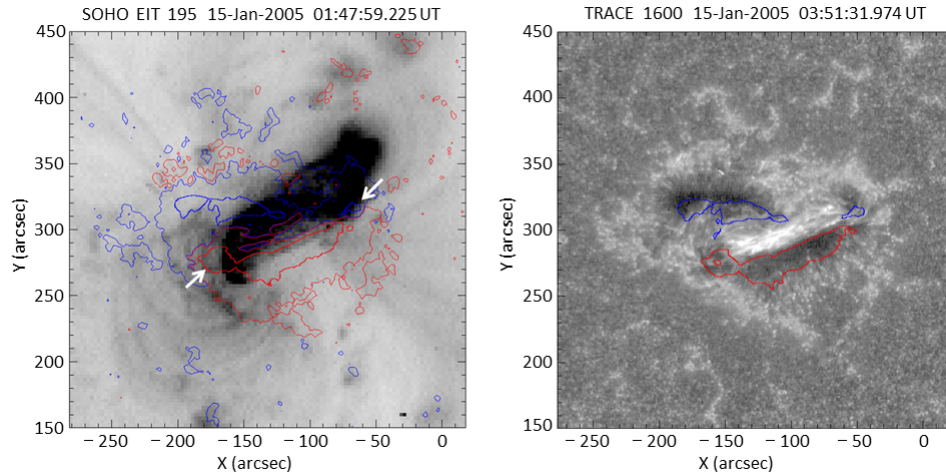


Figure 3.9: Left: A SOHO/EIT 195Å image (in negative print) of NOAA 10720 taken at 01:47 UT, 15 January 2005, after the X1.2 flare peaked at 01:02 UT. White arrows indicate two polarities of EFR2. An inverse-S shaped structure is clearly seen. Right: A TRACE 1600Å image taken at 03:51 UT on 15 January 2005 between the two X-class flares. A bright structure existed between the two polarities of EFR2 even in a relatively quiet period of flare activity. Overlaid contours (red for positive and blue for negative polarities) show the line-of-sight magnetic fields of 1500 gauss (G) and 100 G (only in the left panel). The FOV of both images is  $300 \times 300$  arcsec.

### 3.3.1.2 Evolution of NOAA10826

A day after the emergence of 29 November 2005, NOAA10826 formed a  $\delta$ -configuration and showed high flare activity in the  $\delta$ -duration of 56 h.

Its magnetic and morphological evolution is shown in Figure 3.10. Two EFRs emerged in succession along the east-west line. The  $\delta$ -configuration was formed between the following sunspot of EFR1 and the preceding sunspot of EFR2.

The magnetic tongue patterns of EFR1 and EFR2 showed the sign of negative helicity (the top row of Figure 3.10), suggesting the emergence of magnetic tubes with a left-handed twist. The tilt of the  $\delta$ -configuration rotated in the CW direction, with an average rotational speed of  $35^\circ \text{ day}^{-1}$ , which is similar to the speed of  $30^\circ \text{ day}^{-1}$  measured in NOAA10314 by Poisson *et al.* (2013). As the separation between the umbrae of the  $\delta$ -spot decreased in the first stage, this  $\delta$ -configuration behaved as the emergence of a tube with left-handed writhe and downward kink. As the twist had the same sign as the writhe, we suggest that the tube was kinked downward due to transformation into the writhe from the twist in the layers below the photosphere.

The magnetic twist of EFR1 and EFR2 was studied by the circulation at the foot-points of EFRs. We have selected sunspots n1 of EFR1 and p2 of EFR2 for the evaluation of circulation, as they were isolated and free from possible contamination. From the temporal variations of the circulation shown in Figure 3.11, we conclude that the circulations in both sunspots were predominantly positive, which means that the sunspots in the two EFRs rotated in the CCW direction, *i.e.* the tubes emerged with a left-handed twist.

High flare activity in this region started just after the formation of the  $\delta$ -configuration, producing 17 flares in total (4 M-class and 13 C-class) during its disk passage and 11 flares (3 M-class and 8 C-class) during the  $\delta$ -configuration (Figure 3.12). The flare morphology gave some insight on the topology near the neutral line of the  $\delta$ -configuration. Figure 3.13 shows the case of an M1.0 flare. We can see that the bright flare strand had a highly sheared structure with a left-handed twist. Since the bright strand was probably produced by the magnetic reconnection in the corona, we can infer that the magnetic field near the neutral line had left-handed helicity before the flare explosion.

All the direct or indirect evidence indicates that the EFRs in this region had the same left-handed helicity. As the magnetic fluxes of sunspots n1 and p2 were of the same order of magnitude (Figure 3.11), it is natural to assume that the two EFRs were not physically separated but connected like a single writhed structure as in the case of NOAA 10314 reported by Poisson (2013). Therefore we classify this region as the “downward knotted” type.

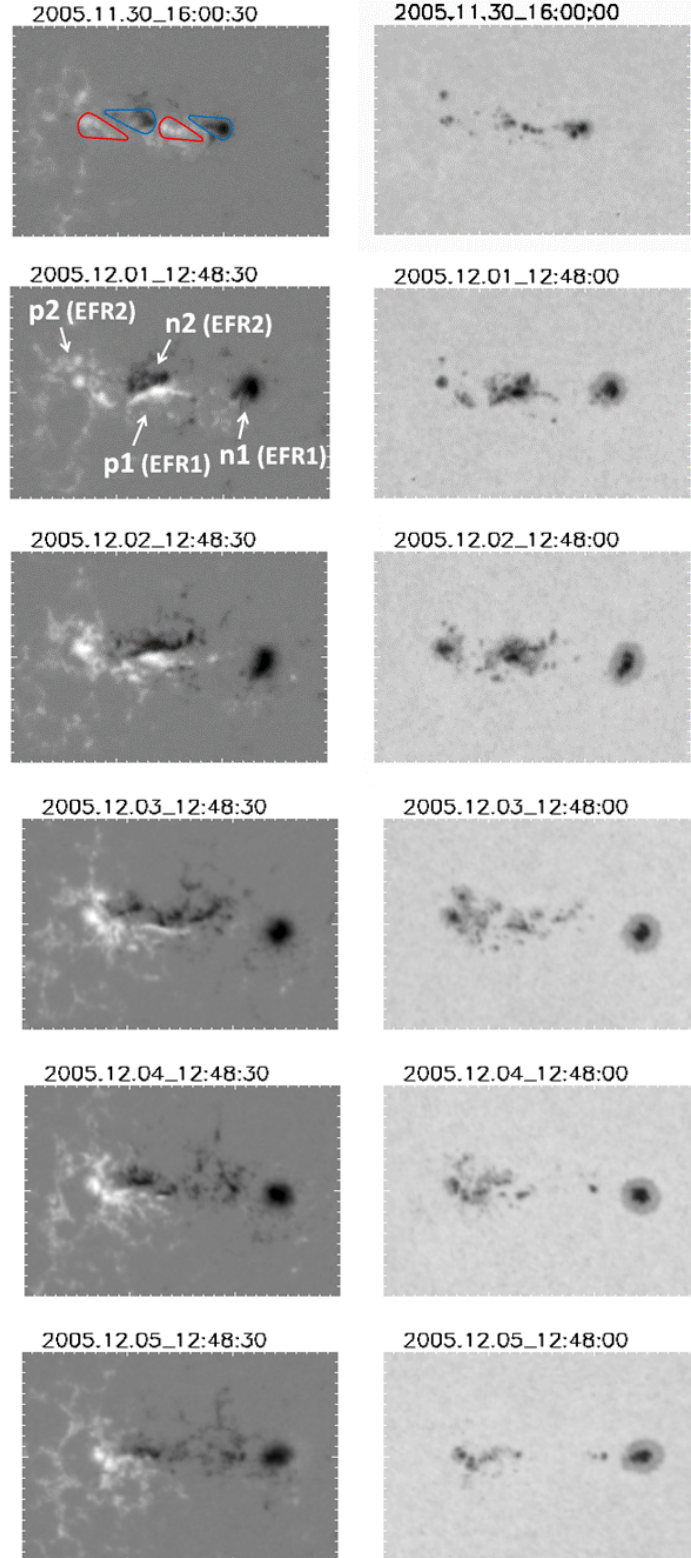


Figure 3.10: SOHO/MDI magnetograms (left) and white-light images (right) of NOAA 10826. Identified two EFRs are shown in the second row. The FOV of each panel is  $300 \times 200$  arcsec.

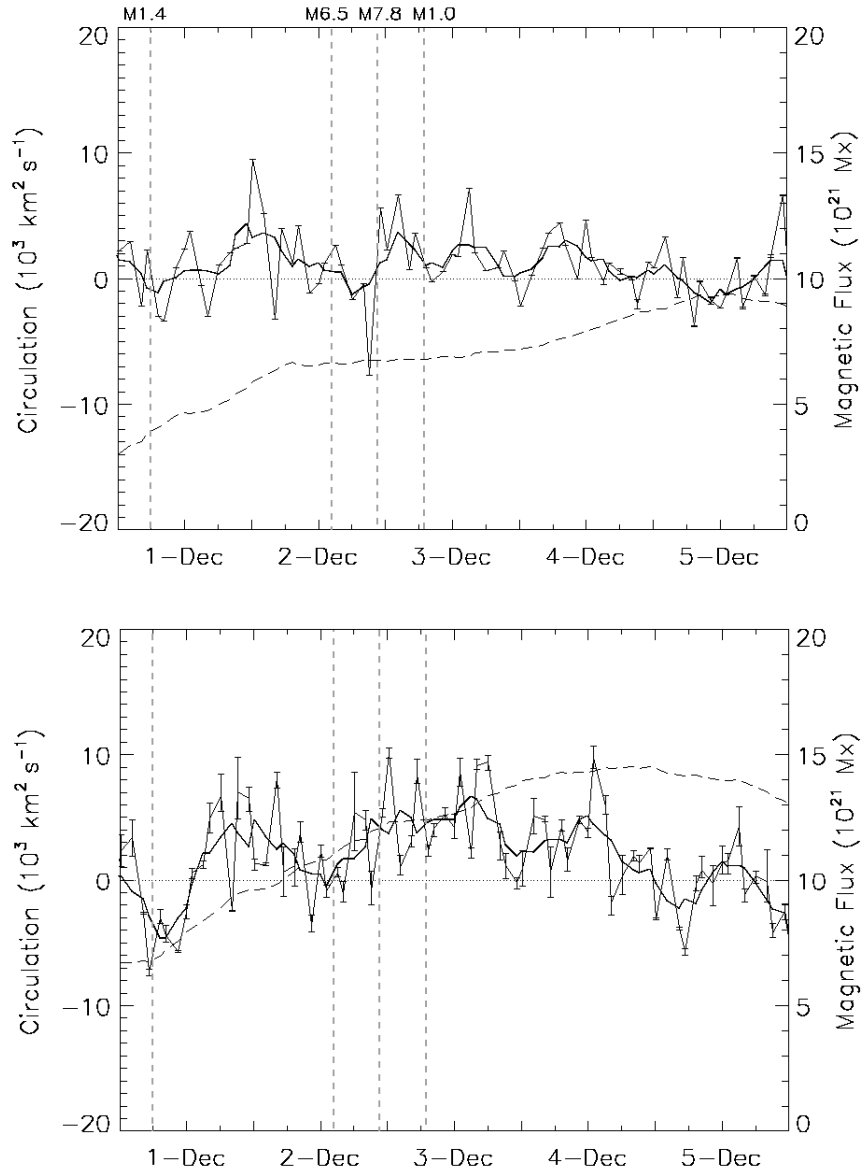


Figure 3.11: Time variations of circulation (thin solid lines) and magnetic flux (dashed lines) in sunspots n1 (top) and p2 (bottom) in NOAA 10826. The format is the same as in Figure 3.7.

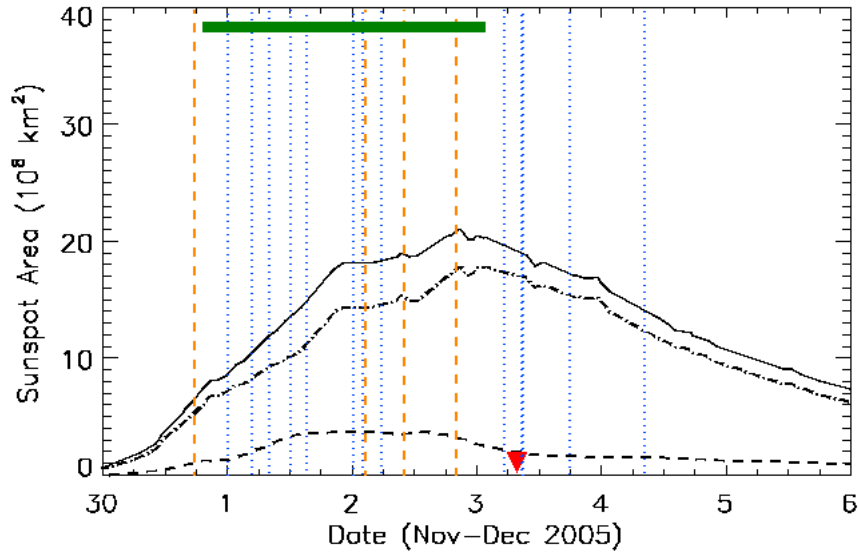


Figure 3.12: Time evolution of umbra (dashed), penumbra (dash-dotted), and total sunspot (solid) areas in NOAA 10826. The format is the same as in Figure 3.8.

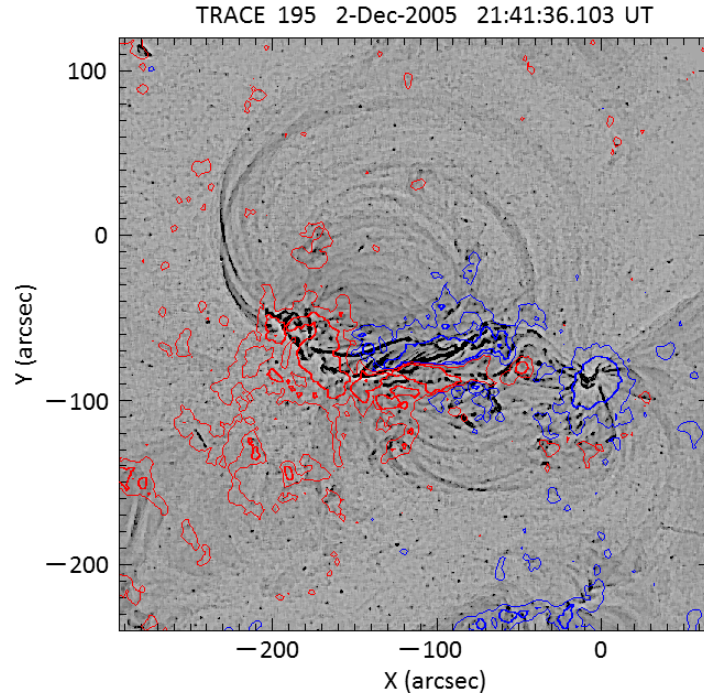


Figure 3.13: A high-pass filtered TRACE 195 Å image (in negative print) of NOAA 10826. Contours indicate line-of-sight magnetic fields of 500 G (thick) and 100 G (thin) in positive (red) and negative (blue) polarity areas. After the M1.0 flare, highly-sheared bright structures appeared on the  $\delta$ -part of the region.

### 3.3.1.3 Evolution of AR NOAA10050

NOAA10050 emerged on 26 July 2002. Although the region developed due to successive emergence of several EFRs, the flare activity was not high. A few  $\delta$ -configurations formed and disappeared within their lifetime of less than a day at different locations in the region. See Figure 3.14 for the magnetic and morphological evolution of the region.

The EFRs in the region emerged with their axes in the east-west direction. As they evolved, the two opposite polarities of each EFR were separated with each other and sunspots of each polarity merged into a dominant center. The evolution was very similar to the bipolar emergence model of Zwaan (1978). The  $\delta$ -configuration formed transiently when a pair of small opposite polarity elements incidentally came together. We found no signature of writhe pattern in their motion.

The temporal evolutions of circulation around the dominant polarities are shown in Figure 3.15. The preceding negative polarity changed its circulation from negative to positive significantly in the early phase of the evolution. After several changes in its sign, the positive circulation became dominant in the later phase. On the other hand, the following positive polarity always indicated negative circulation during the period. The circulations of the two polarities had a tendency to show opposite directions. Furthermore, the evolution of circulation was influenced strongly by the successive merging of small sunspots. Therefore, we may conclude that the actual twist of the dominant sunspots was not high. The flare activity in the  $\delta$ -state of this region was very modest as shown in Figure 3.16.

The evolution of the region is very similar to the  $\beta$ -type and we classify the region as the “quasi- $\beta$ ” type.

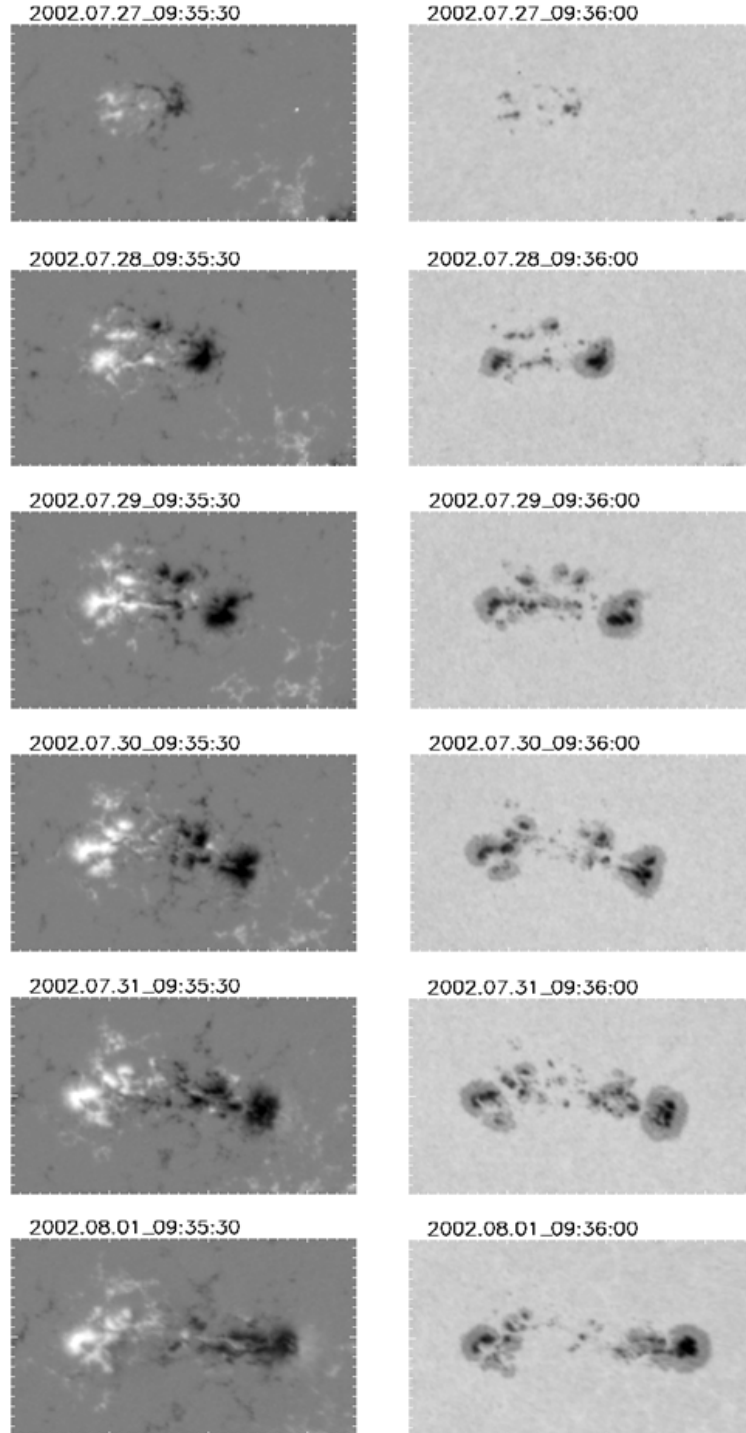


Figure 3.14: SOHO/MDI magnetograms (left) and white-light images (right) of NOAA 10050. The FOV of each panel is  $350 \times 200$  arcsec.



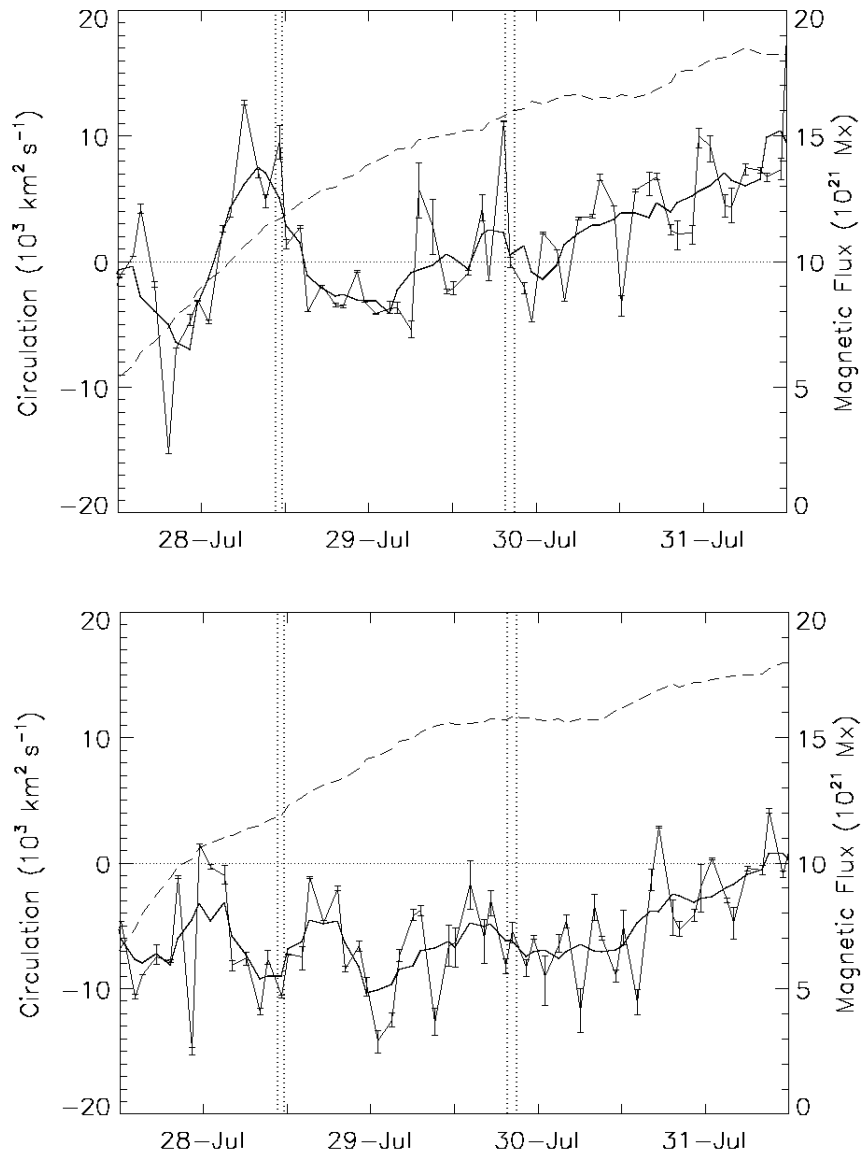


Figure 3.15: Time variations of circulation (thin solid lines) and magnetic flux (dashed lines) in the preceding negative polarity sunspot (top) and the following positive polarity sunspot (bottom) in NOAA 10050. The format is the same as in Figure 3.11. Dotted vertical lines represent C-class flares.

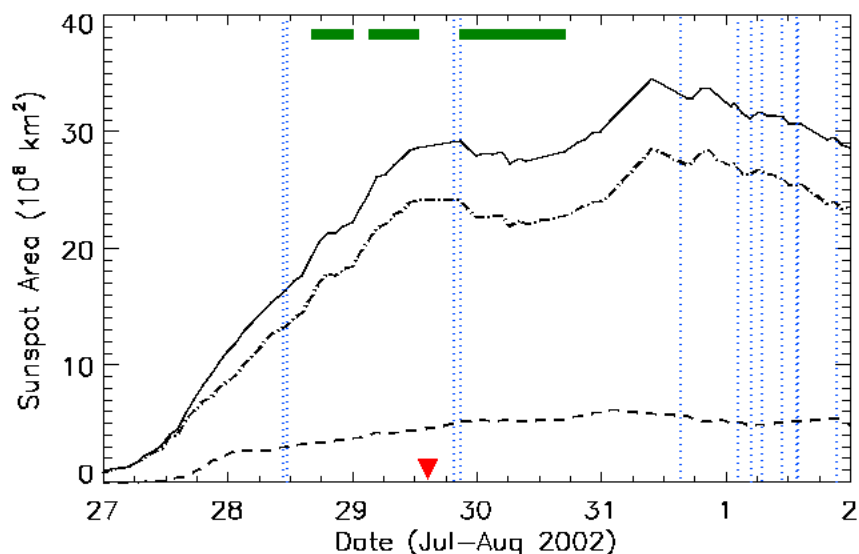


Figure 3.16: Time evolution of umbra (dashed), penumbra (dash-dotted), and total sunspot (solid) areas in NOAA 10050. The format is the same as in Figure 3.8.

### 3.3.2 Statistical Study

In our case studies of  $\delta$ -spots, we notice high flare activity in magnetically complex  $\delta$ -spots. In this subsection, we will statistically analyze the dependence of the flare activity on the characteristic parameters of  $\delta$ -spot regions.

#### 3.3.2.1 Parameters

In Table 1, we summarize several flare indices and the parameters which characterize the 31 ARs we studied. The peak soft X-ray flux ( $X_{R_{\max}}$ ) and FI are the flare indices, while the maximum sunspot area ( $S_{\max}$ ), the maximum umbral area ( $S_{U_{\max}}$ ),  $\delta$ -term (the duration of the  $\delta$ -state), the handedness of twist and writhe, and the type of  $\delta$ -spot formation are the characteristic parameters of ARs. We will comment on the values of the listed parameters in the following paragraphs.

An AR develops and changes its magnetic type and sometimes passes through the west limb keeping its high activity. To eliminate possible ambiguity and uncertainty in the estimated parameters, we only considered the events that occurred in longitudes less than  $W70^\circ$ . The values of FI were thus counted and listed in Table 1. The values in parentheses are for the flares that occurred during the  $\delta$ -state of the region. The identification of the  $\delta$ -state was also limited to longitudes less than  $W70^\circ$ , so that it gives a lower limit in some cases.

The  $\delta$ -state in an AR was not always continuous in time. If there appeared multiple  $\delta$ -states intermittently in an AR, we summed all the time spans of  $\delta$ -periods to obtain the “ $\delta$ -duration” (or “ $\delta$ -term”) in this study. When there was a gap longer than several hours in the available MDI continuum images, we also used TRACE white light images

to estimate the  $\delta$ -duration. However, there remained the uncertainties ranging from seven to 31 hours, which is regarded as estimation errors for the  $\delta$ -duration.

As seen in our case studies, the magnetic field distributions in  $\beta\gamma\delta$  ARs are complex and the estimation of the magnetic twist from the circulation is sometimes ambiguous. However, it is well known that the preceding sunspots have more rigid structure and longer lifetime than the following sunspots (van Driel-Gesztelyi and Petrovay, 1990), while the following sunspots tend to be affected by turbulent motions in the surroundings which cause the fragmentation of the flux tube (Fan *et al.*, 1993). Therefore we mainly measured the circulation of the preceding sunspots and adopted their handedness of twist as more reliable representatives of the ARs. To decide the sign of writhe, we considered the evolution of the  $\delta$ -part as described in Section 3.2.3.3.

The flare that corresponded to the peak X-ray flux represents only a single event of an AR through the observational period and the event did not always occur in the  $\delta$ -state. On the other hand, FI can be measured over the definite period of the  $\delta$ -duration. Therefore, we regarded FI as a better parameter of flare activity in the  $\delta$ -state than  $\text{XR}_{\text{max}}$ .

Table 3.1: Summary of parameters for 31ARs studied. The upper part of the table is for ARs in the northern hemisphere, while the lower part is for those in the southern hemisphere. Here,  $\text{XR}_{\text{max}}$  means the peak X-ray flux in the observed period of each AR. Flare Index indicates the value integrated over the observed period (the value integrated over the  $\delta$ -state is shown in parentheses).  $S_{\text{max}}$  means the maximum sunspot area in the observed period.  $S_{\text{Umax}}$  means the maximum umbral area in the observed period (the value in the  $\delta$ -state is shown in parentheses).  $\delta$ -term shows the integrated duration of the  $\delta$ -state. The twist and writhe are indicated by R (right-handed) or L (left-handed). The “Type” column show the emergence type of ARs; TT (top-to-top), DK (downward knotted), UK (upward knotted), and QB (quasi- $\beta$ ), respectively.

AR	$\text{XR}_{\text{max}}$ ( $\text{Wm}^{-2}$ )	Flare Index	$S_{\text{max}}$ ( $\text{Mm}^2$ )	$S_{\text{Umax}}$ ( $\text{Mm}^2$ )	$\delta$ - term (h)	Twist	Writhe	Type
9165	59.0	257.0 (42.2)	1851	291 (280)	24	L	L	UK
9511	120.0	275.9 (247.5)	714	114 (114)	20	R	R	DK
9678	20.0	103.1 (40.3)	3046	623 (584)	26	L to R	L	DK
9901	40.0	53.1 (53.1)	2003	283 (283)	188	—	R	—
10412	9.8	22.8 (6.0)	944	170 (160)	27	R	R	DK
10488	19.0	191.8 (191.8)	6786	1789 (1789)	158	L	L	DK
10564	110.0	219.0 (209.0)	3716	659 (659)	110	—	—	TT
10696	250.0	1114.9 (1062.1)	3841	829 (829)	192	L	L	TT
10720	710.0	2299.3 (2299.3)	6906	2147 (2147)	213	L	L	TT
10956	2.9	3.9 (2.9)	1054	151 (151)	112	—	—	—
8506	3.3	9.1 (0.0)	1285	245 (211)	8	R	—	QB
8926	2.3	96.6 (41.6)	805	152 (152)	52	L	L	DK
9494	10.0	59.9 (26.7)	1105	251 (159)	32	R	R	DK
9775	22.0	115.3 (11.0)	1415	144 (144)	32	L	L	DK
9900	4.4	11.2 (0.0)	633	75 (67)	10	—	—	—
9904	9.2	8.2 (0.0)	247	52 (52)	30	—	L	—
9906	26.0	58.1 (48.5)	2907	540 (540)	114	R	R	DK
10017	150.0	282.5 (174.4)	2298	341 (341)	34	R	R	TT
10050	8.6	57.5 (6.5)	3408	627 (600)	38	—	—	QB
10119	8.8	54.9 (14.0)	3192	541 (541)	92	L	—	QB
10137	40.0	174.7 (170.0)	1330	252 (252)	88	L	L	DK
10226	68.0	231.6 (124.0)	2812	578 (578)	110	L	R	DK
10314	150.0	511.1 (443.9)	2367	635 (635)	94	R to L	R	DK
10417	5.2	39.7 (6.9)	1405	199 (158)	15	—	—	QB
10456	4.4	6.6 (2.2)	772	101 (60)	14	—	—	QB
10551	3.2	6.9 (0.0)	1531	221 (221)	38	—	—	QB
10591	12.0	12.0 (12.0)	412	82 (82)	32	R	—	—
10798	56.0	84.8 (84.3)	2931	461 (461)	65	R	—	TT
10826	78.0	204.7 (200.9)	2152	390 (390)	56	L	L	DK
10848	41.0	14.9 (0.0)	1466	181 (181)	21	—	—	—
10865	14.0	30.0 (0.0)	2532	568 (285)	38	—	—	QB

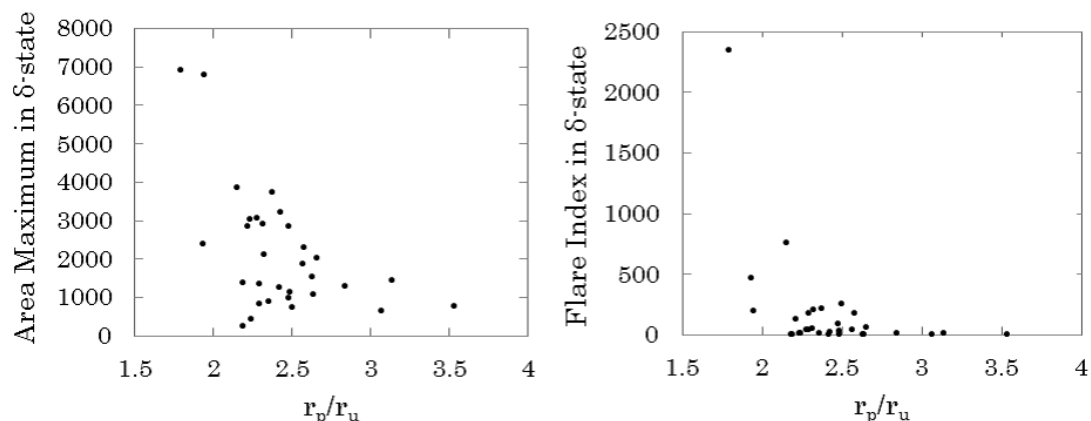


Figure 3.17:  $S_{\max}$  (left) and FI (right) *versus* the penumbral-umbral radius ratio in the  $\delta$ -state.

### 3.3.2.2 Flare Activity and Sunspot Area

Sammis *et al.* (2000) statistically studied the relation between the flare activity and the maximum sunspot area for the ARs in Cycle 22, and found that ARs with larger maximum sunspot area produced higher peak X-ray flux. Especially they showed that  $\beta\gamma\delta$ -ARs had the largest maximum sunspot area and hence produced the strongest flares. Now we will check the relation between the FI (the proxy of flare activity level) and the maximum umbral area for our sampled  $\beta\gamma\delta$ -ARs in Cycle 23.

First, we confirm that the relation found by Sammis *et al.* (2000) also holds in our data. The physical meaning of the relation is that the sunspot area is a measure of the total magnetic flux of the region and hence represents the magnetic energy content of the region. The ARs with large content of magnetic energy can produce large release of energy as flaring. As we do not have the magnetic flux values for all the ARs in Cycle 23, we have to use the measured area as a proxy parameter for the magnetic flux. The line-of-sight magnetic data by SOHO, for example, cannot provide a reliable estimate of the magnetic flux, without the correction for the projection effect and the field inclination to the vertical. We took the umbral area as a better proxy parameter of the magnetic flux than the total sunspot area including the penumbral area, because of two reasons. The first is that larger sunspots have smaller contribution of penumbra to the total sunspot area (left panel of Figure 3.17) and contain more magnetic flux in the umbral area (Antalová, 1991; Jin *et al.*, 2006). The other empirical reason is that FI does not depend so strongly on the penumbra-umbra radius ratio when this ratio is high (right panel of Figure 3.17).

Next, we notice large dispersion in FI in Figure 3.18. For a given maximum umbral area, there appears a variety of ARs from highly flare productive ones to less productive ones. In Figure 3.18,  $\beta\gamma\delta$  ARs are roughly split into different emergence types,

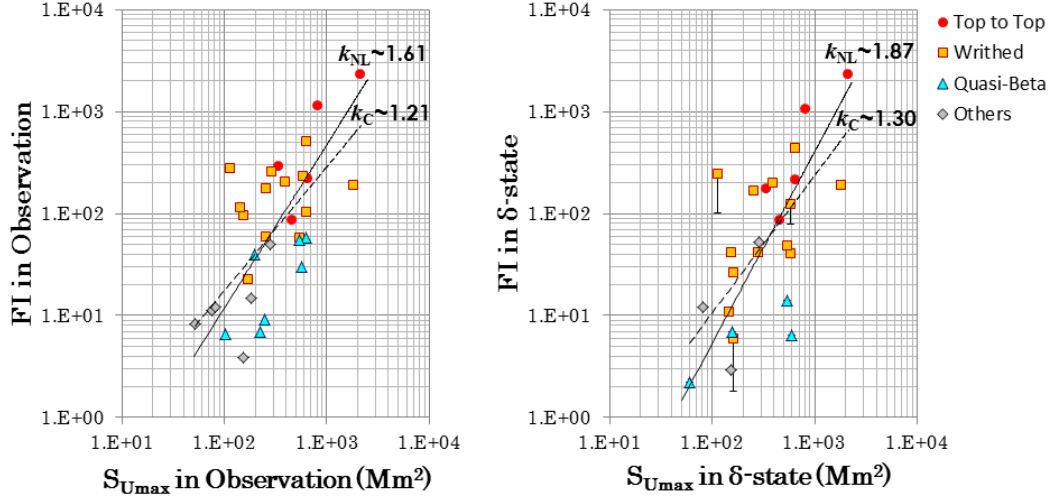


Figure 3.18: Flare index *versus* maximum umbral area in a logarithmic scale. The left panel is for the data in the observed period and the right panel is for those in the  $\delta$ -state. Six ARs which showed no flare activity in the  $\delta$ -state were excluded. Different symbols indicate “top-to-top” (red circles), “writhed” (orange squares, both DK and UK types in Table 1), “quasi- $\beta$ ” (blue triangles), and “others” (gray diamonds), respectively. The error-bars were assigned by considering the effect of data gaps (see text). The results of non-linear least-squares fitting (power-law index  $k_{NL}$ ) and classical least-squares fitting (power-law index  $k_C$ ) are shown by the solid and the dashed lines, respectively.

suggesting that the emergence mode is another key parameter to characterize the flare productivity. By comparing the two panels in the figure, we can see that the separation of the three groups in the right panel is clearer than in the left panel. Since the clear separation into groups may give hints of the  $\delta$ -state, we will mainly concentrate to the flare activity and the area variation in the  $\delta$ -state hereafter.

### 3.3.2.3 Flare Activity and Emergence Type

Figure 3.19 shows the histogram of  $S_{Umax}$  and FI distributions grouped according to the emergence type in the  $\delta$ -state. We combined the groups DK (downward-kinked) and UK (upward-kinked) in Table 1 as the “writhed” type. The bin sizes of  $S_{Umax}$  and FI are  $10^{0.4}$  ( $\approx 2.51$ ) and  $10^{0.7}$  ( $\approx 5.01$ ), respectively. The grouping follows the decreasing order of magnetic complexity (*i.e.* “top-to-top”, “writhed”, “quasi- $\beta$ ” and “others”). As the topological complexity decreases, both  $S_{Umax}$  and FI distribute to lower values. The relation found here clearly indicates that the flare activity of  $\beta\gamma\delta$  ARs depends not only on the umbral area but also on the magnetic complexity. Moreover, it suggests that the large total content of magnetic flux represented by the umbral area is a necessary condition and significant magnetic complexity may be another more stringent necessary condition for the activation of strong flares.

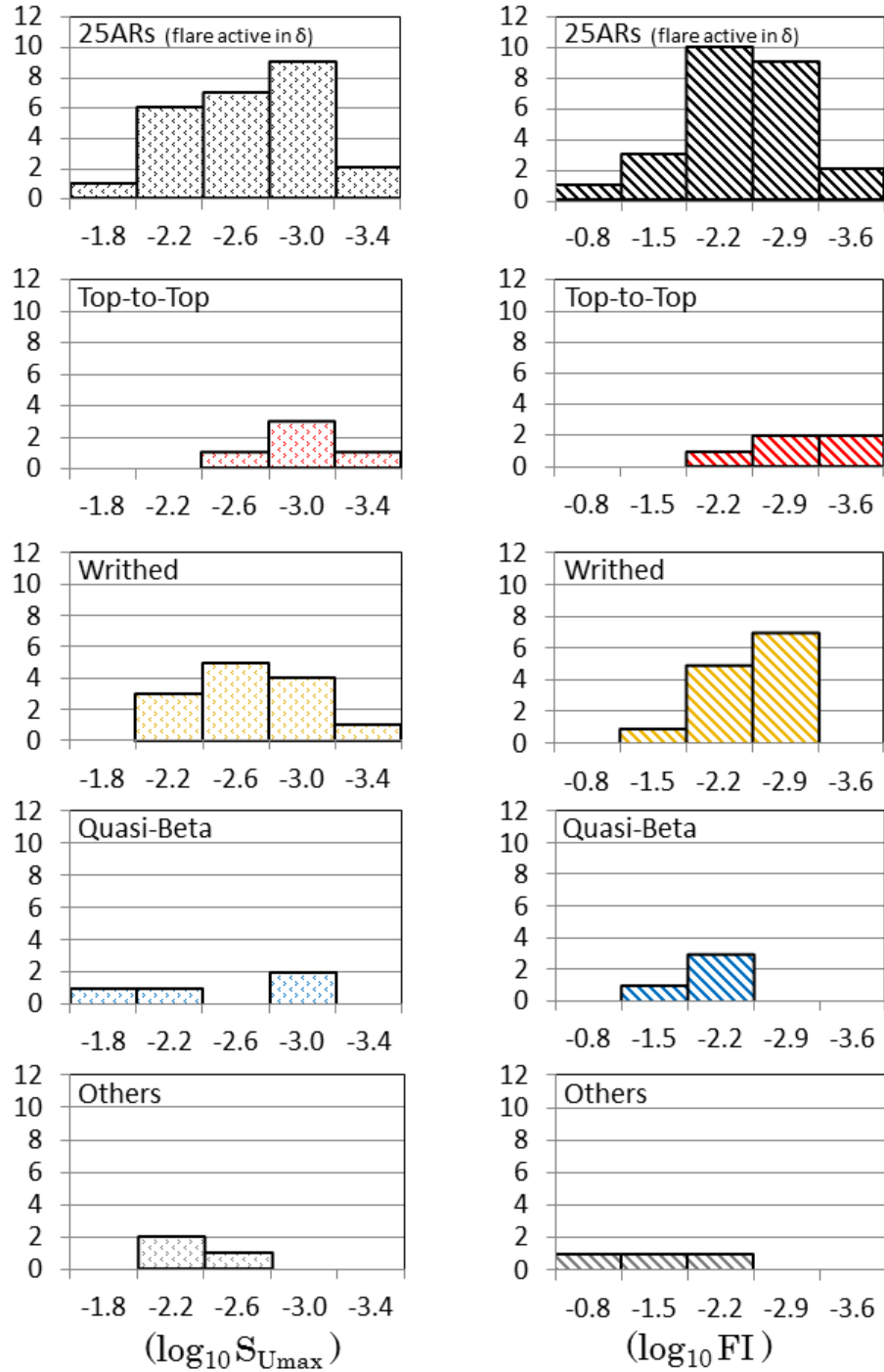


Figure 3.19: Histograms of umbral area maximum (left) and FI (right) in the  $\delta$ -state period. From the second row downward are shown “top-to-top”, “writhed”, “quasi- $\beta$ ”, and “others” types, respectively, and the top row shows the total.

### 3.3.2.4 Twist and Writhe of $\delta$ -Spots

When we classified the 31 ARs by their emergence mode, we found 5 ARs as “top-to-top”, 13 as “writhed”, 7 as “quasi- $\beta$ ” and 6 as “others”. Although the “quasi- $\beta$ ” and “others” groups hardly ever showed the signs of twist and writhe, the “top-to-top” and “writhed” ARs clearly showed the twist and writhe. In most cases of the “writhed” type, the signs of twist and writhe agree with each other at least in their initial phase (12 cases out of 13). This result strongly suggests that the formation of the  $\delta$ -spot is not due to the gathering of disjointed EFRs but due to the emergence of a singly connected structure (left panel in Figure 3.20). The “top-to-top” ARs also show high probability of agreement in their helicity signs (three cases out of five). We speculate that the “top-to-top” type has a more developed writhing structure than the “writhed” type (right panel of Figure 3.20). However, according to the study of Park *et al.* (2012), some “top-to-top” ARs may be associated with the injection of opposite-sign helicities through flux emergence. Therefore the model of “top-to-top” ARs is at present controversial and further investigation is necessary to finalize the model.

The majority of “writhed” ARs were of DK type (12 cases out of 13). The UK type was quite rare. The dominance of DK seems natural because a simple writhed magnetic tube with upward kink will emerge through the photosphere as a normal  $\beta$ -type magnetic distribution and will rarely be identified as the  $\delta$ -type sunspots.

### 3.3.2.5 $\delta$ -Duration and Emergence Type

As shown in the left panel of Figure 3.21, more magnetically complex ARs have longer  $\delta$ -duration. We already confirmed that more magnetically complex ARs have larger maximum umbral area in Figure 3.18.

In general, larger sunspots have longer lifetime (Gnevyshev, 1938; Waldmeier, 1955). Recurrent sunspot groups are found to exhibit a slightly larger lifetime than that based on the Gnevyshev-Waldmeier relationship by Petrovay and van Driel-Gesztelyi (1997). It is also well known that larger sunspots tend to be darker and have stronger magnetic fields (Solanki, 2002; Livingston, 2002). Furthermore, Shi and Wang (1994) reported that the productivity of  $\delta$ -spots for X-class flares is closely correlated to the lifetime of  $\delta$ -spots. Our result suggests that the long lifetime of active  $\delta$ -spots is closely related to their magnetic complexity (twist and writhe). Although magnetic tubes are eventually dispersed due to the action of turbulent convection (Petrovay and Moreno-Insertis, 1997) and/or fragmentation by fluting instabilities, the twisted tubes are more resistant against these dissolving actions. It seems difficult that the magnetic lines of force of the tube above the solar surface will be torn off by convective motions in lower layers, as the lines of force are entangled and hooked to the magnetic tube in the corona. Further, the twist will suppress the fluting instability of magnetic tubes (Priest, 2014). Therefore, we argue that the longevity of an active  $\delta$ -spot depends on its magnetic twist.



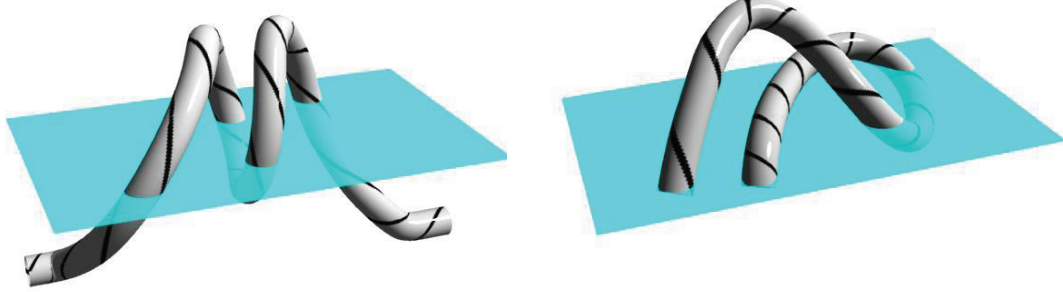


Figure 3.20: Schematic models for  $\beta\gamma\delta$  ARs. The left panel shows a general model for the downward-knotted type such as NOAA 10826. The right panel shows a possible model for the “top-to-top” type such as NOAA 10720.

### 3.3.2.6 Possible Power-law Relations among Parameters

On every scatter plot (Figures 3.18 and 3.21), we performed the power law fitting to the data. Two methods were used to derive the power-law index  $k$ . The first is the classical least-squares fitting (C-LS) to log-log plots and we obtain the power-law index  $k_C$ . The second is the non-linear least-squares fitting (NL-LS) method based on the Gauss-Newton algorithm (*cf.* Hansen *et al.*, 2012), leading to  $k_{NL}$ . For the data points in the left panel of Figure 3.18 ( $S_{U_{\max}}$  vs. FI in the observed period), we found  $k_C = 1.21 \pm 0.24$  and  $k_{NL} = 1.61 \pm 0.33$ . In the right panel of Figure 3.18 ( $S_{U_{\max}}$  vs. FI in the  $\delta$ -state), we found  $k_C = 1.30 \pm 0.31$  and  $k_{NL} = 1.87 \pm 0.50$ . FI follows a power-law dependence on  $S_{U_{\max}}$  with an index around 2, especially in the  $\delta$ -state. It is worthwhile to note that Magara (2014) discussed a power-law relationship between the magnetic free energy and the total magnetic flux for twisted emerging loops with an index of 2 from his numerical simulation.

We next show the relation between the  $\delta$ -duration and FI in the  $\delta$ -state (left panel of Figure 3.21). Although we could not get the converged solution of NL-LS, we obtained  $k_C = 1.54 \pm 0.34$  when we excluded the “others” group as they have large dispersion. For the relation between the  $\delta$ -duration and  $S_{U_{\max}}$  in the  $\delta$ -state (right panel of Figure 3.21), we found  $k_C = 0.76 \pm 0.16$  and  $k_{NL} = 1.07 \pm 0.28$ . Combining the last two relations, namely both plots of Figure 3.21, we can infer a power-law relation  $FI \sim S_{U_{\max}}^{2.0}$  from C-LS which is consistent with the result derived in the previous paragraph.

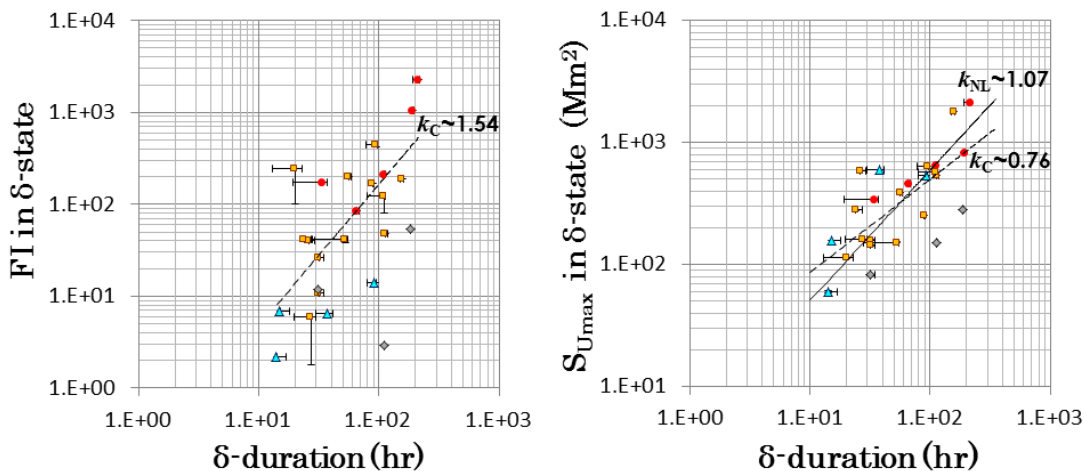


Figure 3.21: Flare Index (left) and maximum umbral area (right) in the  $\delta$ -state as a function of the  $\delta$ -duration. The symbols are the same as in Figure 3.18. Six ARs which showed no flare activity in the  $\delta$ -state were excluded. The error-bars were assigned by considering the effect of data gaps (see text). The results of non-linear least-squares fitting (power-law index  $k_{NL}$ ) and classical least-squares fitting (power-law index  $k_C$ ) are shown by the solid and the dashed lines, respectively.

### 3.4 Discussion

By paying attention to the initial phase of  $\beta\gamma\delta$  ARs in Cycle 23, we investigated what are the important configurations which lead to the flare activity. From our investigation, we discovered three representative topological types which have strong correlations with the flare activity, namely “quasi- $\beta$ ”, “writhed”, and “top-to-top”. We confirmed that the ARs with higher topological complexity show stronger flare activity.

It is interesting to note that almost all ARs classified as the “writhed” type are of DK type. Once the downward knot structure is formed, a dense plasma “reservoir” is formed in the knot and the whole structure of the flux tube may become stable owing to the effect of the mass as an anchor (left panel of Figure 3.20). Under a different situation, Magara (2003) proposed a similar idea in their numerical simulation of the emergence of a twisted flux tube in the convection zone. Subsequently, Magara and Longcope (2011) has studied the case of the emergence of a U-loop formed below the photosphere. van Driel-Gesztelyi *et al.* (2000) have reported that the emergence of a U-loop which connected the opposite polarity legs of two  $\Omega$ -loops below the photosphere. Recently, Poisson *et al.* (2013) studied the possibility of a downward kinked structure in the mid part of NOAA10314. Thus the idea of DK structure is not so exceptional and applicable to twisted magnetic tubes, with several evidence. The DK structure as an anchor may contribute to the stability of the AR.

Subsequently we checked the case of the “top-to-top” group. They show clear twist

and writhe structures with common handedness (three cases out of five). Therefore, we infer that the three-dimensional collision is not an accidental one but is attributed to the extreme development of a writhing structure. For example NOAA10696, classified as the “top-to-top” type, had the second strongest FI in our sampled ARs and showed both characters of three-dimensional collision and downward knotted structure. The AR is namely a hybrid type of “writhed” and “top-to-top”. Such a configuration of this AR reminds us that there may be continuity of developments between the “top-to-top” and “writhed” structures. We propose a schematic model for NOAA10720 with a highly writhed structure as shown in Figure 3.20 (right panel). We can point out that a similar, highly writhed model for NOAA 7926 was proposed by Pevtsov *et al.* (1998).

Brown *et al.* (2003) studied the rotation of seven sunspots using high resolution white light images with TRACE. They proposed that a possible mechanism for sunspot rotation is the emergence of a pre-twisted flux tube. On the other hand, Yan *et al.* (2009) claimed that the rotation of sunspots originates from the photospheric flows, based on their study of combined photospheric and coronal observations. In our study, the rotation of sunspots themselves and the tilt angle rotation of EFR are rarely observed in small and flare-inactive ARs. If the rotation is mainly attributed to photospheric flows, rotational motions of sunspots will be observed commonly regardless of the sunspot size. However, as shown in our statistical study, the ARs of prominent twist and writhe had larger area and showed stronger flare activity among the sampled ARs. In addition, as described in Section 3.3.2.5, the pre-twisted flux tube model is in harmony with several features of  $\delta$ -spots. Therefore we conclude that the origin of sunspot rotation is the emergence of the pre-twisted flux tube.

It is known that twist and writhe helicities transform each other in an ideal thin flux tube (Călugăreanu, 1959; Moffat and Ricca, 1992; Ricca and Moffat, 1995; Török *et al.*, 2010). In this study, we adopted a picture in that the initial twist of ARs will be mostly generated by turbulent flows in the convection zone. When the twist increases in an AR, the twist transforms into the writhe in the middle part of the flux tube by the kink instability (Török *et al.*, 2010). Then it is natural to find the sign relationship as seen in this study. The previous studies have shown that the kink instability facilitates the formation of  $\delta$ -spots (*e.g.* Linton *et al.*, 1999). Tian *et al.* (2005) pointed out that the signs of twist and writhe tend to agree in well-developed ARs under kink instability.

Regarding the classification of  $\delta$ -spots, we review the relations between the types classified by our study and the types by Zirin and Liggett (1987) as introduced in Section 1. We can consider that the first type of Zirin and Liggett (ZL) is the same as the “top-to-top” type of ours. The third type of ZL may be equal to the “writhed” group, although we believe that the configuration is not formed by different dipoles but by a connected structure below the photosphere. However, the second type of ZL was seldom observed in our study. This type was seen in only one or two cases in

the “others” group of our study. This type may be more likely to occur in recurrent sunspots rather than in sunspots in their young stage studied here. The “quasi- $\beta$ ” type was not considered in the ZL classification as they may not produce notable flares.

We discussed the possible power-law relations among the  $\beta\gamma\delta$ -spot parameters. Our physical interpretation is as follows. FI is a good proxy of the total energy released in flares in an AR and thus is a measure of the total magnetic free energy of the region supplied by the gas flow field. The maximum umbral area  $S_{U\max}$  is a measure of the magnetic flux of the region. The functional relation of a power law sometimes is interpreted as the evidence of a scale-free process (Shimizu *et al.*, 1995; Shimojo *et al.*, 1999; Nishizuka *et al.*, 2009). In our case, the total free energy supply or injection can be considered as due to a kind of scale-free processes, probably the helicity injection process by the turbulent convective flows or the differential rotation. The process seems to work independent of the total amount of magnetic flux. The difference in FI among the emergence-type groups may be the difference in topology of the magnetic tubes. While the “quasi- $\beta$ ” type may have a simple form with less twist and less free-energy, the “writhed” type may have a singly knotted or kinked tube with more free-energy, and the “top-to-top” type may have a doubly or multiply knotted tube with much more free-energy.

### 3.5 Conclusions

We have studied the initial evolution of 31  $\beta\gamma\delta$  ARs and derived the following conclusions.

- i) From the point of view of topology, emerging  $\beta\gamma\delta$  ARs can be classified broadly into three categories: “quasi- $\beta$ ”, “writhed”, and “top-to-top”. The “top-to-top” type has the most complex topology and the “quasi- $\beta$ ” type is the simplest type. The “writhed” group has medium complexity among the three types.
- ii) ARs of more complex topology tend to exhibit higher flare activity.
- iii) The signs of twist and writhe both tend to be consistent with each other in the “writhed” type.
- iv) The downward-knotted structure in the mid portion of the flux tube is the essential element of active  $\beta\gamma\delta$  ARs.
- v) The flare activity of  $\beta\gamma\delta$  ARs are highly correlated not only with the sunspot areas but also with the magnetic complexity.
- vi) There is a possible scaling-law between FI and  $S_{U\max}$ .

Finally, we will give some comments on the future extension of our study. Direct measurements of magnetic helicity will be essential to study the free-energy accumulation in ARs. Observations of the ARs throughout their lifetime along with stereoscopic views from space will be desirable. Further it will be an important challenge to diagnose

the magnetic topology of ARs in the convection zone by improving local helioseismology.



## Chapter 4

# Prominent Photospheric Downflows on Magnetic Neutral Line in a delta-type Sunspot

### 4.1 Introduction

Active regions are known to be born as emerging flux regions (EFRs), develop their complexities and then decay after exhibiting explosive activities. Among them,  $\beta\gamma\delta$  active regions are known to show highly energetic flare activities (Sammis *et al.*, 2000). However, some  $\delta$  regions do not show so much violent activities (Zirin and Liggett, 1987). During the surveying study of  $\beta\gamma\delta$  regions, we found an indication of submergence of magnetic flux in an inactive and decaying  $\beta\gamma\delta$  region.

We will report the temporal behavior of the region as a case study of magnetic flux decay of the region. In general, the reduction of the observed surface magnetic flux can be attributed to processes such as submergence, rapid or slow dissipation, diffusion by turbulent flow, and reconnection. Submergence was studied by many researchers until now (Wallenhorst and Howard, 1982; Wallenhorst and Topka, 1982; Rabin *et al.*, 1984; Zirin, 1985; Harvey *et al.*, 1999; Kálmán 2001; Chae *et al.*, 2004; Kubo *et al.*, 2010; Iida *et al.*, 2010).

Zirin (1985) studied submergence of small dipole in AR BBSO 18962 and he proposed that the flux loop was pulled back down by magnetic tension and submerged.

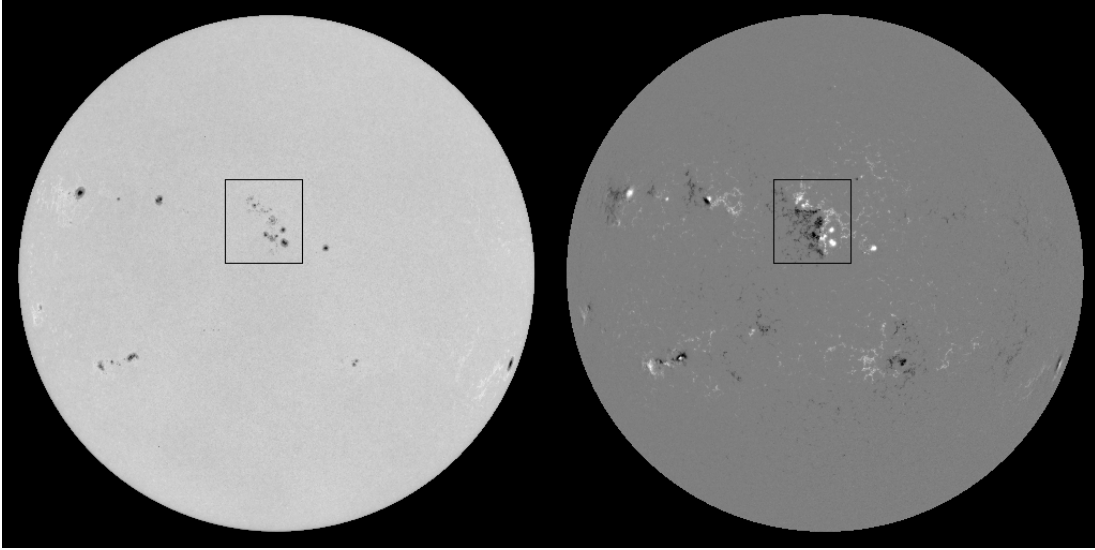


Figure 4.1: White light image and magnetogram of active region NOAA 9957 observed with SOHO-MDI on 2002 May 22 11:12 UT

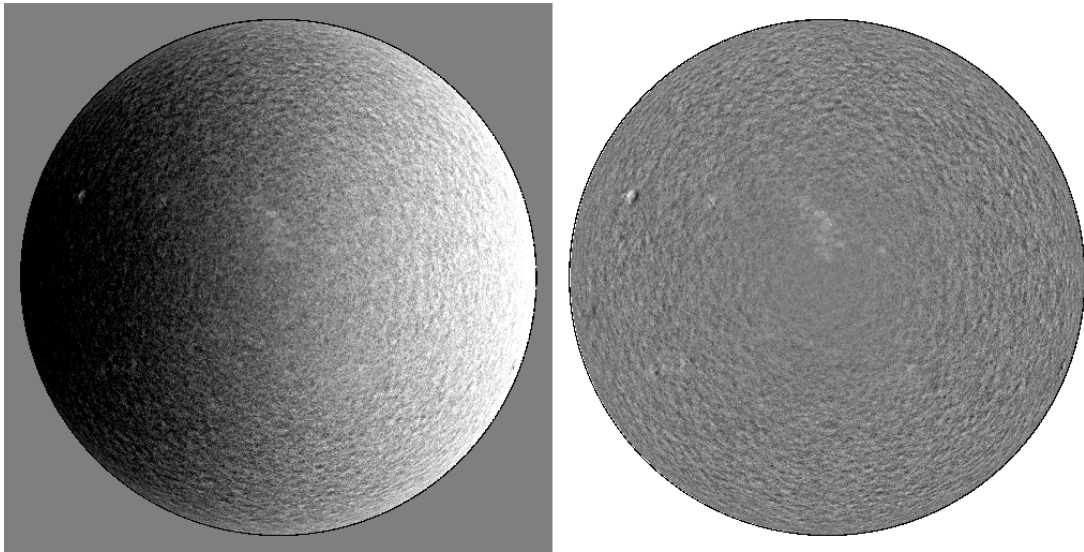


Figure 4.2: Raw image of MDI Dopplergram (left) and corrected image for solar rotation and 5 min oscillation (right).

Harvey *et al.* (1999) studied the disappearance timing of magnetic bipoles in different layers (photosphere, chromosphere and corona). They detected the bipoles disappeared earlier in the chromosphere and corona than in the photosphere for 44% of cancelling bipoles. They considered that these cases of magnetic flux cancellation are due to submergence.

Chae *et al.* (2004) reported two cases of  $1 \text{ km s}^{-1}$  downflow near the neutral line (NL) at small cancellation sites in NOAA 10043, and they considered that the flow corresponds to the  $\Omega$  loop submergence of magnetic flux tube. Recently, using *Hinode* SOT



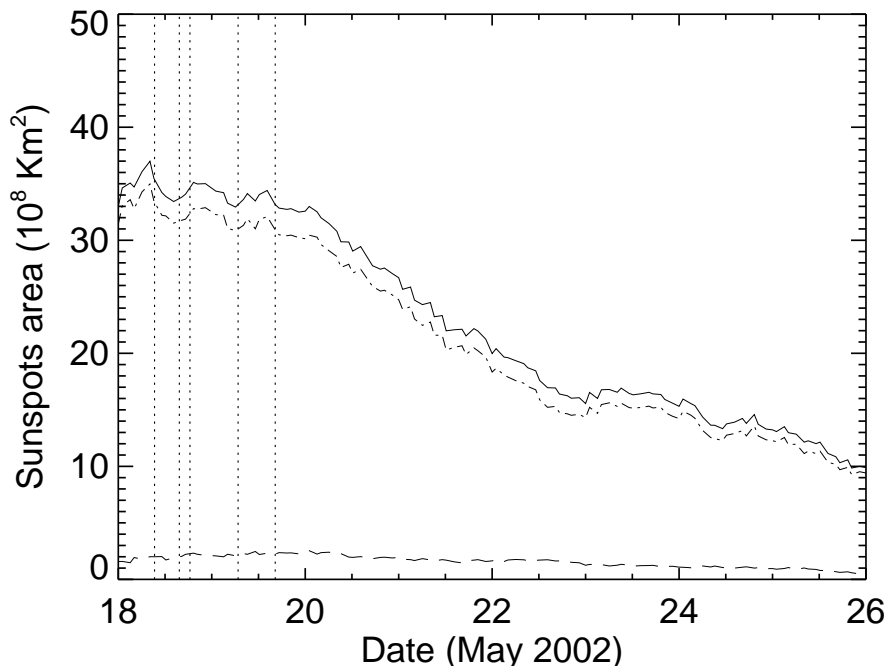


Figure 4.3: Temporal variation of sunspot area. Solid line, dashed-dotted line and broken line represent sunspot area, penumbral area and umbral area, respectively. Vertical dotted lines represent occurrence time of C class flares by GOES X-ray data.

data, Kubo *et al.* (2010) and Iida *et al.* (2010) reported respectively small magnetic flux submergence at flux cancellation site in quiet region.

These previous works reveal that magnetic flux submergence will occur in some flux cancellation sites without any eruption events and that the submergence are rather common phenomena in spite of prevailing buoyant character of solar atmosphere.

Active region NOAA 9957, we report in this paper, was classified as  $\beta\gamma\delta$ -type and showed low activities. We studied the region using data from Michelson Doppler Imager (MDI, Scherrer *et al.*, 1995) on board the *Solar and Heliospheric Observatory* (SOHO) satellite for photospheric velocity field and we discovered prominent downflow of  $1.5 \text{ km s}^{-1}$  which lasted about 17 hrs near the NL. The observational result strongly suggests the occurrence of submergence in the decay phase of  $\beta\gamma\delta$  regions.

## 4.2 Data & Analysis

The active region NOAA 9957 was observed for 13 days from 2002 May 16 to 2002 May 28 on solar disc ( $N3^\circ$ - $N15^\circ$ ). No flare activities were reported from May 20 to May 26 in the region, although NOAA 9957 was classified as a  $\beta\gamma\delta$  spots during 10 days from May 17 to May 26 (Figure 4.1).

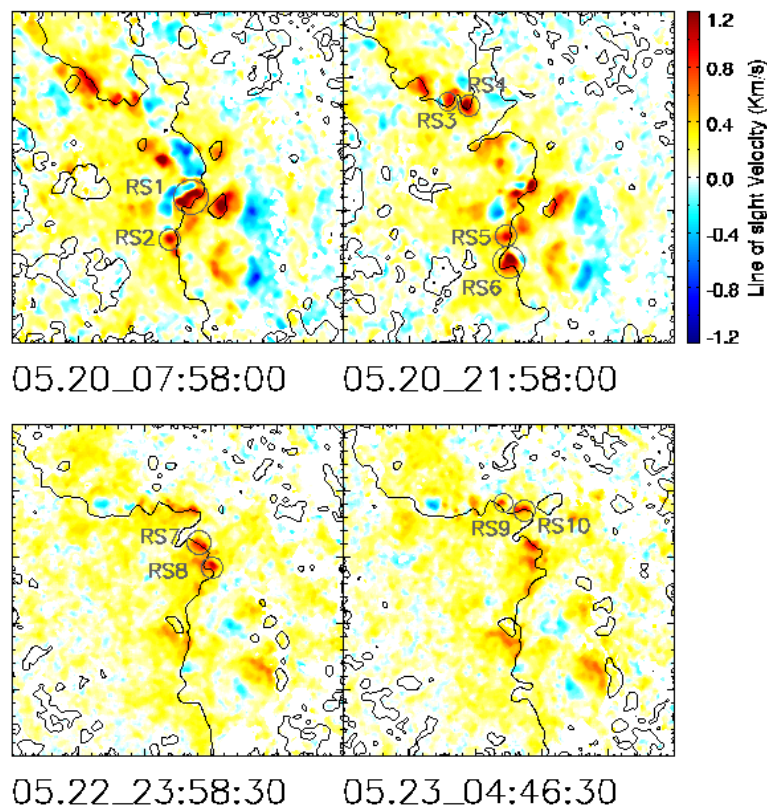


Figure 4.4: Temporal evolution of Doppler velocities in the active region NOAA 9957. The field of view(FOV) is  $250'' \times 250''$  for each panel. Magnetic neutral lines are overlaid with black lines. Prominent redshift patches are indicated with circles. North is up and west to the right in these and subsequent maps.

In this study, we use MDI Dopplergrams, magnetograms and continuum images on board SOHO satellite. The data on the magnetic field and white light images have a time resolution of 96 min, while Dopplergrams, line of sight (LOS) velocities, have a time resolution of 1 min. These data have a spatial resolution 2 arc sec per pixel. Partially, Dopplergrams of spatial resolution 0.6 arc sec per pixel are included for analysis after May 22 20:00 UT. Although here, we describe analysis method about normal mode data of Dopplergrams, we have treated high resolution mode data in a similar manner.

For preparation of our analysis using Dopplergrams, first, we removed the solar rotation with the following method. We made mean Doppler image by averaging all the Doppler images (7689 images) during almost 4 days (from May 18 to May 22), and subtracted the mean image from each images. Secondly, we corrected for the 5 min oscillation by averaging every sequential 4 images (Figure 4.2).

From the time series of magnetograms, we derived the horizontal velocity fields of magnetic feature by local correlation tracking (LCT, November *et al.*, 1988) method in 96 min temporal step with a window size of 5 by 5 arc sec.

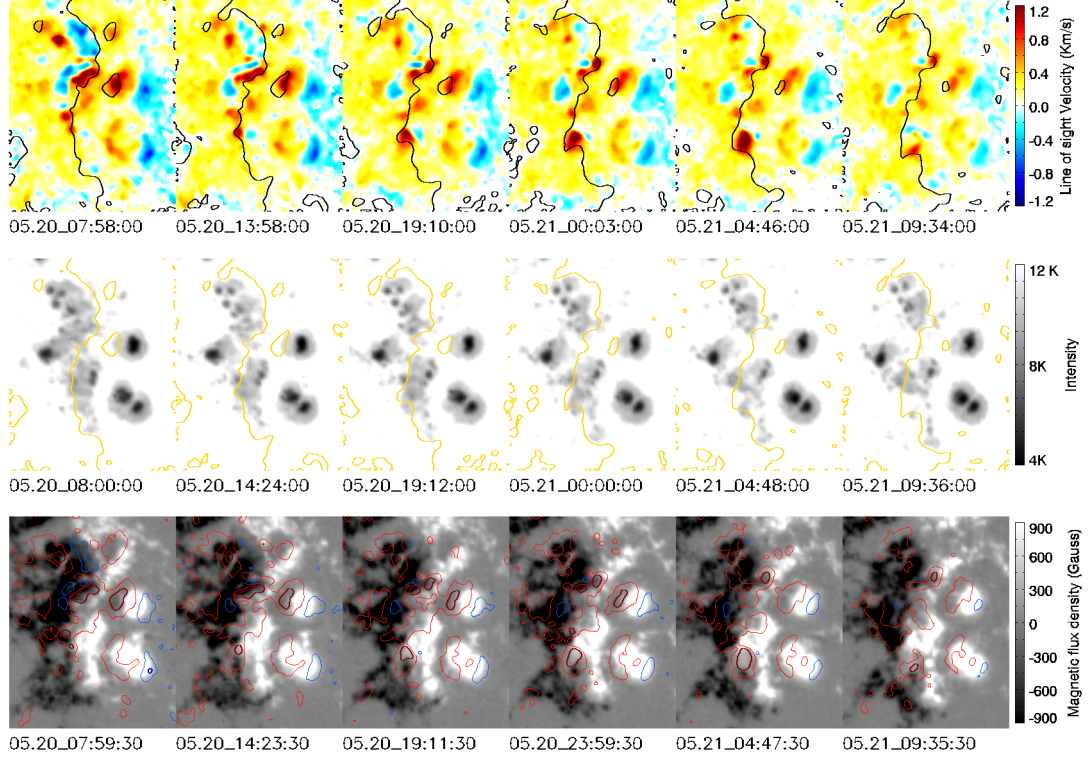


Figure 4.5: Temporal evolution of the most prominent downflow (RS6). The FOV is  $130'' \times 165''$  for each panel. Time steps of Dopplergram, white light image and magnetogram are shown from left to right for each row. Magnetic neutral lines are drawn in top and middle rows. On the bottom panel, dark red contours, light red contours, light blue contours represent  $800 \text{ m s}^{-1}$ ,  $300 \text{ m s}^{-1}$  for redshifts and  $300 \text{ m s}^{-1}$  for blueshifts, respectively. Dark blue contour which represents  $800 \text{ m s}^{-1}$  blueshifts is only in the bottom far left panel on the positive spot at south-west.

In addition, we applied a labeling method (connected component labeling) to identify notable redshift patches. Our labeling method with binary image is similar to the one described in Gonzalez and Woods (1992). The redshift patches from Dopplergram data were extracted with a criterion that LOS velocities were above  $800 \text{ m s}^{-1}$ . We identified each notable identical patch between consecutive images visually, and investigated their evolutions.

We defined the sunspot regions, including penumbrae, as darker ones below 0.9 times quiet region brightness and measured their areal variations. (*cf.* Brandt *et al.*, 1990; Chapman *et al.*, 1994).

Magnetic flux values of the region were corrected for the influence of projection effect by dividing each pixel data by  $\cos\theta\cos\phi$ , where  $\theta$  and  $\phi$  represent heliographic longitude and latitude, respectively.

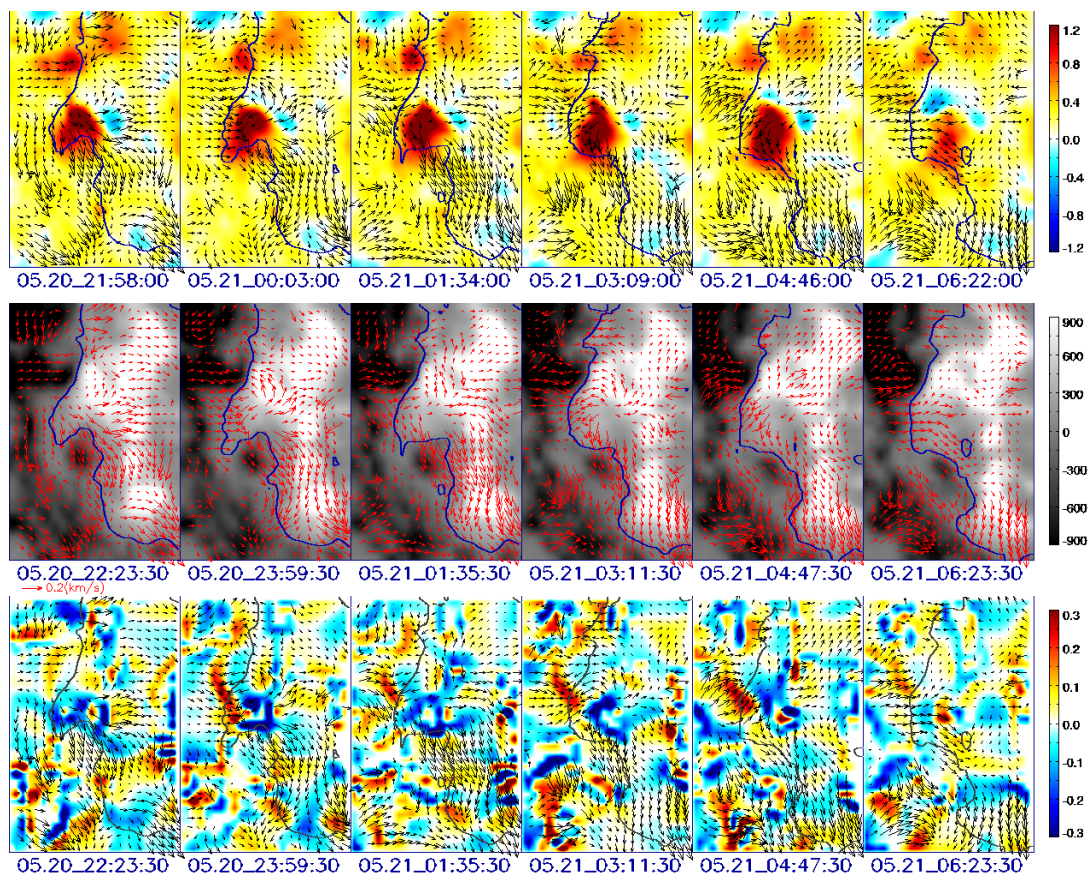


Figure 4.6: Temporal evolution of horizontal flow. The FOV is  $50'' \times 75''$  for each panel. LCT flow vectors are shown by arrows on the Doppler map in the top row and on the magnetic map in the middle row, respectively. The bottom row shows divergence images for horizontal velocities based on LCT (Reddish colors indicate convergence and bluish colors indicate divergence). Converging flow from both sides to the NL continued from around 00:00 UT to 04:47 UT on May 21 about 5 hrs when the downflow area (RS6) were growing. However converging flows weakened on NL after the decline of the downflow.

### 4.3 Results

Although NOAA 9957 is the most complex sunspot type, i.e.,  $\beta\gamma\delta$  region, the area rapidly decreased in the observation period from 2002 May 20 to May 26 without any flare activity (Figure 4.3). The region was in the decay phase. We have found several redshift patches around the magnetic neutral line in this AR (Figure 4.4).

#### 4.3.1 Case Study of Most Prominent Redshift Patch

The most prominent downflow (RS6 in Figure 4.4) appeared in NOAA 9957 from 2002 May 20 to 21 about 17 hrs in  $1.0 \text{ km s}^{-1}$  level. RS6 located at  $5^\circ$  north latitude. In this case, downflow contour of  $300 \text{ m s}^{-1}$  includes both magnetic polarity areas (Figure 4.5).

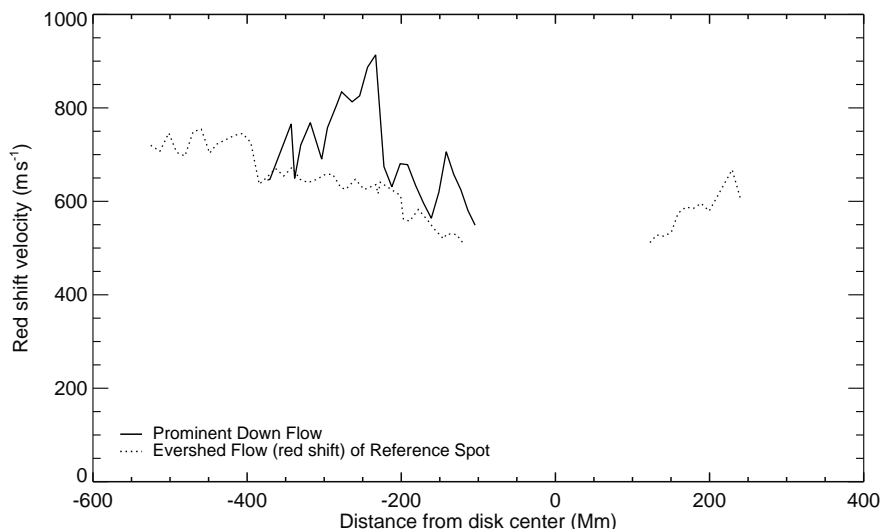


Figure 4.7: Solid line and dotted line represent temporal evolution of prominent downflow in RS6 and that of Evershed flow (redshift part) of the reference round spot NOAA 9958, respectively. The velocities was median value inside the area contoured by  $500 \text{ m s}^{-1}$  LOS velocity.

RS6 disappeared suddenly and penumbral area at RS6 decayed simultaneously. Visual inspection of magnetogram movies tell us that moat flows continued steadily from the two stable sunspots of positive polarity located west of NL during the observation period. Neighboring negative polarities also moved on from east side to NL. These converging horizontal flows to the NL at the downflow area were also confirmed by LCT method (Figure 4.6). The converging flows accompanied the growth of the downflow area and continued about 5 hrs.

Figure 4.7 shows the temporal variation of LOS velocity for the prominent redshift patch (RS6) with that of typical Evershed flow (redshift part) for reference. In this figure, the abscissa is taken as the distance from disc center. The median values above  $500 \text{ m s}^{-1}$  in these areas are taken as representative values. The redshift flow in RS6 showed no pairing blueshift area, transient occurrence, different evolution and larger Doppler velocity compared to Evershed flows. So the flow in the RS6 is not due to Evershed flow. Furthermore, if the observed redshift is due to horizontal flows, the dependence of Doppler amplitude on the distance from disc center will be similar to the Evershed flows. As the Doppler shift in the RS6 behaves so differently, we may conclude that the observed shift is mainly due to downflow to lower layers.

Next let us see the magnetic field around the RS6. Vector magnetogram data obtained at *Huairou Solar Observatory Station* (HSOS) (Figure 4.8) shows that magnetic lines of force ran parallel to the solar surface at the RS6 area. Continuous downflow at horizontal magnetic flux corresponds to the penumbral area decay spatially and

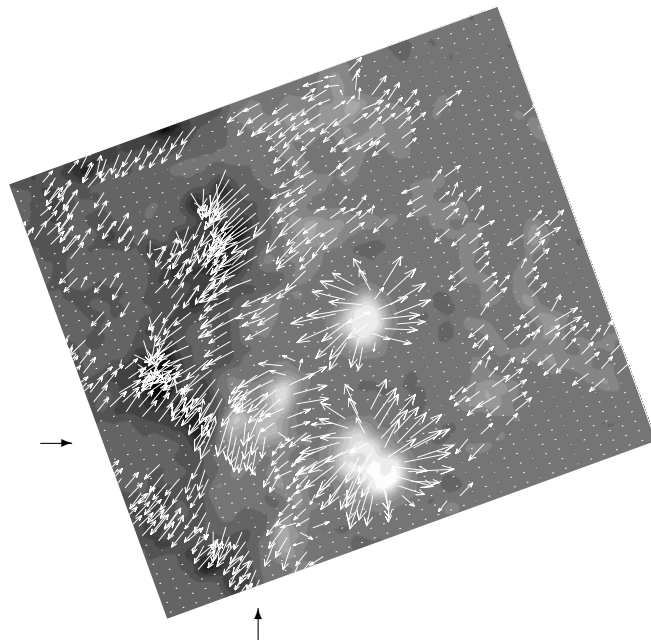


Figure 4.8: Vector magnetogram data obtained at *Huairou Solar Observatory Station* (HSOS) on 2002 May 21 0350 UT. RS6 is around the cross point of outer black arrows. This figure shows that magnetic lines of force ran parallel to the solar surface at the RS6 area.

temporarily. These observed results strongly suggest occurrence of a submergence of magnetic  $\Omega$  loop structure in the area.

### 4.3.2 Statistical Study of Redshift Patches

We investigated all the redshift patches in NOAA 9957 that showed redshifts above  $800 \text{ m s}^{-1}$ . Following criteria were used for selection of the patches: They (1) had redshift above  $800 \text{ m s}^{-1}$ , (2) occurred near the NL, (3) located within about  $30^\circ$  of the central meridian, (4) had no characteristics of Evershed flow, (5) had clearly identifiable for longer time than 4.5 hrs (to be found at least consecutive 4 images with 96 min cadence).

As a result, we found 9 cases which satisfied above criteria. We studied the correlation between their LOS velocities and life times and summarized the result in Figure 4.9. Maximum velocity during the life time of each patch is taken as a representative value. We can see that almost all of redshift patches have velocities around  $1 \text{ km s}^{-1}$  at maximum and do not depend on their lifetimes. Majority of them have lifetimes less than

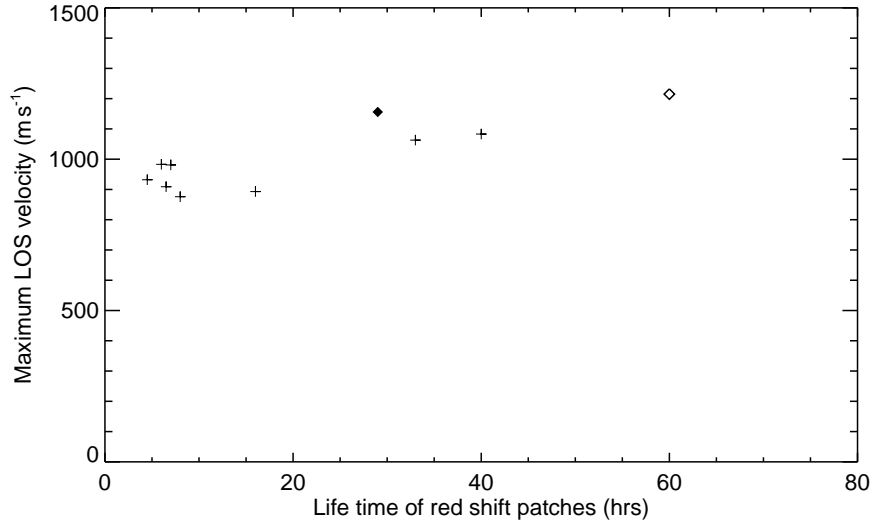


Figure 4.9: Maximum LOS velocities during the life time of redshift patches near the NL in NOAA 9957. The velocities were adopted median value inside area contoured by  $800 \text{ m s}^{-1}$  LOS velocity. Black diamond represents RS6 which continued 29 hrs at  $800 \text{ m s}^{-1}$  level. White diamond RS1 is shown only for reference. RS1 was observed far from the solar meridian ( $\sim$  east longitude  $45^\circ$ ) and may be influenced by horizontal flow.

20 hrs and they show pulse-like temporal evolution as that of RS6. Their transient activities were observed to be intermittent.

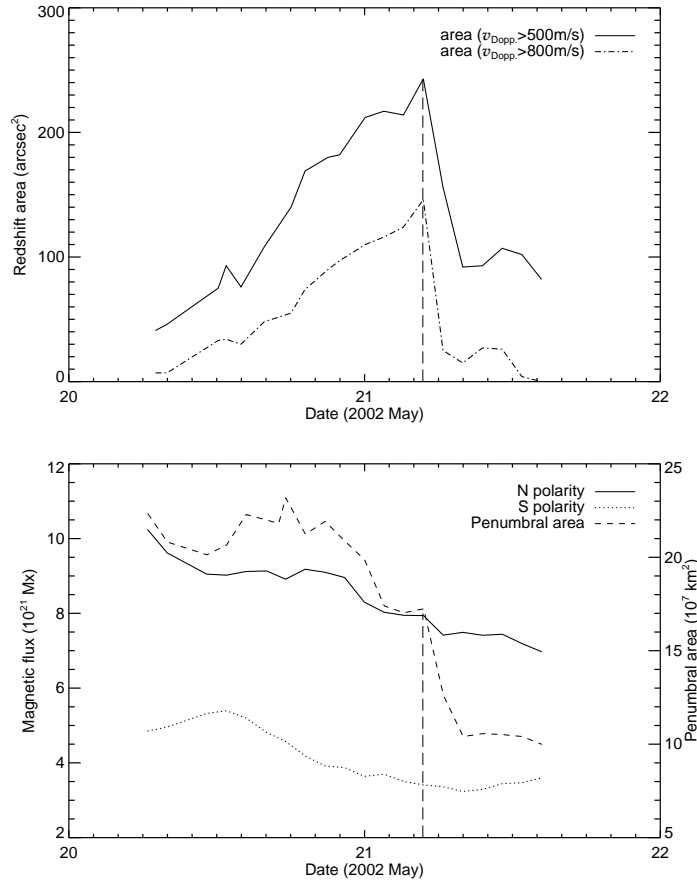


Figure 4.10: Top panel shows temporal evolution of the redshift area for RS6. Solid line and dashed-dotted line represent the areal evolution of  $v_{Dopp.} > 500 m s^{-1}$  and of  $v_{Dopp.} > 800 m s^{-1}$ , respectively. Bottom panel shows temporal evolutions of the magnetic flux and penumbral area for RS6. Solid line, dotted line and broken line represent positive polarity flux, negative polarity flux and penumbral area. We can see the positive polarity flux decrease 30 % and negative polarity flux decrease 20 % in one day from May 20 to May 21. Vertical broken lines in both panels represent the epoch time where the penumbral area shows dramatic decay.

## 4.4 Discussion and Conclusions

There are several possibilities for disappearance of active regions: magnetic diffusion, magnetic reconnection, submergence etc. The active region NOAA 9957 in this study decreased the penumbral area 46 % from May 20 00:00 UT to May 22 12:00 UT. Decreasing rate for penumbral area was 22 % per day in that 2.5 days.

Our study shows that the penumbral decay mainly occurs in the vicinity of the NL, and must be strongly associated with magnetic flux cancellations. For instance, in a very small area ( $20'' \times 25''$ ) including RS6, the magnetic flux dropped by 30 % during only one day (Figure 4.10), and this reduction accompanied the extreme



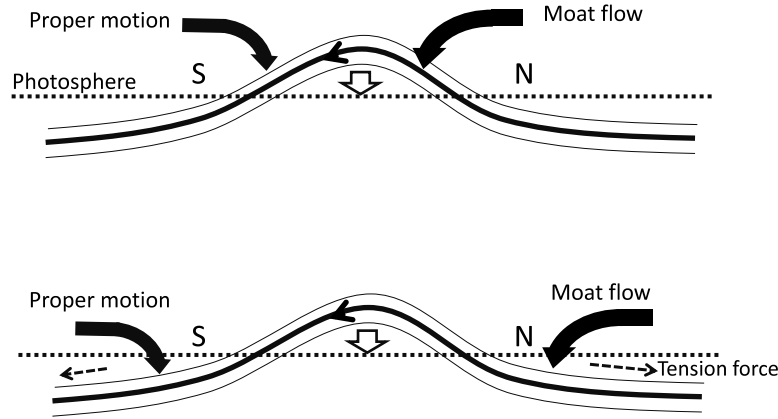


Figure 4.11: Schematic image of magnetic flux submergence. Top panel represents that the moat flows mainly act the magnetic flux above the solar surface and directly drag the flux to downward below the surface. Bottom one shows that moat flows act the flux below the surface and enhance the magnetic tension force.

penumbral decay in the prominent downflow area of RS6. We consider that downflow activities may cause rapid decay of this AR. In the following we will discuss the possible mechanism of the rapid decay of NOAA 9957.

First, let us consider the diffusion mechanism. Howard and Labonte (1981) examined magnetic field measurements at the Mt. Wilson, done from 1967 to mid-1980. They found that the rate of disappearance of magnetic flux from active latitudes is about 10 % per day of the total flux. And they pointed out that the disappearance of active region fields are not due to diffusion, but advection to polar latitude by meridional flow. Wallenhorst and Howard (1982) checked temporal evolution of average magnetic flux for 25 ARs. Their analysis indicated that the average rate of flux disappearance is also about 10 % per day. The weak background fields below 10 G around ARs show no increase corresponding to the decrease of total magnetic flux above 10 G field. Thus, they concluded that diffusion does not play an important role in the disappearance of the flux. Wallenhorst and Topka (1982) also reported similar results for the small sunspot group associated with Hale AR 17694.

Second, the possibility of reconnection would be checked. When the magnetic reconnection occurs frequently, we can expect that the magnetic flux decreases rapidly and that X-ray emission is strong. As GOES X-ray intensity was in low level and did not showed the occurrence of strong flares during our period of study, we can rule out the reconnection as the mechanism of the decay of NOAA 9957.

Finally, possibility of submergence will be considered. Let us discuss the directions of flows in the redshift patches. Are they horizontal or vertical? As mentioned above in

Sec. 3.2, the strong Doppler signals observed near the NL are almost all redshifts. If we suppose this phenomenon as horizontal flows with fixed direction, the Doppler signals must change red to blue (or blue to red) when the patches cross the solar meridian. However we never detected such an effect. When the horizontal flows have random directions, it is highly likely that both redshifts and blueshifts will be found. This possibility is ruled out from the observational results. So the flows in the redshift patches will be vertical.

Another argument support the view of vertical flow. RS7 took place near the meridian (W6°-W7°, N13°) and always indicated redshift velocity of around  $1 \text{ km s}^{-1}$ . If the redshift is due to horizontal flow, the absolute flow speed reaches  $4 \text{ km s}^{-1}$ . It is not likely that such a sonic-speed level phenomena occurs in the photosphere and lives for several hours, which have never been reported.

In case of RS6 as mentioned in Sec.3.1, converging flows near the NL would make the gas density high. So the horizontal converging flows will turn to downward directions around the NL, by gravitational force. We also notice that the converging flows will convect the foot points of magnetic flux tube to the NL. We expect that these effects will drive downward motion of magnetic flux tubes near the NL as will be discussed in the next paragraphs.

We propose physical pictures for explaining the phenomenon in Figure 4.11. Moat flows continued almost during the observational period from the two positive polarities adjacent to the strong downflow area. The proper motion of negative polarities from east to NL also continued for a long duration (May19-22). There are two possibilities for the action of drag force of moat flows which works magnetic flux above or below the solar surface. One is that, the moat flows mainly act the magnetic flux above the solar surface and directly drag the flux to downward.

Another possibility is that moat flows act the flux below the surface and enhance the magnetic tension force. Since the magnetic buoyancy is balanced with the magnetic tension force in the emerged and stabilized magnetic flux tube, we get a following relation (*cf.* Parker, 1955, 1984; Priest, 1982):

$$(\rho_e - \rho_i)g \sim \frac{B_i^2}{\mu L_c}, \quad (4.1)$$

where  $\rho_e$  and  $\rho_i$  represent the mass densities outside the tube and inside the tube, respectively.  $L_c$  is the critical separation of the anchor points for the emerging tube. Pariat (2004) pointed out that  $L_c$  is around 2000 km. Converging flows as shown in Fig.11 will force to reduce the separation of the anchor points of bipoles. When  $L$  becomes lower than  $L_c$ , the magnetic tension force overcomes the magnetic buoyancy. Then the magnetic bipoles will submerge. When the plasma flows from both sides of NL continued 5 hrs with velocity of  $0.1 - 0.2 \text{ km s}^{-1}$  at the surface as shown in Fig. 6, both foot points separated around 7000km ( $\sim 10''$ ) will come together by 5000 km.

So the foot points separation of the magnetic tubes near the NL become smaller than  $L_c$  ( $\sim 2000$  km) and the submergence of tubes will be driven near the NL.

This simple estimation tells us that continuous converging flows near the NL can trigger the submergence not only in  $\delta$ -type sunspots as NOAA 9957 but also in any other type sunspots. If the magnetic tube lies nearly horizontally and weakly convex to the vertical, submergence is likely to be driven by converging horizontal flows.

During solar disc passage of NOAA 9957, there are many redshift patches near the NL as described in 4.3.2. So we can presume that these phenomena of submergence are rather common and that they have not been detected behind the violent activities.

So we get our conclusion on these phenomena in the AR NOAA 9957 as follows.

- i) In a rapidly decaying  $\beta\gamma\delta$ -type AR NOAA 9957, we have detected continuous and prominent downflows on magnetic neutral line.
- ii) The downflow motions occurred intermittently with an average lifetime of 12 hrs.
- iii) Near the downflow area, converging horizontal flow to the NL from both sides was found to continue almost 5 hrs. We suppose that the moat flow motions from two large positive polarities promote or drive the phenomenon.
- iv) Several submergences occurred along the NL which were accompanied by the flux cancellations and low flare activities.

We suggest that these phenomena may be one of the mechanisms of active region decay irrespective of sunspot type.



## Chapter 5

# Conclusions and Discussion

### 5.1 Conclusions

The property of  $\beta\gamma\delta$ -spots as the most flare active sunspot group have been found by Sammis *et al.* (2000). However, there were uncertainty about the paths of  $\delta$ -formation and the specific characters of emergence in the  $\beta\gamma\delta$ -spots. In this thesis the author shed light on these points and unveiled that there are much differences of flare activity level of each emerging type in  $\beta\gamma\delta$ -spots. The author also investigated the decay phase of  $\beta\gamma\delta$ -spots.

The results of investigation of the evolution and decay of  $\delta$ -spots lead to the following conclusions:

- i) From the point of view of topology, emerging  $\beta\gamma\delta$  ARs can be classified broadly into three categories: “quasi- $\beta$ ”, “writhed”, and “top-to-top”. The “top-to-top” type has the most complex topology and the “quasi- $\beta$ ” is the simplest type. The “writhed” group has medium complexity among the three types.
- ii) The ARs of more complex topology tend to exhibit higher flare activity.
- iii) The both signs of twist and writhe tend to be consistent with each other in “writhed” types.
- iv) We infer that downward-knotted structure in the mid portion of the flux tube are the essential elements of the active  $\beta\gamma\delta$  ARs.
- v) The flare activity of  $\beta\gamma\delta$  ARs highly correlate not only with the sunspot areas but also with the magnetic complexity.
- vi) We suggest a possible scaling-law between FI and  $S_{Umax}$ .
- vii) In a rapidly decaying  $\beta\gamma\delta$ -type AR NOAA 9957, we have detected continuous and prominent downflows on magnetic neutral line.
- viii) The downflow motions occurred intermittently with an average lifetime of 12 hrs.
- ix) Near the downflow area, converging horizontal flow to the NL from both sides was found to continue almost 5 hrs. We suppose that the moat flow motions from two large positive polarities promote or drive the phenomenon.

x) Several submergences occurred along the NL which were accompanied by the flux cancellations and low flare activities.

## 5.2 Discussion

The thesis has exhibited the four primary challenges at the preface, namely the formation of  $\delta$ -configuration, the flare occurrence conditions, the cause of long life for  $\delta$ -spots, and the decay of  $\delta$ -spots. Next, we will show our answers for these challenges in the order.

### 5.2.1 Formation of $\delta$ -Configuration

*How are  $\delta$ -spots born and how do they develop?*

We have checked the initial emerging phase of  $\delta$ -spots in details in Chapter 3. From our investigation, we discovered three representative topological types which have strong correlations with the flare activity, namely “top-to-top”, “writhed”, and “quasi- $\beta$ ”. We also confirmed that the ARs with higher topological complexity have stronger flare activity.

Particularly, in the case of “writhed” type, the handedness of twist and writhe agree to each other in the most cases, namely 12 cases out of 13. From this result, we propose a magnetic model that the emerging flux regions in an  $\beta\gamma\delta$  AR are not separated but united as a singly connected structure below the solar surface.

### 5.2.2 Flare Occurrence Conditions in $\delta$ -State

*What conditions make flare occurrence at  $\delta$ -spots?*

Although we cannot get the definite answer of this question at present, we have got some clues of the answer. As the topological complexity increase, both  $S_{Umax}$  and FI distribute to higher values. The relation found in this study clearly indicates that the flare activity of  $\beta\gamma\delta$  ARs depends not only on the umbral area but also on the magnetic complexity. Moreover, it suggests that the large total content of magnetic flux proxied by the umbral area is a necessary condition and the heavy magnetic complexity may be another more stringent necessary condition for the strong flare activation.

### 5.2.3 Cause of Long Life for $\delta$ -Spots

*How do  $\delta$ -spots keep themselves for a long time?*

It is certain that the  $\delta$ -spots have long life times as shown in Chapter 2 (see Table 2.2 and Figure 2.4). Although we could not get a final conclusion on this issue, we can suggest that the strongly twisted magnetic flux tubes have a function against fragmentation by convective motions below the solar surface.

It seems difficult that the surface magnetic lines of force over the tube will be torn off by the action in lower layer convective motions, as the magnetic lines of force are entangled and hooked to the magnetic tube in the corona. Further, the twist are well known to suppress the fluting instability of magnetic tubes (Priest, 2014). So we think that the long life of active  $\delta$ -spot is due to their strong magnetic twist.

To further verify the idea, we need to study the differences of areal evolution among different magnetic types with equivalent sunspot scale.

#### 5.2.4 Decay of $\delta$ -Spots

*How do  $\delta$ -spots decay at last?*

From the preliminary statistical study of flaring ARs described in Chapter 2, we have noticed the existence of inactive  $\delta$ -spots in spite of their long  $\delta$ -duration. In NOAA9957 which is one of such ARs, we detected prominent photospheric down flows near the magnetic neutral line (NL). Then we investigated these phenomena as described in Chapter 4. From the investigation, we consider that the continuous down flows near the NL directly related to the dramatic decay of penumbral area at those places. We interpreted the down flows with penumbral disappearance as the magnetic flux submergence. We claim that the submergence is one of the significant causes of the decay from this study.





# Bibliography

## Chapter 1

Allen, C. W.:1973, *Astrophysical quantities, 3rd ed.*, London: University of London, Athlone Press.

Antalová, A.: 1991, *Bull. Astron. Inst. Czechosl.* **42**, 316.

Aschwanden, M. J.: 2006, *The Sun, Encyclopedia of the Solar System, 2nd ed.*, Chapter 4, Editors: McFadden, L. A., Johnson, T., and Weissman, P., San Diego, CA, USA, Academic Press.

Bhatnagar, A.; Livingston, W.: 2005, *Fundamentals of Solar Astronomy, World Scientific Series in Astronomy and Astrophysics*, WORLD SCIENTIFIC, Edited by Bhatnagar, A. and Livingston, W., vol. 6.

Berger, M. A.; Field, G. B.: 1984, *Journal of Fluid Mechanics*, **147**, 133.

Brandt, P. N.; Schmidt, W.; Steinegger, M.: 1990, *Solar Phys.*, **129**, 191.

Brants, J. J.; Steenbeek, J. C. M.: 1985, *Solar Phys.*, **96**, 229.

Bray, R. J.; Loughhead, R. E.: 1979, *Sunspots*, New York, NY (USA): Dover Publications.

Brunner, W.: 1930, *Astronomische Mitteilungen der Eidgenössischen Sternwarte Zürich*, **13**, 67.

Bruzek, A.: 1967, *Solar Phys.*, **2**, 451.

Bruzek, A.: 1969, *Solar Phys.*, **8**, 29.

Fox, P.: 1908, *Astrophys. J.*, **28**, 253.

Gaizauskas, V.: 1989, *Solar Phys.*, **121**, 135; Discussion, 471.

Glackin, D. L.: 1975, *Solar Phys.*, **43**, 317.

Gnevyshev, M. N. 1938, *Izv. Gl. Astron. Obs. Pulkove*, **16**, B36.

Hagyard, M. J.; Teuber, D.; West, E. A.; Smith, J. B.: 1984, *Solar Phys.*, **91**, 115.

Hale, G. E.: 1908, *Astrophys. J.*, **28**, 315.

Hale, G. E.; Ellerman, F.; Nicholson, S. B.; Joy, A. H.: 1919, *Astrophys. J.*, **49**, 153.

Hale, G. E.; Nicholson, S. B.: 1925, *Astrophys. J.*, **62**, 270.

Hale, G. E.: 1927, *Nature*, **119**, 708.

Harvey, K. L.; Martin, S. F.: 1973, *Solar Phys.*, **32**, 389.

Ikhsanov, R. N.; Marushin, Yu. V.: 2003, eprint arXiv:astro-ph/0311114

- Ikhsanov, R. N.; Marushin, Yu. V.; Ikhsanov, N. R.: 2004, Multi-Wavelength Investigations of Solar Activity, IAU Symposium, Vol. 223. Edited by Alexander V. Stepanov, Elena E. Benevolenskaya, and Alexander G. Kosovichev. Cambridge, UK: Cambridge University Press, p.257-258.
- Ishii, T. T.; Kurokawa, H.; Takeuchi, T. T.: 1998, *Astrophys. J.*, **499**, 898.
- Kawaguchi, I.; Kitai, R.: 1976, *Solar Phys.*, **46**, 125.
- Kippenhahn, R.: 1994, *Discovering the secrets of the Sun*, Chichester; New York: Wiley.
- Künzel, H.: 1960, *Astronomische Nachrichten*, **285**, 271.
- Kurokawa, H.: 1987, *Solar Phys.*, **113**, 259; Discussion, 264.
- Kurokawa, H.; Wang, T.; Ishii, T. T.: 2002, *Astrophys. J.*, **572**, 598.
- Lehoux, D.: 2001, *History of Modern Science and Mathematics, 1st ed.*, Editor: Baigrie, B.S., Charles Scribner's Sons.
- Leka, K. D.; Canfield, R. C.; McClymont, A. N.; van Driel-Gesztelyi, L.: 1996, *Astrophys. J.*, **462**, 547.
- Lites, B. W.; Low, B. C.; Martinez Pillet, V.; Seagraves, P.; Skumanich, A.; Frank, Z. A.; Shine, R. A.; Tsuneta, S.: 1995, *Astrophys. J.*, **446**, 877.
- López Fuentes, M. C.; Demoulin, P.; Mandrini, C. H.; van Driel-Gesztelyi, L.: 2000, *Astrophys. J.*, **544**, 540.
- López Fuentes, M. C.; Demoulin, P.; Mandrini, C. H.; Pevtsov, A. A.; van Driel-Gesztelyi, L.: 2003, *Astron. Astrophys.*, **397**, 305.
- Luoni, M. L.; Demoulin, P.; Mandrini, C. H.; van Driel-Gesztelyi, L.: 2011, *Solar Phys.*, **270**, 45.
- McKenzie, D. E.; Canfield, R. C.: 2008, *Astron. Astrophys.*, **481**, L65.
- Moreno-Insertis, F.; Vazquez, M.: 1988, *Astron. Astrophys.*, **205**, 289.
- Mullan, D. J.: 2009, *Physics of the Sun: a first course, 1st ed.*, Series: Pure and Applied Physics, Chapman and Hall/CRC.
- Petrovay, K.; van Driel-Gesztelyi, L.: 1997, *Solar Phys.*, **176**, 249.
- Richardson, R. S.: 1941, *Astrophys. J.*, **93**, 24.
- Rust, D. M.; Nakagawa, Y.; Neupert, W. M.: 1975, *Solar Phys.*, **41**, 397.
- Rust, D. M.; Kumar, A.: 1996, *Astrophys. J. Lett.*, **464**, L199.
- Sammis, I.; Tang, F.; Zirin, H.: 2000, *Astrophys. J.*, **540**, 583.
- Sheeley, N. R., Jr.: 1969, *Solar Phys.*, **9**, 347.
- Severny, A. B., 1960, *Izv. Crim. Astrophys. Obs.*, **22**, 12.
- Solanki, S. K.: 2003, *Astron. Astrophys. Rev.*, **11**, 153.
- Stix, M.: 2004, *The sun : an introduction, 2nd ed.*, Astronomy and astrophysics library, Berlin: Springer.
- Tajima, T.; Shibata, K.: 2002, *Plasma astrophysics*, Cambridge, Massachusetts, Perseus Books.

- Tanaka, K.:1975, *BBSO Preprint No.0152*, Big Bear Solar Observatory.
- Tanaka, K.: 1991, *Solar Phys.*, **136**, 133.
- Tandberg-Hanssen, E.; Emslie, A. G.:2009, *The Physics of Solar Flares*, Cambridge, UK: Cambridge University Press.
- Tang, F.: 1983, *Solar Phys.*, **89**, 43.
- Török, T.; Berger, M. A.; Kliem, B.: 2010, *Astron. Astrophys.*, **516**, A49.
- van Driel-Gesztelyi, L.; Petrovay, K.: 1990, *Solar Phys.*, **126**, 285.
- Waldmeier, M.:1938, *Zeitschrift für Astrophysik*, **14**, 91. Waldmeier, M.: 1955, Leipzig, Geest and Portig, erweiterte Aufl.
- Wang, H.: 1992, *Solar Phys.*, **140**, 85.
- Zirin, H.: 1972, *Solar Phys.*, **22**, 34.
- Zirin, H.; Liggett, M. A.: 1987, *Solar Phys.*, **113**, 267; Discussion, 282.
- Zirin, H.: 1988, *Astrophysics of the Sun, Cambridge and New York*, Cambridge University Press.
- Zirker, J. B.: 2001, *Journey from the Center of the Sun*, Princeton: Princeton University Press.
- Zwaan, C.: 1985, *Solar Phys.*, **100**, 397.

## Chapter 2

- Sammis, I.; Tang, F.; Zirin, H.: 2000, *Astrophys. J.*, **540**, 583.
- Hansen, P. C., Pereyra, V., Scherer, G.: 2012, *Least Squares Data Fitting With Applications*, Johns Hopkins Univ. Press, Baltimore, MD, 163-175.
- Magara, T.: 2014, *Pub. Astron. Soc. Japan. Lett.*, **66**, L6.

## Chapter 3

- Abramenko, V. I. : 2005, *Astrophys. J.*, **629**, 1141.
- Antalová, A.: 1991, *Bull. Astron. Inst. Czechosl.*, **42**, 316.
- Antalová, A.: 1996, *Contrib. Astron. Obs. Skalnaté Pleso*, **26**, 98.
- Brown, D. S., Nightingale, R. W., Alexander, D., Schrijver, C. J., Metcalf, T. R., Shine, R. A., Title, A. M., Wolfson, C. J.: 2003, *Solar Phys.*, **216**, 79.
- Călugăreanu, G.: 1959, *Rev. Roum. Math. Pure Appl.* **4**, 5.
- Chae, J.: 2001, *Astrophys. J.*, **560**, 95.
- Chae, J., Wang, H., Qiu, J., Goode, P. R., Strous, L., Yun, H. S.: 2001, *Astrophys. J.*, **560**, 476.
- Delaboudinière, J. -P., Artzner, G. E., Brunaud, J., Gabriel, A. H., Hochedez, J. F., Millier, F., *et al.*: 1995, *Solar Phys.*, **162**, 291.

- Domingo, V., Fleck, B., Poland, A. I.: 1995, *Solar Phys.*, **162**, 1.
- Fan, Y., Fisher, G. H., Deluca, E. E.: 1993, *Astrophys. J.*, **405**, 390.
- Fan, Y., Zweibel, E. G., Linton, M. G., Fisher, G. H.: 1999, *Astrophys. J.*, **521**, 460.
- Gnevyshev, M. N. 1938, *Izv. Gl. Astron. Obs. Pulkove*, **16**, B36.
- Guo, Y., Ding, M. D., Cheng, X., Zhao, J. Pariat, E.: 2013, *Astrophys. J.*, **779**, 157.
- Handy, B. N., Acton, L. W., Kankelborg, C. C., Wolfson, C. J., Akin, D. J., Bruner, M. E., *et al.*: 1999, *Solar Phys.*, **187**, 229.
- Hansen, P. C., Pereyra, V., Scherer, G.: 2012, *Least Squares Data Fitting With Applications*, Johns Hopkins Univ. Press, Baltimore, MD, 163-175.
- Ikhsanov, R. N., Marushin, Y. V.: 2003, *arXiv:astro-ph*, 0311114.
- Ikhsanov, R. N., Marushin, Yu. V., Ikhsanov, N. R.: 2004, In: Stepanov, A.V., Benevolenskaya, E. E., Kosovichev, A. G. (eds.), *Multi-Wavelength Investigations of Solar Activity*, *IAU Symp.*, **223**, 257.
- Ishii, T. T., Kurokawa, H., Takeuchi, T. T.: 1998, *Astrophys. J.*, **499**, 898.
- Jin, C. L.; Qu, Z. Q., Xu, C. L., Zhang, X. Y., Sun, M. G.: 2006, *Astrophys. Space Sci.*, **306**, 23.
- Jing, J., Song, H., Abramenko, V. I., Tan, C., Wang, H.: 2006, *Astrophys. J.*, **644**, 1273.
- Joshi, B., Joshi, A.: 2004, *Solar Phys.*, **219**, 343.
- Künzel, H.: 1960, *Astron. Nachr.*, **285**, 271.
- Kurokawa, H.: 1987, *Solar Phys.*, **113**, 259.
- Kurokawa, H. Wang, T., Ishii, T. T.: 2002, *Astrophys. J.*, **572**, 598.
- Leka, K. D., Canfield, R. C., McClymont, A. N., van Driel-Gesztelyi, L.: 1996, *Astrophys. J.*, **462**, 547.
- Linton, M. G., Fisher, G. H., Dahlburg, R. B., Fan, Y.: 1999, *Astrophys. J.*, **522**, 1190.
- Livingston, W.: 2002, *Solar Phys.*, **207**, 41.
- López Fuentes, M. C., Demoulin, P., Mandrini, C. H., van Driel-Gesztelyi, L.: 2000, *Astrophys. J.*, **544**, 540.
- López Fuentes, M. C., Mandrini, C. H.: 2008, *Bol. Asoc. Argent. Astron.*, **51**, 31.
- Luoni, M. L., Démoulin, P., Mandrini, C. H., van Driel-Gesztelyi, L.: 2011, *Solar Phys.*, **270**, 45.
- Magara, T, Longcope, D. W.: 2003, *Astrophys. J.*, **586**, 630.
- Magara, T.: 2011, *Pub. Astron. Soc. Japan.*, **63**, 417.
- Magara, T.: 2014, *Pub. Astron. Soc. Japan. Lett.*, **66**, L6.
- Moffatt, H. K., Ricca, R. L.: 1992, *Proc. Roy. Soc. London A*, **439**, 411.
- Nishizuka, N., Asai, A., Takasaki, H., Kurokawa, H., Shibata, K.: 2009, *Astrophys. J. Lett.*, **694**, L74.
- November, L. J., Simon, G. W.: 1988, *Astrophys. J.*, **333**, 427.

- Park, J., Moon, Y.-J., Gopalswamy, N.: 2012, *Astrophys. J.*, **750**, 48.
- Petrovay, K., Moreno-Insertis, F.: 1997, *Astrophys. J.*, **485**, 398.
- Petrovay, K., van Driel-Gesztelyi, L.: 1997, *Solar Phys.*, **176**, 249.
- Pevtsov, A. A., Longcope, D. W.: 1998, *Astrophys. J.*, **508**, 908.
- Poisson, M., López Fuentes, M., Mandrini, C. H., Demoulin, P., Pariat, E.: 2013, *Adv. Space Res.* **51**, 1834.
- Priest, E.: 2014, *Magnetohydrodynamics of the Sun*, Cambridge, UK: Cambridge University Press.
- Ricca, R. L.: 1995, *J. Phys. A*, **28**, 2335.
- Rust, D. M., Kumar, A.: 1996, *Astrophys. J. Lett.*, **464**, 199.
- Sammis, I., Tang, F., Zirin, H.: 2000, *Astrophys. J.*, **540**, 583.
- Scherrer, P. H., Bogart, R. S., Bush, R. I., Hoeksema, J. T., Kosovichev, A. G., Schou, J., *et al.*: 1995, *Solar Phys.*, **162**, 129.
- Shi, Z. X., Wang, J. X.: 1994, *Solar Phys.*, **149**, 105.
- Shimizu, T.: 1995, *Pub. Astron. Soc. Japan.*, **47**, 251.
- Shimojo, M., Shibata, K.:1999, *Astrophys. J.*, **516**, 934.
- Solanki, S. K.: 2002, *Astron. Nachr.*, **323**, 165.
- Tanaka, K.:1975, *BBSO Preprint No.0152*, Big Bear Solar Observatory.
- Tanaka, K.: 1991, *Solar Phys.*, **136**, 133.
- Tian, L., Alexander, D., Liu, Y., Yang, J., 2005, *Solar Phys.*, **229**, 63.
- Török, T., Berger, M. A., Kliem, B.: 2010, *Astron. Astrophys.*, **516**, 49.
- van Driel-Gesztelyi, L., Petrovay, K.: 1990, *Solar Phys.*, **126**, 285.
- van Driel-Gesztelyi, L., Csepura, G., Schmieder, B., Malherbe, J. -M., Metcalf, T.: 1997, *Solar Phys.*, **172**, 151.
- van Driel-Gesztelyi, L., Malherbe, J. -M., Démoulin, P.: 2000, *Astron. Astrophys.*, **364**, 845.
- Waldmeier, M.: 1955, *Ergebnisse und Probleme der Sonnenforschung*, Geest & Portig, Leipzig, 164-165.
- Yan, Xiao-Li., Qu, Zhong-Quan., Xu, Cheng-Lin., Xue, Zhi-Ke., Kong, De-Fang.: 2009, *Res. Astron. Astrophys.* **9**, 596.
- Zirin, H., Liggett, M. A.: 1987, *Solar Phys.*, **113**, 267.
- Zwaan, C.: 1978, *Solar Phys.*, **60**, 213.

## Chapter 4

- Brandt, P. N., Schmidt, W., Steinegger, M.: 1990, *Solar Phys.*, **129**,191.
- Chae, J., Moon, Y. -J., Pevtsov, A. A.: 2004, *Astrophys. J.*, **602**, 65.
- Chapman, G. A., Cookson, A. M., Dobias, J. J.: 1994, *Astrophys. J.*, **432**, 403.
- Gonzalez, R., Woods, R, :1992, *Digital Image Processing*, Addison-Wesley, Boston,

---

Chap. 2.

- Harvey, K. L., Jones, H. P., Schrijver, C. J., Penn, M. J.: 1999, *Solar Phys.*, **190**, 35.
- Howard, R., LaBonte, B. J.: 1981, *Solar Phys.*, **74**, 131.
- Iida, Y., Yokoyama, T., Ichimoto, K.: 2010, *Astrophys. J.*, **713**, 325.
- Kálmán, B.: 2001, *Astron. Astrophys.* **371**, 731.
- Kubo, M., Low, B. C., Lites, B. W.: 2010, *Astrophys. J.*, **712**, 1321.
- November, L. J., Simon, G. W.: 1988, *Astrophys. J.*, **333**, 427.
- Pariat, E., Aulanier, G., Schmieder, B., Georgoulis, M. K., Rust, D. M., Bernasconi, P. N.: 2004, *Astrophys. J.*, **614**, 1099.
- Parker, E. N.: 1955, *Astrophys. J.*, **121**, 491.
- Parker, E. N.: 1984, *Astrophys. J.*, **280**, 423.
- Priest, E. R.: 1982, *Solar Magneto-hydrodynamics*, D. Reidel, Dordrecht, 291.
- Rabin, D., Moore, R., Hagyard, M. J.: 1984, *Astrophys. J.*, **287**, 404.
- Sammis, I., Tang, F., Zirin, H.: 2000, *Astrophys. J.*, **540**, 583.
- Scherrer, P. H., *et al.*: 1995, *Solar Phys.*, **162**, 129.
- Wallenhorst, S. G., Howard, R.: 1982, *Solar Phys.*, **76**, 203.
- Wallenhorst, S. G., Topka, K. P.: 1982, *Solar Phys.*, **81**, 33.
- Zirin, H.: 1985, *Astrophys. J.*, **291**, 858.
- Zirin, H., Liggett, M. A.: 1987, *Solar Phys.*, **113**, 267.

## Chapter 5

- Sammis, I.; Tang, F.; Zirin, H.: 2000, *Astrophys. J.*, **540**, 583.
- Priest, E.: 2014, *Magnetohydrodynamics of the Sun*, Cambridge, UK: Cambridge University Press.